Mon. Not. R. Astron. Soc. **000**, 1–18 (2013) Printed 24 July 2013 (MN LATEX style file v2.2)

Exploring Metallicity Gradients of Nearby Spirals at High Spatial Sampling with VENGA IFU Spectroscopy

K. F. Kaplan[1], S. Jogee[1], L. Kewley[2], and VENGA Team
[1] *Department of Astronomy, University of Texas at Austin, 2515 Speedway, Stop C1400, Austin, TX 78712-1205, USA*
[2] *Research School of Astronomy and Astrophysics, The Australian National University, Cotter Road, Weston Creek, ACT 2611*

Accepted 2013 Month XX. Received 2013 Month XX

ABSTRACT

We present an IFU-based study of the gas-phase metallicity Z_{gas}, SFRs, DIG, and ionization parameter q in nine nearby spiral galaxies drawn from the VIRUS-P Exploration of Nearby Galaxies (VENGA) survey. Our sample has IFU data (with coverage 3600-6800 Å and spectral resolution ~ 5 Å FWHM at 5000 Å) over a large fraction of the galaxy's disk, while maintaining a high spatial sampling and resolution (median $\mathrm{PSF_{FWHM}} \sim 298$ pc). We exclude fibers where gas is not primarily ionized by photons from massive stars and present maps of q, extinction-corrected Hα-based SFRs and Z_{gas} from seven commonly used Z_{gas} diagnostics: R_{23}-KK04, R_{23}-M91, R_{23}-Z94, N2O2-KD02, O3N2-PP04, N2-D02, and N2-PP04. We resolve individual galactic components (bulge, bar, spiral arms, outer disk) and explore how Z_{gas} varies across them. Our results are: **(1)** Between these different Z_{gas} diagnostics, the shape of the Z_{gas} radial profiles show fairly good agreement beyond the inner 1-2 kpc, and yield flat to sometimes slightly negative gradients. There is good agreement in absolute value of Z_{gas}, within 0.1 to 0.2 dex, between R_{23}-KK04, R_{23}-M91, R_{23}-Z94, and N2O2-KD02. **(2)** The Z_{gas} gradients in both our isolated barred and unbarred spirals all show flat to slightly negative gradients. This contradicts previous claims that isolated unbarred galaxies have steeper gradients than those that are barred, and suggests all disk galaxies have their gradients flattened by existing or previous bars, interactions, and feedback. **(3)** Previous studies claim interacting galaxies exhibit flatter gradients than those that are isolated. The one interacting galaxy in our sample (NGC 5194) exhibits a flat gradient, consistent with the idea that gas flows and bars induced by tidal interactions flatten Z_{gas} gradients. Although, we note that the gradients for our isolated galaxies are also similarly flat. **(4)** The Z_{gas} gradients in our subsample of spiral galaxies are markedly shallower than in higher redshift galaxies at $z \sim 1.5-2.0$. This is consistent with the idea that Z_{gas} gradients are flattening over cosmic time. We find that cosmologically motivated SPH models of Z_{gas} evolution that include radial gas flows, baryonic physics, and typical feedback best reproduce this observed evolution. The overall picture that emerges from data and models is that an inside-out disk formation scenario, coupled with efficient radial mixing resulting from gas inflows and outflows induced by bars (both past and present), galaxy interactions, and feedback account for the evolution of Z_{gas} gradients in galaxies.

1 INTRODUCTION

Spatially resolved integral field unit (IFU) spectroscopy allows detailed mapping and study of the gas phase metallicity ($Z_{gas} \equiv \log(\mathrm{O/H})+12$) to high spatial sampling and spectral resolution across nearby spiral galaxies. Z_{gas} provides critical information about the assembly history and evolution in a galaxy. The value of Z_{gas} at a given location in a galaxy depends on the star formation rate (SFR) which enriches the gas, and the relative inflow and outflow rate of gas from within the galaxy and from external sources. These processes are ultimately tied to the evolution of the galaxy from mergers (e.g., Somerville &

Primack 1999; Cole et al. 2000; Conselice 2009; Jogee et al. 2009; Lotz et al. 2011), cold mode accretion (e.g., Kereš et al. 2005, 2009; Dekel & Birnboim 2006; Dekel et al. 2009a,b), and secular processes, such as bar-driven gas inflow and outflow (e.g., Kormendy & Kennicutt 2004; Jogee et al. 2005). Feedback processes also play an important role as enriched gas can be ejected in outflows driven by stellar (e.g., supernovae) and AGN feedback.

This paper focuses on studying the distribution of Z_{gas} across the different components of a spiral galaxy such as the central (disky or classical) bulge, bar, spiral arms, outer disk, etc. in the context of understanding what Z_{gas} is telling us about the galaxy's history and chemical evolution. To test different modes of galaxy evolution, we target different types of spiral galaxies including those that are isolated, interacting, barred, unbarred, and have different morphologies which probe different avenues of galaxy evolution. The first studies for Z_{gas} were surveys of large numbers of galaxies using multi-slit spectroscopy targeting bright HII regions. Studies by Zaritsky et al. (1994), Martin & Roy (1994), and Vila-Costas & Edmunds (1992) have targeted galaxies of different morphologies, specifically isolated unbarred vs. barred spirals and claim that barred spirals exhibit flatter Z_{gas} gradients than unbarred spirals due to radial gas mixing induced between different dynamical resonances of a barred potential. Observations by Rupke et al. (2010b) and simulations by Hernquist & Mihos (1995); Mihos & Hernquist (1996) studied spirals that are interacting, and claim they exhibit flatter Z_{gas} gradients than isolated galaxies due to gas flows driven by gravitational torques and bars induced by the interactions.

Older studies that focused on Z_{gas} used multi-slit spectroscopy, but this technique suffers from poor spatial sampling. One of the most effective avenues for progress for studying Z_{gas} is through spatially-resolved, high-quality, integral field spectroscopic data of nearby galaxies. Previous IFU studies of nearby spirals have been used to study Z_{gas}. The PINGS survey (Rosales-Ortega et al. 2010) specifically targets HII regions in nearby face on spirals. CALIFA (Sánchez et al. 2011) is a survey that targets spirals that are slightly further away, using the same instruments as PINGS. A sample of nearby face on spiral galaxies by Sánchez et al. (2012) using both PINGS and CALIFA data shows the Z_{gas} gradients in their sample are independent of galaxy type and morphology.

In this paper, we take advantage of the VIRUS-P Exploration of Nearby Galaxies (VENGA) survey (Blanc et al. 2013, 2010). VENGA is a powerful integral field spectroscopic survey of a large sample of 30 nearby representative spirals. VENGA delivers exquisite, high-quality, spatially-resolved data (typically on scales of a few hundred pc) having moderate resolution (~ 5 Å FWHM at 5000 Å), and with broad blue-to-red wavelength coverage (3600-6800 Å).

This study focuses on a subset of nine spiral galaxies from VENGA. To address what kinds of processes in galaxy evolution affect Z_{gas}, we selected galaxies where we have high spatial coverage, sampling, and resolution and select galaxies of different types including barred, unbarred, isolated, and interacting galaxies. We selected galaxies which have the highest spatial resolution (median $\mathrm{PSF_{FWHM}} = 298$ pc, a median ratio of (R_e-bulge/$\mathrm{PSF_{FWHM}}$) = 3.63), and IFU data covering a large fraction of the galaxy's disk so that we can resolve individual galactic components such as the bulge (classical or pseudo), bar, and outer disk, and thereby explore how Z_{gas} varies across these different components (§ 2.2). Our sample contains nine isolated galaxies, of which six are barred and three are unbarred, as well as one unbarred interacting galaxy. The galaxies span a range of Hubble types, from Sab to Sd, and have good coverage with ancillary data.

Our large λ coverage (3600-6800 Å) and fine spatial sampling allow us to tackle numerous issues that have plagued previous Z_{gas} studies: **(i)** Many Z_{gas} diagnostics work well when observing emission line ratios from gas that is ionized by by photons from massive stars in regions of high SF, but break down when observing gas that is ionized by a hard radiation field from an AGN or is shocked (e.g., in starburst outflows). Studies without spatially resolved IFU data cannot exclude contaminated regions, leading to erroneous trends in Z_{gas}, as emphasized by numerous authors (Yuan et al. 2012; Rich et al. 2010; Kewley & Ellison 2008; Kewley & Dopita 2002; Baldwin et al. 1981). We avoid this pitfall by using our large λ coverage to produce diagnostic diagrams (often called BPT diagrams after Baldwin et al. 1981) based on different line ratios ([NII]/Hα, [SII]/Hα against [OIII]/Hβ), and use these to remove Seyfert and LINER regions (§4.1). **(ii)** The inferred Z_{gas} from some indicators (e.g., R_{23} & N2) exhibit degeneracies between the calibration of that indicator and Z_{gas}. In this work, we break these degeneracies by using our large λ coverage to estimate Z_{gas} via seven different diagnostics based on several indicators (e.g., R23, N2O2, O2N2, N2) and different calibrations (§4.5). **(iii)** Some indicators (e.g. R_{23}) depend on the ionization parameter q, and not all calibrations take this into account. This may be part of the reason for the difference in absolute values of Z_{gas} or/and radial gradients in Z_{gas} given by different Z_{gas} calibrations or diagnostics. In this work, we calculate *spatially resolved* maps of q across the bulge, bar, and outer disk and across different regions of different SF intensity (§4.4). We use q to explore potential differences between the seven Z_{gas} diagnostics.

This paper is organized as follows: §2.1 introduces the VENGA survey; §2.2 describes our subsample of nine nearby spirals; and §3 covers the data reduction. For our methodology, §4.1 discusses the use of BPT diagrams to remove Seyfert and LINER contaminated regions; §4.2 discusses how we identify and remove regions dominated by emission from diffuse ionized gas; §4.3 details how we compute SFRs; §4.4 shows our computation of the ionization parameter q; and §4.5 shows how we compute the different Z_{gas} diagnostics. For our results, §5.1 compares Z_{gas} between the different diagnostics; §5.2 presents the spatially-resolved maps of Z_{gas}, q, & SFR, as well as the Z_{gas} gradients, in these galaxies; §5.3 compares our Z_{gas} results to those of other isolated barred and unbarred galaxies and to our expectations based upon our theoretical understanding of how gas behaves in a barred gravitational potential; §5.4 compares our Z_{gas} results to interacting galaxies; §5.5 compares the Z_{gas} in low vs. high redshift in observed galaxies, and § 5.6 compares to the evolution in theoretical models.

2 OBSERVATIONS AND SAMPLE

2.1 VENGA

VENGA is an unprecedented integral field spectroscopic survey of the inner and outer regions of a large sample of 30 representative nearby spiral galaxies with the VIRUS-P IFU on the 2.7 meter telescope at McDonald Observatory (for details see Blanc et al. 2013). VIRUS-P has large (4.3″) sensitive fibers and the largest FOV (110″ × 110″ or 3.36 arcmin^2) among existing IFUs (Hill et al. 2008). Table 1 shows a comparison between VENGA and other IFU surveys. Over the past four years, this survey has been allocated $\sim$ 150 nights of observing time. Three dithers are performed on each galaxy to compensate for the 1/3 filling factor of VIRUS-P, and multiple pointing are used to get spectra out to large radii (typically 0.7 R_{25}) in the disks of the spiral galaxies (Fig. 1). At the typical distance of the galaxies, the large fibers provide high signal-to-noise spectra, while sampling galaxies at high median spatial resolution of 298 pc. Furthermore, each galaxy is observed a blue (3600-5800 Å) and a red (4600-6800 Å) setup to get a wide wavelength coverage. The spectral resolution is $R \approx 1000$ or $\sim$ 5 Å FWHM at 5000 Åor , which corresponds to $\sim$ 120 km s^{-1}. The VENGA sample consists of 30 nearby spirals, 80% of which are at a distance below 20 Mpc. All the target galaxies are listed in Table 3 and Figure 1. The 30 nearby target spirals were selected for a broad range of different science goals by various co-investigators on the project. The sample covers a range of Hubble types (Sa to Sd) and includes galaxies with classical bulges and pseudo-bulges (e.g., Weinzirl et al. 2009; Kormendy & Kennicutt 2004; Fisher & Drory 2008), as well as barred and unbarred objects. The VENGA galaxies have a global SFR typically in the range of 0.5 to 10 M$_\odot$ yr^{-1}, and stellar masses primarily in the range of a few times 10^9 to 10^{11} M$_\odot$. For stellar mass above 10^{10} M$_\odot$, they span a representative range of the stellar mass-SFR plane, as shown in Figure 1. Most galaxies have ancillary data from a variety of sources including HST, Spitzer, GALEX, CO maps from BIMA SONG (Helfer et al. 2003) and the CARMA CO survey STING (Rahman et al. 2011), and archival HI 21 cm maps from THINGS (Walter et al. 2008) and ALFALFA (Giovanelli et al. 2005).

2.2 Subsample Selection

We picked a subset of nine spiral galaxies from the 30 VENGA spirals for our study of Z_{gas}, based on criteria (i) to (vi) below. In particular, we need high spatial resolution (criteria ii and iv; Table 2), in order to resolve individual components, such as the bulge (classical and pseudo), bar, outer disk, and to explore how Z_{gas} varies across these components, and across dynamically different regions of the galaxy. At the same time, we want IFU data to cover a large fraction of the galaxy's R_{25} radius (criterion iii), so that we can explore how Z_{gas} varies from the inner few kpc out to fairly large radii in the disk.The availability of ancillary data (criterion v) and the use of our Z_{gas} by other studies (criterion vi) were secondary factors guiding our choices. Criteria (i) to (vi) for our subsample selection are listed below.

(i) **Inclination** - Our view of highly inclined galaxies is subject to extinction by dust and the high inclination makes it difficult to spatially resolve the separate galactic components. Face-on galaxies lack information on the kinematics of the stars and gas, which is important for detecting azimuthal and radial motions. To balance out these two extremes, our sample covers a range of low to moderate inclinations, between $27 \rightarrow 66°$, with a median of 35°.

(ii) R_e**-bulge/PSF$_{\mathbf{FWHM}}$** - One way to quantify how well VIRUS-P can spatially resolve a galaxy is to divide the half light radius of the bulge (R_e-bulge) by the FWHM of the PSF of VIRUS-P (4.3"). We place a lower limit on the ratio (R_e-bulge/PSF$_{\rm FWHM}$) $>\sim 2$ for galaxies with significant bulges (B/T > 0.01). Our subsample has a median (R_e-bulge/PSF$_{\rm FWHM}$) of 3.63.

(iii) **Fraction of R25**- We select galaxies where the fraction of the disk's R25 radius (f_{R25}) covered by VIRUS-P observations is at least 30% ($f_{R25} > 0.3$). Our sample has f_{R25} ranging from $0.38 \rightarrow 1.18$ with a median of 0.66.

(iv) **Spatial Resolution & Distance** - To ensure we can spatially resolve regions of a galaxy that are dynamically different, such as the inner kiloparsec region (where the rotation curve is rising steeply and where outer inner Lindblad resonance (OILR) and inner inner Lindblad resonances (IILR) of stellar bars lie), the bulge (classical or pseudo), primary stellar bar, spiral arms, and different HII regions across the disk, we target galaxies where our PSF$_{\rm FWHM}$ < 600 pc. This constraint sets the maximum distance of our subsample to be $\sim$ 30 Mpc. Note that a large spatial coverage (criterion iv) tends to select distant galaxies, while criteria (ii) ((R_e-bulge/PSF$_{\rm FWHM}$) $>\sim 2$) and the present criterion of PSF$_{\rm FWHM}$ < 600 pc tends to select galaxies that are nearby. Applying these competing selection criteria results in our subsample picking galaxies at an intermediate median distance of 14.3 Mpc, giving us a median spatial resolution of 298 pc.

(v) **Ancillary Data** - We preferentially select galaxies that cover a large amount of ancillary data such as Spitzer, 2MASS, CO, HI, GALEX, etc.

(vi) **Use of data by other studies** - The [CII] studies by the KINGFISH team (A. Bolatto and D. Fisher, private communication; Kennicutt et al. 2011) and studies of the CO-to-H_2 conversion factor by Sandstrom et al. (2012) require Z_{gas} maps of high-quality and high spatial resolution. To the extent possible, we have included galaxies from these studies in our subsample

Table 3 shows our subsample of nine spiral galaxies that result from the above criteria highlighted in bold with respect to to the whole VENGA sample. Table 2 shows our subsample in more detail. In summary, it includes galaxies which have high spatial resolution (with a median $\mathrm{PSF_{FWHM}}$ of 298 pc and a median (R_e-bulge/$\mathrm{PSF_{FWHM}}$) of 3.63) and IFU data coverage over a large fraction of the galaxy's disk (median f_{R25} of 0.66). This allows us to resolve individual galaxy components such as the bulge (classical and pseudo), bar, and outer disk, and thereby explore how Z_{gas} varies across these components. The sample contains nine isolated galaxies, of which six are barred and three are unbarred, as well as one unbarred interacting galaxy. The galaxies span a range of Hubble types from Sab to Sd and have good coverage with ancillary data. In terms of overlap with other studies, six galaxies are in the KINGFISH survey by Kennicutt et al. (2011), and five galaxies in the CO-to-H_2 conversion factor study by Sandstrom et al. (2012).

3 DATA REDUCTION

Figure 2 illustrates our data reduction and analysis steps (Adams et al. 2011; Blanc et al. 2013). A data reduction pipeline (VACCINE; Adams et al. 2011) has been developed to do the basic data reduction, including the bias and dark subtraction, flat fielding, wavelength calibration, cosmic ray rejection and sky subtraction. After running VACCINE, an additional sky subtraction step was done for a better removal of sky residuals by calculating spline interpolation of a median of sky frame for the night. Flux calibration is done in two steps. The first step uses spectrophotometric standard star frames for wavelength-dependent flux calibration for each observing run. The second step uses SDSS broad-band images to perform absolute flux calibration and astrometry correction to compensate for changing weather conditions and uncertainty in the pointings. The uncertainty for the flux in each fiber is a combination of the readout noise, Poisson uncertainty, and systematic error. Calculation of the uncertainty is detailed in Blanc et al. (2013). Finally, all the science frames are rebinned and collapsed together to generate a datacube.

We extract the emission lines from the underlying stellar continuum by using PARADA, a modified version of GANDALF (Sarzi et al. 2006). We use the MILES (Sánchez-Blázquez et al. 2006) empirical stellar library, which has over 900 stars with a wide range of spectral types and metallicities, and is well flux-calibrated. Each stellar spectrum is convolved to the wavelength-dependent VIRUS-P spectral resolution (median of $\sim$ 5 ÅFWHM at 5000 Å). The observed spectra are fit with the templates in pixel space using the Penalized Pixel-Fitting (pPXF; Cappellari & Emsellem 2004) method, from which the stellar kinematics are extracted.

Spectra can be binned spatially, if desired, to a constant signal-to-noise ratio, and Galactic extinction is corrected using the extinction map of Schlegel et al. (1998). Spectra are decomposed by Gaussian-shape emission lines being simultaneously fitted with the underlying stellar continuum. A multiplicative high order Legendre polynomial is used to account for the internal reddening. The uncertainty in the flux for each of the emission line fits is given by GANDALF. We check the quality of our data using a technique outlined by Oh et al. (2011), comparing the residuals of our fits of the stellar continuum and emission lines to the statistical noise in the data.

The resulting data cubes store spatially resolved 2D information on the gas emission line fluxes, stellar continuum spectra, stellar and gas velocities, and velocity dispersions from which we will derive Z_{gas}, SFRs, and the ionization parameter q. All emission line fluxes are corrected for extinction by dust intrinsic to the observed galaxies using Hα/Hβ line ratio decrement described in Osterbrock & Ferland (2006). Examples of the data products, such as the stellar velocity field, extinction corrected Hα map, and Hα velocity field are shown for each galaxy in Figure 3. For the isolvelocity contours, we use Voronoi binning for regions with low S/N, with a minimum of S/N $\geqslant$ 3 for Hα and a minimum S/N $\geqslant$ 50 for the stellar continuum.

4 METHODOLOGY

4.1 BPT Diagnostics to Identify Regions as Star Forming, Seyfert, or LINER

Gas metallicity (Z_{gas}) diagnostics are all based on the assumption that the emission line fluxes we measure are from gas being photoionized by UV light from hot young stars. Therefore, it is important to ensure that our Z_{gas} measurements only target fibers where the gas is predominantly ionized by photons from massive stars. Other sources of energy, such as AGN or shocks in the gas, can affect the strength of the emission lines and give us erroneous results. Previous Z_{gas} studies, especially single fiber or slit spectroscopy of individual galaxies, such as SDSS, are unable to mask out regions not photoionized by young massive stars and this contaminates their Z_{gas} results (Yuan et al. 2012; Rich et al. 2010; Kewley & Ellison 2008; Kewley & Dopita 2002; Baldwin et al. 1981). The high quality IFU data and large number of lines observed by VENGA allow us to assess each fiber, probing sub-kpc scales, and separate regions primarily photoionized by young massive stars from those excited by shocks or AGN activity, through the use of the "Baldwin, Phillips & Terlevich" (BPT) diagnostics: [OIII]λ5007/Hβ vs. [NII]λ6584/Hα, [OIII]λ5007/Hβ vs. [SII]$\lambda\lambda$6717,6731/Hα, and [OIII]λ5007/Hβ vs. OI]λ6300/Hα (Baldwin et al. 1981; Kewley et al. 2006b; Rich et al. 2010; Kewley et al. 2001). We apply a signal-to-noise cut of $S/N > 5$ for the lines used in our BPT diagrams. We are unable to make use of the [OIII]/Hβ vs. [OI]/Hα BPT diagnostic due to masking out the nearby telluric lines. Examples of the [OIII]/Hβ vs. [NII]/Hα and [OIII]/Hβ vs. [SII]/Hα BPT diagrams can be seen for NGC 2903 in Figure 4.

BPT diagnostics work as follows: The [OIII]/Hβ ratio (y-axis in Figure 4) is sensitive to both Z_{gas}, and the hardness of the radiation field. Low Z_{gas} and hard radiation fields tend to give high [OIII]/Hβ while high Z_{gas} and soft radiation field give low [OIII]/Hβ. To break this degeneracy, BPT diagrams introduce another emission line ratio such as [NII]/Hα or [SII]/Hα (x-axis in Figure 4). Both [NII]/Hα and [SII]/Hα decrease with harder radiation fields, while they generally increase with Z_{gas}, although at high values they saturate and then start to decrease, as seen for [NII]/Hα in Figure 7. The physics behind BPT diagrams are described in detail by Kewley & Dopita (2002) and Davies et al. (2013, in prep.). By making use of multiple line ratios, BPT diagrams can separate regions dominated by recent SF from regions dominated by an AGN hard radiation field or shocks. Points dominated by recent SF tend to fall in the lower left of the BPT diagrams while points of AGN or shock excitation tend to fall in the upper right. We use the thresholds set by Kewley et al. (2001) to separate star forming from excited regions, and then exclude fibers above this threshold from our analysis for Z_{gas}, SFRs, and q.

We identify Seyfert and LINERs on the [SII]/Hα BPT diagram using the method of Kewley et al. (2006b) (seen as the blue line in Figure 4). Since [OIII]/Hβ is mostly sensitive to the hardness of the background radiation field, regions contaminated by a Seyfert like radiation field tend to fall in the Seyfert region higher on the BPT diagram. Excited regions with a softer radiation field tend to have lower [OIII]/Hβ and fall in the LINER region lower on the BPT diagram. Shocked gas tends to have enhanced [NII]/Hα and [SII]/Hα ratios do not greatly raise [OIII]/Hβ since there is no hard radiation field, so shocked regions are typically found in the LINER region of the BPT diagrams. This can be seen in Farage et al. (2010) who finds that shocked gas filaments in NGC 4696 from a minor merger mostly fall in the LINER region of their BPT diagrams. Their models (MAPPINGS III, Sutherland & Dopita 1993) show that higher shock velocities lead to higher [NII]/Hα and [SII]/Hα values but [OIII]/Hβ tends to saturate at log([OIII]/Hβ)$\sim$ 0. Allen et al. (2008) presents a large library of radiative shock models from the MAPPINGS III code. The library includes models that with only shocks, and those that add a hard radiation field that would be the *precursor* for the shocks. The models show typically that for shocks only, [NII]/Hα and [SII]/Hα increase with increasing shock velocity, while the [OIII]/Hβ ratio remains invariant, putting the shock only models in the LINER region of the BPT diagrams. For the models that include precursor hard radiation field, the [OIII]/Hβ ratio increases, pushing their results into the Seyfert region of the BPT diagrams.

We apply a new technique to map out the *excitation sequence* using the [SII] BPT diagrams, first employed to study the mixing sequence of NGC 7130 by Davies et al. (2013, in prep.). The middle curve is the threshold below which fibers are dominated by photoionization from massive young stars, given by Kewley et al. (2001). The *excitation sequence* quantifies the distance a fiber is from this threshold. The region on the BPT diagram is divided into six slices defined by five curves. The two curves above it are versions of the middle curve scaled by 0.4 and 0.8 dex along the log([OIII]/Hβ) axis. The two curves below are similarly scaled downward by 0.4 and 0.8 dex along the log([OIII]/Hβ) axis. This essentially divides the BPT diagram into six *slices* to quantify the degree of excitation. We then color code the fibers based on where they fall in these slices, as seen on the left side of Figure 5. One major advantage of using IFU data to study excitation in BPT diagrams is that we can take the color coded *excitation sequence* and map it back to the image of the galaxy, as seen in Figures 4 & 5, to study the excitation across the different galactic components.

4.2 Contribution from Diffuse Ionized Gas

Diffuse ionized gas (DIG) consists of warm ($\sim 10^4$ K) ionized gas from that resides up to two kiloparsecs above and below the plane of a spiral galaxy's disk, and consists of gas that has been raised above the galactic disk by supernovae at large scale heights and superbubbles created from regions in the disk where multiple supernovae have occurred (Wood et al. 2010). The DIG consists of the majority of ionized gas in a galaxy (Walterbos 1998), and its low level emission is a possible source of contamination superimposed over emission from HII regions ionized by photons from massive stars in the disk (see reviews by Mathis 2000; Haffner et al. 2009). The majority of the energy ionizing the DIG is currently thought to come from massive OB stars in the galactic disk from which ionizing Lyman continuum photons can travel large path lengths up to several kiloparsecs above the galactic disk before ionizing the DIG (Walterbos 1998), so the source of ionizing photons is non-local. While the DIG is thought to be produced by supernovae, the recombination time scale is on the order of $\sim$ 3 Myr while the dynamical time scale is $\sim$ 100 Myr, so the DIG must be subject to constant photoionization by hot OB-stars (Wood et al. 2010; Spitzer 1978). Shock ionization might also be a secondary contribution (Martin 2000). Since the DIG is not primarily ionized by photons from local SF, it is a poor tracer of local Z_{gas}, so we exclude fibers dominated by DIG emission from our Z_{gas} analysis.

Using the data from DIG and HII regions in the Milky Way from the Wisconsin Hα Mapper (WHAM) sky survey (Madsen et al. 2006), Blanc et al. (2009) estimates that fibers with [SII]/H$\alpha \geqslant 0.34$ and with Hα flux below a certain minimum value are 100% dominated by DIG emission. Fibers not satisfying these two conditions include Seyferts, LINER and star-forming regions. In our work, we apply a similar technique using the [SII]/Hα and Hα flux of each individual fiber. We fit a curve for [SII]/Hα vs Hα, and where that curve intersects [SII]/H$\alpha = 0.34$, becomes the minimum Hα flux considered to be 100% DIG emission. We then consider those fibers below this minimum Hα flux to be 100% DIG emission and exclude them from our Z_{gas} analysis.

For our galaxies, we use Figure 6 to illustrate where the DIG is located on the BPT diagrams (left side of Figure 6) and in the galaxies (right side of Figure 6). Most of the DIG dominated fibers occupy the mid-to-upper right side of the BPT diagram. This behavior is expected since high [NII]/Hα or [SII]/Hα line ratios used are associated with DIG emission. As shown on the right side of Figure 6, we find that most of the DIG-dominated emission comes from the outer disks at large radii, in the regions beyond the spiral arms and away from the regions of intense SF. Contamination in fibers of emission from the DIG explains, at least partially, why the outer regions far from the spiral arms and regions of active SF in a galaxy show LINER like emission line ratios on BPT diagrams as seen in Figure 5. This effect has also been observed by Greenawalt et al. (1997) and Hoopes & Walterbos (2003).

In NGC 2903 we calculate the effect of erroneously including DIG when calculating Z_{gas}. The other few IFU studies of Z_{gas} specifically target only bright HII regions, sacrificing spatial sampling to avoid DIG contamination (e.g. see Sánchez et al. 2012). We find that including the DIG dominated fibers only changes the average Z_{gas} from all our diagnostics by at most $\pm$0.1 dex and the slope of the Z_{gas} gradients by $\pm$0.015 dex kpc^{-1}, even in the outer regions of the disk where emission is the most dominated by the DIG. While this is a small effect in NGC 2903, for accuracy we remove all DIG dominated fibers when calculating Z_{gas} in our sample galaxies.

4.3 Computing Star Formation Rates

We can estimate the current star formation rate (SFR) by measuring the intensity of recombination lines such as Hα. UV photons blueward of the Lyman break ionize hydrogen and deposit their energy into the ISM. Eventually the total energy of the Lyman continuum photons absorbed by neutral atomic hydrogen radiates away via recombination lines. Before any SFR can be measured, we correct for reddening in each spectrum due to dust in the target galaxy using the Hα/Hβ line ratio decrement described in Osterbrock & Ferland (2006). Contaminated regions such as Seyfert, LINER, & DIG are masked out, as described in § 4.1 & 4.2 . The SFR for a given fiber is calculated from the luminosity of the Hα line as described by Kennicutt (1998). The SFR varies linearly with the Hα luminosity, given by the following equation:

$$\mathrm{SFR}\ (\mathrm{M}_\odot\ \mathrm{yr}^{-1}) = 7.9 \times 10^{-42} L(H\alpha)\ (\mathrm{erg\ s}^{-1}). \tag{1}$$

We convert the SFR for each individual fiber into a SFR density (Σ_{SFR} M$_\odot$ yr^{-1} pc^{-2}) by dividing the SFR for each fiber by area of the fiber's PSF$_{\mathrm{FWHM}}$ in kpc^2. Table 4 lists the total integrated SFR over our spatial coverage for each galaxy, along with the peak Σ_{SFR}. Radial gradients for Σ_{SFR} are shown on the right side of Figure 9. Although our spatial coverage over the entire disk of a galaxy is incomplete for every galaxy (as seen in Figure 1), most of the SF takes place in the central few kpc so our Hα derived SFRs provide a lower limit to the global SFR of the galaxy. We compare our Hα derived SFRs to global imaging UV or Hα SFRs from the literature (Blanc et al. 2013 and references therein).

SFRs derived from UV are directly measuring the ionizing flux from hot stars, while recombination lines such as Hα indirectly measures SFRs by radiating away the energy the ionizing photons are depositing into the ISM. In the far infrared (FIR) between 40 & 120 μm, the luminosity scales with the SFR because the majority of the FIR light observed is thermal radiation reradiated by dust from absorbed starlight from the most massive stars ($M > 5M_\odot$) (Devereux & Young 1990; Xu 1990). We calculate a global FIR flux F_{FIR} for each galaxy by taking the integrated flux from the IRAS 60 and 100 μm bands and plugging them into the following equation:

$$F_{FIR} = 1.26 \times 10^{-14}(2.58 S_{60} + S_{100}) \tag{2}$$

where S_{60} and S_{100} are the flux in janskys for the 60 & 100 μm IRAS bands (Condon 1992; Helou et al. 1988). We convert the FIR flux (F_{FIR}) to FIR luminosity (L_{FIR}), given the distance to each galaxy. Assuming most of L_{FIR} comes from massive stars ($M > 5M_\odot$), Condon (1992) gives the SFR for massive stars, based on L_{FIR}, to be:

$$\frac{SFR_{FIR}(M > 5M_\odot)}{M_\odot\ \mathrm{yr}^{-1}} = 0.9 \frac{L_{FIR}}{10^{10} L_\odot} \tag{3}$$

To account for lower mass stars ($M < 5M_\odot$), we assume an extended Miller Scalo IMF (Kennicutt 1983; Jogee et al. 2005) and multiply $SFR_{FIR}(M > 5M_{\odot})$ by a scale factor of 4.3 to get the total SFR_{FIR}:

$$\frac{SFR_{FIR}}{M_{\odot}\ \mathrm{yr}^{-1}} = 3.9\frac{L_{FIR}}{10^{10}L_{\odot}} \tag{4}$$

The global FIR luminosities and SFRs we calculate for our galaxies can be seen in Table 4, where the FIR SFRs are larger than the lower limits we calculate using Hα luminosity, as one would expect due to our incomplete spatial coverage.

4.4 Computing the Ionization Parameter q

As seen in the top left & top right of Figure 7, both line ratios R_{23} and [NII]/Hα are dependent on the ionization parameter q. Kewley & Dopita (2002) defines an effective ionization parameter q as the flux of ionizing photons above the Lyman limit (energy >13.6 eV) through the surface of a Strömgren sphere of radius R:

$$q = \frac{Q}{4\pi R^2 n} \tag{5}$$

where Q is the flux of ionizing photons produced at the surface of the central star(s), R is the radius of the Strömgren sphere, and n is the number density of hydrogen atoms.

For each fiber consistent with photo-ionization by SF, we calculate q with several goals in mind: (a) Firstly, we wish to explore how q varies across regions which have different SFR density and are dynamically different (e.g., along the bar versus the inner kpc and outer disk) (see § 5.2 and Figure 8) (b) Secondly, for the Z_{gas} diagnostics where q is explicitly used in the calculations (e.g. R_{23}-KK04), we can estimate the impact of q on Z_{gas}. (c) Thirdly, we wish to compare Z_{gas} diagnostics that do not explicitly include q (R_{23}-Z94, 03N2-PP04, N2-D02, & N2-PP04; Table 5) with those that do, and see if they show different *relative* radial trends (e.g. a negative versus a positive or flat gradient). We discuss our attempt to create a new theoretical [NII]/Hα Z_{gas} diagnostic, which takes into account q, in § 5.1.

The method we use to calculate q (hereafter called Method 1) is to get the Z_{gas} from the N2O2-KDO2 diagnostic using the line ratio [NII]/[OII], which is invariant to the value of q. N^+ and O^+ have similar ionization potentials so the ratio [NII]/[OII] depends little on q, as seen in the bottom left of Figure 7. The line ratio [OIII]/[OII] depends heavily on q, as seen in the bottom right of Figure 7. Once we have Z_{gas}, along with the line ratio [OIII]/[OII], we can calculate q by plugging Z_{gas} and [OIII]/[OII] into the following equations from Kobulnicky & Kewley (2004):

$$y = \log\left(\frac{[\mathrm{OIII}]}{[\mathrm{OII}]}\right) \tag{6}$$

$$Z = log(\mathrm{O/H}) + 12 \tag{7}$$

$$\log q = \frac{32.81 - 1.153y^2 + Z(-3.396 - 0.025y + 0.1444y^2)}{4.603 - 0.3119y - 0.163y^2 + Z(-0.48 + 0.0271y + 0.02037y^2)} \tag{8}$$

We discuss an alternative method (hereafter method 2) for finding q in Appendix A. This method gets q from the [OIII]/[OII] line ratio (as does in Method 1), but it solves iteratively for Z_{gas} and q using [OIII]/[OII], [NII]/[OII], and R_{23}. Both methods give similar results for q. Several of the other Z_{gas} diagnostics (Table 5) also make corrections for q using the [OII] and [OIII] lines, as discussed in Appendix B.

4.5 Computation of Z_{gas} Using Different Diagnostics

The most direct method for computing Z_{gas} from emission line fluxes involves measuring the electron temperature (T_e) from the flux ratio of the [OIII] lines: [O III]λ4363 to [O III]$\lambda\lambda$4959,5007. By plugging the measured value of T_e into a classical HII region model, one finds Z_{gas} (Osterbrock & Ferland 2006). Our VENGA observations do not go deep enough to detect the emission of the [O III]λ4363 line with high enough S/N to use the direct T_e method. Instead, we make use of stronger emission lines that we can easily detect.

The broad wavelength coverage and good spectral resolution of VENGA allows us to explore Z_{gas} across spatially resolved galactic components, and star-forming regions, using seven different Z_{gas} diagnostics based on several calibrations of four Z_{gas} indicators, as shown in Table 5. The four indicators (R_{23}, N202, 03N2 and N2; Table 5) are based on the following strong emission line ratios: R_{23} = ([OII]+[OIII])/Hβ, [NII]/[OII], ([OIII]/Hβ)/([NII]/Hα), and [NII]/Hα.

For each of the line ratios, we use one or more *calibrations* that are either "empirical" or "theoretical." Empirical calibrations involve calibrating the strong emission line ratios observed in HII regions to the Z_{gas} derived from the direct T_e method using multi-slit spectroscopy. Theoretical Z_{gas} indicators base their line ratios on stellar population synthesis, nebular photo-ionization, and radiative transfer models reviewed in Kewley & Dopita (2002) and Dopita et al. (2000).

We provide a brief summary of the models here. The models start with the stellar population synthesis codes PEGASE (Fioc & Rocca-Volmerange 1997) and STARBURST99 (Leitherer et al. 1999) to generate single stellar populations with varying metallicities. The light from these synthetic stellar populations creates the ionizing UV radiation field. The resulting ionization field is put into the shock and photo-ionization code MAPPINGS III (Sutherland & Dopita 1993) which is plane-parallel and includes treatments for dust and elemental depletion. These photo-ionization models were calculated for a large range of Z_{gas} between 0.05-3 times solar or log(O/H)+12=7.6-9.4, and ionization parameters $\log(q)$ =6.7-8.5. These ranges in Z_{gas} and q are sufficient for the theoretical Z_{gas} calibrations to cover Z_{gas} and q for our subsample of VENGA galaxies.

To calculate Z_{gas}, we start by making a signal-to-noise cut of S/N > 5 for the Balmer decrement to ensure we have a good extinction correction, and S/N > 3 for all the lines used for each Z_{gas} diagnostic. We exclude all fibers that are LINER or Seyfert on the BPT diagrams (§ 4.1), along with all fibers flagged as DIG dominated (§ 4.2). After applying the empirical and theoretical calibrations to the four different Z_{gas} indicators, we use a total of seven different Z_{gas} *diagnostics* to determine Z_{gas} for each individual fiber in regions of our galaxies that are primarily photoionized photons from massive stars. These different Z_{gas} diagnostics are all systematically offset from each other in their absolute values for Z_{gas}. The reader should keep in mind that our diagnostics give *relative* Z_{gas}, but Kewley & Ellison (2008) provides prescriptions for converting between the various Z_{gas} diagnostics. All seven of the Z_{gas} diagnostics we use are summarized in Table 5, and how Z_{gas} is calculated for each diagnostic is discussed in detail in Appendix B and Kewley & Ellison (2008).

Four of the diagnostics are theoretical, with three that are based on the R_{23} ratio and by McGaugh (1991); Kobulnicky & Kewley (2004); Zaritsky et al. (1994), and one is based on the [NII]/[OII] line ratio by Kewley & Dopita (2002) (hereafter abbreviated as R_{23}-M91, R_{23}-KK04, R_{23}-Z94, & N2O2-KD02). Two of the theoretical diagnostics correct for the ionization parameter q, R_{23}-M91 uses the [OIII]/[OII] ratio directly in its functions to correct for q, and R_{23}-KK04 calculates q by assuming an initial Z_{gas} and iterating between q and Z_{gas} until there is a convergence (see Appendix B). The R_{23}-Z94 diagnostic does not correct for q. The N2O2-KD02 diagnostic also does not correct for q, but this line ratio is invariant to to the value of q (see bottom left of Figure 7).

The remaining three diagnostics are all fits to empirical multi-slit spectroscopy of HII regions. There is one based on the [OIII]/[NII] line ratio by Pettini & Pagel (2004), and two based on the [NII]/Hα line ratio by Denicoló et al. (2002) and Pettini & Pagel (2004) (hereafter abbreviated as O2N2-PP04, N2-D02, & N2-PP04).

It is extremely important to have multiple Z_{gas} indicators in order to break degeneracies and explore the systematics between indicators. As shown in the top left of Figure 7, the R_{23} indicator is degenerate with two possible ranges of Z_{gas} for every R_{23} value. The R_{23} ratio is sensitive to Z_{gas} because [OII] and [OIII] are sensitive to the electron temperature (T_e) of the nebula. HII regions have temperatures typically around 10^4 K, so it is hot enough to collisionally excite the forbidden [OII] and [OIII] transitions. On the lower branch where R_{23} rises with Z_{gas}, the main coolant is oxygen and the strength of the [OII] & [OIII] lines increases with oxygen abundance. On the higher branch, R_{23} falls with Z_{gas} because at high Z_{gas}, cooling is dominated by far-IR fine structure metal lines and the electron temperature becomes too low to collisionally excite the the [OII] & [OIII] lines. Adding in the [NII]/[OII] line ratio, as seen in the bottom left of Figure 7, can break this degeneracy since [NII]/[OII] rises with Z_{gas} and tells us if Z_{gas} is high or low to break the double valued degeneracy of R_{23}.

5 RESULTS AND DISCUSSION

5.1 Comparison Between Different Z_{gas} Diagnostics

After excluding fibers in the Seyferts and LINER region of the BPT diagram (§ 4.1) and DIG-dominated fibers (§ 4.2), we compute the ionization parameter q (§ 4.4) and the seven different Z_{gas} diagnostics (R_{23}-KK04, R_{23}-M91, R_{23}-Z94, N2O2-KD02, O3N2-PP04, N2-D02 and N2-PP04; see Table 5) for seven of the nine subsample galaxies (NGC 0337, 0628, 2903, 3938, 4254, 5194, & 5713). For the other two galaxies we have reduced, NGC 2775 shows very little emission from the gas so we are unable to get Z_{gas}, and NGC 1068 is a known Seyfert galaxy with most of the fibers covering it showing excitation from AGN and/or shocks. Thus, we do not include our Z_{gas} results for NGC 1068 & 2775 in this study.

Currently, one long-standing major issue in Z_{gas} studies is that there are systematic offsets between *absolute* values of Z_{gas} given by the different diagnostics. Attempts have been made to reconcile the differences between the diagnostics (for example see Kewley & Ellison 2008; Kewley & Dopita 2002), but the issue is far from settled. Another problem is that different Z_{gas} indicators may show different *relative radial gradients* in Z_{gas} (e.g., a negative versus a positive or flat gradient). In this work, we are able to compute 2D maps and radial gradients of q, and of these seven Z_{gas} diagnostics, as well as of related properties such as the extinction-corrected SFR. This allows us to explore possible differences between radial trends of different Z_{gas} diagnostics, and investigate if some of these differences might be tied to the dependence of some Z_{gas} diagnostics on q.

Figure 8 shows a montage of 2D maps of q and six Z_{gas} diagnostics (R_{23}-KK04, R_{23}-M91, N202-KD02, O3N2-PP04, N2-D02, & N2-PP04), along with the stellar continuum and extinction-corrected Hα-based SFRs for our VENGA subsample. Our seven galaxies show a range in global SFR of $1.2 \rightarrow 11$ $M_\odot$ yr^{-1}. Figure 9 shows the azimuthally-averaged value of q and the SFR per unit area ($\Sigma_{\rm SFR}$): we find that for NGC 0628, 2903, 3938, & 4254, q and $\Sigma_{\rm SFR}$ tend to correlate fairly well while in NGC 0337 and NGC 5713, $\Sigma_{\rm SFR}$ falls steeply with radius while q shows little variation. This is possibly due to a lower limit on log(q) $>\sim$ 7.0. Similar lower limits in q have been seen by Shields (1990) and Dopita et al. (2000). This lower limit for q does not appear in theoretical simulations of HII regions and the detailed physics behind it are currently unknown.

Figure 10 show deprojected radial Z_{gas} gradients based on all seven Z_{gas} diagnostics for NGC 0337, 0628, 2903, 3938, 4254, 5194, & 5713. In terms of the *shape* of the radial profile of Z_{gas}, the seven Z_{gas} diagnostics show fairly good agreement beyond the inner 1-2 kpc, and yield flat to moderately negative gradients (Figure 10). As shown in Table 6, the gradients are shallow and in dex kpc^{-1}, they range from (-0.005 to -0.0275) in R_{23}-KK04, (-0.0063 to -0.0268) in N2O2-KD02 and (-0.0093 to 0.101) in N2-PP04, while in dex (R/R25)$^{-1}$ they range from (-0.007 to -0.32) in R_{23}-KK04, (-0.049 to -0.404) in N202-KD02, and (-0.27 to 0.138) in N2-PP04.

Next we compare how the *absolute values of* Z_{gas} vary across the eight Z_{gas} diagnostics:

(i) *R_{23} Z_{gas} diagnostics:* The three R_{23} Z_{gas} diagnostics show a similar shape in the radial profile of Z_{gas}. There is good agreement within 0.1 to 0.2 dex in the absolute values of Z_{gas} given by R_{23}-KK04, R_{23}-M91, and R_{23}-Z94. R_{23}-Z94 is a theoretical calibration that does not correct for q, while R_{23}-KK04 and R_{23}-M91 are theoretical calibrations, which explicitly calculate q in each fiber based on the the [OIII]/[OII] ratios (see Appendices A & B) and use q to correct Z_{gas}. The fact that the R_{23}-Z94 Z_{gas} diagnostics do not correct for q, but yet gives similar Z_{gas} to R_{23}-KK04 and R_{23}-M91 is likely due to the fact that we are upper branch of R_{23} (see top right of Figure 7), where there is a small dependence on q.

(ii) *The N2O2-KD02 Z_{gas} diagnostic:* The N2O2-KD02 & O3N2-PP04 diagnostics show the least amount of scatter out of all eight Z_{gas} diagnostics. N2O2-KD02 gives Z_{gas} values similar to the three main R_{23} diagnostics (R_{23}-KK04, R_{23}-M91, & R_{23}-Z94). We note that N2O2-KD02 is a theoretical calibration that uses the [NII]/[OII] line ratio, which has little dependence on q (Figure 7).

(iii) *The O3N2-PP04 Z_{gas} diagnostic:* O3N2-PP04 gives a Z_{gas} that is systematically lower by 0.2 to 0.3 dex compared to the three main R_{23} diagnostics. O3N2-PP04 uses the [NII]/[Hα] and [OIII]/[Hβ] line ratios and is an empirically-based calibration that does not correct for local variations in q. It is possible that the dependence of [NII]/[Hα] on q suggested by Figure 7 may help explain the Z_{gas} offset between O3N2-PP04 and the other convergent diagnostics (N2O2-KD02, R_{23}-KK04, R_{23}-M91, and R_{23}-Z94).

(iv) *The N2-D02 and N2-PP04 Z_{gas} diagnostics:* The N2-D02 and N2-PP04 Z_{gas} diagnostics use the [NII]/Hα line ratio and are based on empirical calibrations that do not correct for local variations in q. N2-PP04 gives a Z_{gas} that tends to be 0.2 to 0.4 dex lower compared to to the three main R_{23} diagnostics (R_{23}-KK04 ands R_{23}-M91, and R_{23}-Z94), while N2-D02 can show a smaller offset of 0.1-0.2 dex. It should be noted that for the N2-PP04 diagnostic, we only consider fibers with $-2.5 < \log([\mathrm{NII}]/H\alpha) < -0.3$, hence there is a cutoff at high log(O/H)+12 when compared to the N2-D02 diagnostic. Furthermore, in the inner 2 kpc of some of our galaxies, the radial gradients in Z_{gas} given by N2-D02 and N2-PP04 can differ from those given by other diagnostics. For instance, in NGC 2903, the first five Z_{gas} diagnostics give a moderately negative to flat Z_{gas} gradient in the inner 1.5 kpc radius, but N2-KD02 and N2-PP04 give a slightly positive gradient, which then inverts (see Figure 10). A milder example can be seen in the form of a negative central gradient in NGC 4254. We have looked into two possibilities to explain why the absolute value of Z_{gas} (and possibly its profile shape too) from the N2-D02 and N2-PP04 diagnostics differ from that given by the other diagnostics. The [NII]/Hα line ratio is subject to saturation at high Z_{gas}, and is also sensitive to the value of q, both of which can be seen in Figure 7. To this end, we attempted to calculate Z_{gas} by interpolating over the theoretical [NII]/Hα curves from Kewley & Dopita (2002) which uses the [NII]/Hα ratio and corrects explicitly for local variations in q, using the q we calculated based on the [OIII]/[OII] line ratio via Method 1 (§ 4.4). We find that the shape and absolute value of the gradients does not change significantly from the empirical N2-D02 and N2-PP04 diagnostics, suggesting that correcting for q does not appreciably affect the the values we get for Z_{gas} for the N2 diagnostics. It is clear that the saturation of [NII]/Hα at high Z_{gas} makes it difficult to calculate Z_{gas} beyond log(O/H)+12 > 9.1, and future theoretical calculations relating [NII]/Hα, q, and Z_{gas} might help better probe the discrepancies between the N2 and other Z_{gas} diagnostics.

5.2 Resolved Distribution of Z_{gas}, q, and SFR Across Different Galactic Components

The high spatial resolution (with a median $\mathrm{PSF_{FWHM}}$ of 298 pc and a median (R_e-bulge/$\mathrm{PSF_{FWHM}}$) of 3.63) and IFU data coverage over a large fraction of the galaxy's disk (median f_{R25} of 0.66) in our sample allows us to resolve individual galaxy components such as the bulge (classical and pseudo), bar, and outer disk, and thereby explore how Z_{gas} varies across these components.

As discussed in § 5.1, of the nine galaxies reduced in our sample, we have valid Z_{gas} measures for seven galaxies (NGC 0337, 0628, 2903, 3938, 4254, 5194, & 5713), while NGC 1068 and NGC 2775 are excluded. Four of these galaxies are barred (NGC 0337, 2903, 4254, & 5713), two are unbarred (NGC 0628 & 3938), and one is unbarred and interacting (NGC 5194). Table 6 gives the gradients for all seven galaxies using the R_{23}-KK04, N2O2-KD02, & N2-PP04 Z_{gas} diagnostics. The gradients are shallow: in units of dex kpc^{-1}, they range from (-0.005 to -0.0275) in R_{23}-KK04, (-0.0063 to -0.0268) in N2O2-KD02 and (-0.0093 to 0.101) in N2-PP04, while in dex (R/R25)$^{-1}$ they range from (-0.007 to -0.32) in R_{23}-KK04, (-0.049 to -0.404) in N202-KD02, and (-0.27 to 0.138) in N2-PP04. For comparison, the Z_{gas} gradient for the Milky Way was determined by Shaver et al. (1983) using the R_{23} ratio and finds the gradient to be -0.07 ± 0.015 dex kpc^{-1}.

Figure 11 shows the radial variation of Z_{gas} as a function of function of radius in kpc and $R/R25$, respectively using the R_{23}-KK04 diagnostic. For our galaxies, Figure 8 shows a montage of 2D maps of the stellar continuum of galactic components, the extinction-corrected Hα-based SFRs, q, and six Z_{gas} diagnostics. The 2D maps and Figure 9 allow a more detailed investigation of how q and Z_{gas} relate to local processes (SF, shocks, etc.) in different parts of the barred potential. We find an odd behavior in the 2D maps between the two Z_{gas} diagnostics based on the [NII]/Hα ratio (N2-D2, N2-PP04) and the other Z_{gas} diagnostics shown. In NGC 2903, the N2-D2, N2-PP04 Z_{gas} diagnostics appear to show lower Z_{gas} along the leading edges of the bar and along the spiral arms than on the trailing edge, while the opposite behavior is seen in the other four Z_{gas} diagnostic (Figure 8) Similarly flipped behavior is clearly seen in NGC 4254 & 5713. It is possible that this inconsistency may be related to the differences we saw in the central Z_{gas} gradients between the N2-D2, N2-PP04 Z_{gas} diagnostics and the other Z_{gas} diagnostics (§ 5.1).

It is remarkable that all the galaxies in our subsample including unbarred, barred, and interacting galaxies exhibit such flat Z_{gas} gradients across all their galactic components. In § 5.3 we discuss our results for barred and unbarred galaxies and the physics behind how bars can flatten Z_{gas} gradients, § 5.4 compares the Z_{gas} gradients between isolated and interacting galaxies and explores how interactions flatten Z_{gas} gradients, § 5.5 compares our low redshift Z_{gas} gradients to those found at higher redshifts, and § compares our results to theoretical models to better understand the detailed physics behind how Z_{gas} gradients can flatten.

5.3 Comparison of Z_{gas} Between Isolated Barred and Unbarred Galaxies

Are Z_{gas} gradients in *present-day* barred galaxies shallower than in present-day unbarred galaxies at a given Hubble type or stellar mass? This dataset does not presently exist, but we make a first order attempt with existing empirical studies. The first requirement is high-quality spatially resolved, finely-sampled Z_{gas} maps across all the galactic components such as the bulge, bar, and disk. Our maps provide the best data of this sort to date. Our subsample of VENGA galaxies includes Z_{gas} results for four barred (NGC 0337, 2903, 4254, & 5713) and two unbarred (NGC 0628 & 3938) isolated galaxies.

Among the four barred galaxies, whose Hubble types span Sb, Sbc, Sc, and Sd, the galaxy of latest Hubble type, NGC 0337 (Sd), has an absolute value of Z_{gas} that is lower by 0.2 to 0.4 dex compared to the galaxies of earlier Hubble types. This is easily seen at the top of Figure 11 where we overplot the Z_{gas} gradients of all nine of our galaxies in our VENGA subsample. The gradient for NGC 0337 does not appear to be any steeper than the other galaxies (see Table 6). While it is difficult to draw conclusions on trends in morphology based on only this one galaxy, We are probably seeing a manifestation of the mass-metallicity relation since NGC 0337 is an Sd galaxy with the lowest stellar mass ($\sim 8 \times 10^9$ M$_\odot$ yr^{-1}, Blanc et al. 2013) in our subsample, and thus expected to have the lowest metallicity.

The most significant feature, as seen in Figure 11, is that for all four barred galaxies, *the Z_{gas} gradient is primarily flat and sometimes slightly negative along the bar and in the outer disk beyond the bar end* (Figure 11). In the inner 1-2 kpc radius, the behavior of Z_{gas} differs across the four barred galaxies with Z_{gas} rising toward the center in NGC 2903 and 0337, but staying flat in NGC 4254 and NGC 5713.

The way a barred galaxy's existing Z_{gas} gradient changes with time depends on the gas inflow rate, SFR, and outflow rate at each position in the galaxy. We therefore discuss how our results of shallow Z_{gas} gradients may be tied to the gas inflow and outflow expected in three different dynamical regions of a barred potential:

(i) In a barred potential, gas between the corotation resonance (CR) and outer Lindblad resonance (OLR) of the bar is driven *outward* by gravitational torques (e.g. reviews by Buta & Combes 1996 and by Jogee 2006). If a galaxy starts out with a negative Z_{gas} gradient, such an outflow would tend to flatten the Z_{gas} gradient beyond the bar end, in the outer disk. This may be part of the reason for the flat Z_{gas} gradient we are seeing in the outer disk of these barred galaxies.

(ii) Inside the corotation resonance (CR) of the bar, gas is shocked on the leading edge of the bar and driven *inward* toward the inner kpc by gravitational torques. If the gas inflow rate supersedes the SFR along the bar, it will flatten any existing negative Z_{gas} gradient along the bar. This is more likely to happen along strong bars, which not only drive large gas inflow rates, but also have large non-circular motions and shear that leads to a low SFR per unit mass of molecular gas (e.g., in NGC 4569 (Jogee et al. 2005), in M83 (Handa et al. 1991), and in NGC 5383 (Tubbs 1982)). This may be part of the reason for the flat Z_{gas} gradient we see along the bar.

(iii) As the gas inflows along the bar toward the inner few kpc, its subsequent fate depends of whether the barred galaxy has one of more inner Lindblad resonances (ILRs)[1]: (a) If the barred potential has no ILRs, the inflowing gas reaches the central part of the galaxy. There it can flatten any existing negative Z_{gas} gradient, but it can also lead to central starbursts which metal-enrich the gas, and to starburst-driven outflows. (b) If the barred potential has one or more ILRs called the outer ILR (OILR) and inner ILR (IILR), then the gas inflowing along the bar does not reach the center, but piles up in a ring inside

[1] In the limit of epicyclic approximation for weak bars, one or more ILRs exist if the galaxy has a significant central mass density such that the peak of (Ω - $\kappa/2$) exceeds the bar pattern speed. In a more general sense, ILRS exist if the x_2 family of periodic stellar orbits are present in the inner regions of the bar.

the OILR (or between the ILRs if two ILRs exist). In spirals of intermediate Hubble types, the IILR is typically at a radius of 200-400 pc and and the OILR is typically at a radius of 1-2 kpc (e.g. see Buta & Combes 1996; Jogee et al. 1999, 2005; Kormendy & Kennicutt 2004). In such a case, the lower metallicity gas will not reach the central kpc and will not flatten any existing negative Z_{gas} gradient. We checked whether the negative Z_{gas} gradient in the inner kpc of NGC 2903 and 0337, and flat Z_{gas} gradient in the inner kpc of NGC 4254 and NGC 5713 may be related to the presence of (resolved) ILRS in the former class of galaxies. We find that NGC 2903 contains an inner ring, evidence that it has IIRLs (Alonso-Herrero et al. 2001). NGC 0337 does not show any evidence for rings but might be undergoing a possible minor merger or interaction, where the "southern knot" seen in both stellar continuum and Hα emission might be the merging system as suggest by Sandage & Bedke (1994). It appears to be associated with a kink in the Hα isovelocity contours as seen in Figure 3. NGC 4254 & 5713 show no evidence for rings or ILRs. We note that the large distance of NGC 5713 results in a $\mathrm{PSF_{FWHM}}$ of $\sim$ 700 pc, making it less likely that we would resolve its ILRS, even if they are present, thereby resulting in the artificial smearing/flattening of the observed Z_{gas} gradient there.

Ellison et al. (2011) investigated 294 barred and 588 unbarred SDSS DR4 galaxies via single fiber spectroscopy which probes the inner few kpc, and they find that the central regions of the barred galaxies in their sample show enchanted SFRs that are higher by $\sim$ 60% when compared to the unbarred galaxies in their sample, and that this enhanced SFR is evidence that radial gas mixing induced by bars is driving SF in the center of barred galaxies. Figure 9 shows that the peak $\log(\Sigma_{SFR})$ in the central kpc for our four isolated barred galaxies (NGC 0337, 2903, 4254, & 5713) are $\log(\Sigma_{SFR}) \sim -1$, while our two isolated unbarred spirals (NGC 0628 & 3938) range in $\log(\Sigma_{SFR})$ from $\sim$ -2 to -1.5 which are consistent with the SFR results from Ellison et al. (2011). Our global Hα and FIR based SFRs for our subsample of VENGA galaxies seen in Table 4 do not show a clear correlation between SFR and whether the galaxy is barred or unbarred, suggesting that the effects of bars on SFRs are mostly confined to the central few kpc.

The absolute value of Z_{gas} in our VENGA galaxies does not appear to exhibit any trend between our barred and unbarred isolated spirals. Ellison et al. (2011) claims that Z_{gas} in the central few kpc is higher by $\sim$ 0.006 dex in barred galaxies, when compared to unbarred galaxies in their sample. Nearly all of our VENGA subsample exhibit a value of Z_{gas} of log(O/H)+12 $\sim$ 9.1 in the center (with the exception of our single Sd galaxy NGC 0337 which exhibits systematically lower Z_{gas} by $\sim$ 0.2 dex), but the scatter between the galaxies and even between individual fibers is similar to or greater than 0.006 dex, so it is difficult to draw conclusions on such minute differences between the isolated barred and unbarred spirals from our VENGA subsample.

Previous studies have claimed that Z_{gas} gradients are flatter in isolated barred spiral galaxies than those that are unbarred. Vila-Costas & Edmunds (1992) claims to find that barred spirals exhibit flatter Z_{gas} gradients than unbarred spirals, although their classification of galaxies with partially visible bars (labeled as "mixed") exhibit a large amount of scatter between flat to steep gradients. Martin & Roy (1994) studied Z_{gas} gradients across three barred spiral galaxies using spectrophotometry and found shallow gradients ($\sim$ -0.03 to -0.05 dex kpc^{-1}). They claim that the gradients of unbarred spiral galaxies are steeper ($\sim$ -0.1 dex kpc^{-1}), although there is a large amount of scatter between the individual galaxies. This early result and the large amount of scatter in the observed gradients might be caused by several issues. The large scatter in Z_{gas} gradients in both barred and unbarred spirals might be caused by correlations between the gas flow, SF, and enrichment induced by the bar, the bar's strength, and the galaxy's morphology (Dutil & Roy 1999; Zaritsky et al. 1994; Martin & Roy 1994). There is some evidence from these previous studies that bar strength correlates with Z_{gas} gradients (e.g. see Martin & Roy 1994 who finds a correlation between bar ellipticity and Z_{gas} gradients). Nearly all other studies of Z_{gas} target bright dense HII regions to ensure the gas is ionized by young massive stars, sacrificing their spatial sampling. Vila-Costas & Edmunds (1992) finds a correlation between Z_{gas} and surface density, showing Z_{gas} presumably traces SFR. Since all these studies target the brightest and densest HII regions, it is possible this introduces a systematic bias in the Z_{gas} gradient results, especially for barred galaxies where bars induce SF far out from the central few kpc in a galaxy's disk. To achieve fine spatial sampling, we do not distinguish bright dense HII regions from more diffuse regions in this VENGA study, and instead mask out regions not photoionized by massive stars using BPT diagrams and identifying DIG (see § 4.1 & 4.2) avoiding possible systematics associated with only targeting the brightest HII regions.

Figures 12 & 13 use the R_{23}-KK04 and N202-KD02 diagnostics respectively to compare the Z_{gas} radial profiles of our barred and unbarred VENGA galaxies to those of isolated barred and unbarred galaxies from the Rupke et al. (2010b) study, which uses slit spectroscopy. Rupke et al. (2010b) used this sample of isolated galaxies as a control sample to compare against their sample of interacting galaxies. Our four VENGA isolated barred galaxies (NGC 0337, 2903, 4254, & 5713) show shallow Z_{gas} gradients: in dex kpc^{-1}, they range from (-0.0103 to -0.0275) in R_{23}-KK04 and (-0.013 to -0.034) in N2O2-KD02, while in dex (R/R25)$^{-1}$ they range from (-0.17 to -0.222) in R_{23}-KK04 and (-0.17 to -0.327) in N202-KD02. Our two VENGA isolated unbarred galaxies (NGC 0628 & 3938) also show similarly shallow Z_{gas} gradients in dex kpc^{-1} and possibly slightly steeper gradients in dex (R/R25)$^{-1}$: in dex kpc^{-1}, they range from (-0.0201 to -0.0225) in R_{23}-KK04 and (-0.0268 to -0.0200) in N2O2-KD02, while in dex (R/R25)$^{-1}$ they range from (-0.30 to -0.32) in R_{23}-KK04 and (-0.280 to -0.404) in N202-KD02. While our unbarred galaxies are also remarkably flat, it is possible that past interactions and bars have led to radial mixing of the gas flattening the gradient in Z_{gas} to what we see today for our unbarred spirals. It is clear from Figures 12 & 13 that our VENGA-based Z_{gas} radial profiles are of much higher quality (in terms of spatial sampling and scatter) than the profiles from Rupke et al. (2010b), and this makes a direct apples-to-apples comparison with that dataset difficult. At face value, the three unbarred spiral galaxies in Rupke et al. (2010b) exhibit gradients in R/R25 of ~ -0.5 dex (R/R25)$^{-1}$, while their barred galaxies exhibit an even larger range of gradients of $\sim$ -0.2 to -0.8 dex (R/R25)$^{-1}$. Again, we find that both barred and unbarred galaxies show similarly shallow Z_{gas} gradients, suggesting that unbarred galaxies in the present day universe have their gradients flattened by the same processes that flatten gradients for currently barred galaxies such as radial gas flows induced by bars that have existed in the past, interactions, mergers, and feedback. Previous IFU studies of nearby spirals have been used to study Z_{gas}. Our result has been seen in the previous IFU study of nearby face on spiral galaxies by Sánchez et al. (2012) who uses both PINGS and CALIFA data to show the Z_{gas} gradients in their sample have no correlation with whether the galaxies are barred or unbarred.

Previously existing bars in currently unbarred galaxies are one compelling process that could have induced radial gas flows in the past that may have contributed to the flat Z_{gas} gradients we observe today. Cosmologically motivated simulations of disk galaxies show that bars have undergone two distinct phases of development in early and late times (Romano-Díaz et al. 2008; Heller et al. 2007). The first bars that formed in the first few Gyr of a galaxy were induced by asymmetries in the dark matter halos, decaying and reforming quickly as the disks are built up over the first few Gyr via major and minor mergers. Early bars exist in almost all simulated galaxies, and were dominated by strong radial gas flows. At later times around 5-7 Gyr, bars become dominated by stars and are formed primarily through tidal interactions. These late time bars are typically long lived ($\sim$ 5-10 Gyr), as suggested by Jogee et al. (2004).

Observations can currently only probe these later bars and accurate determination of bar fractions for non-local (z > 0) galaxies requires large complete samples and high spatial resolution. Jogee et al. (2004) found for a sample of $\sim$ 250 galaxies imaged with the HST ACS, that the strong bar fraction was $\sim$ 30% out to $z \sim 1$ (6-8 Gyr ago). In the COSMOS survey, Sheth et al. (2008) finds evidence for evolution of increasing bar fractions of all strengths in $\sim$ 2500 galaxies from 10-30% from $z \sim 0.8$ to $z = 0$, and Cameron et al. (2010) finds that for a mass limited sample the low mass galaxies build bars up to $z \sim 0.2$ while high mass galaxies have fairly constant bar fractions out to $z \sim 1$. Previous existing bars in currenly unbarred local galaxies (e.g. NGC 0628 & 3938 in our subsample) are one possible way radially mixed the gas leading to the flat Z_{gas} gradients we see today. In the next § 5.4, we discuss the possibility of interactions and mergers as another mechanism for flattening Z_{gas} gradients. While our results are compelling, a full study of the difference in gradients between barred and unbarred spirals requires a large sample with the superb data quality and spatial sampling such as VENGA, data that future IFU surveys may provide.

5.4 Comparison of Z_{gas} to Interacting Spiral Galaxies

Simulations (e.g., Hernquist & Mihos 1995; Mihos & Hernquist 1996) indicate that large gas inflows are generated during tidal interactions and mergers (typically via gravitational torques from induced stellar bars and tidal torques directly from the companion). It has been suggested that these gas inflows can flatten Z_{gas} gradients by causing metal-poor gas in the outer disk to stream inwards, depressing Z_{gas} in the central few kpc and flattening the gradient (Kewley et al. 2006a; Rupke et al. 2010a).

Figures 14 & 15 compares the radial Z_{gas} profile of our non-interacting VENGA galaxies, our one interacting VENGA galaxy NGC 5194, and the interacting galaxies from Rupke et al. (2010b) using both the the R_{23}-KK04 and N2O2-KD02 diagnostics. The sample of interacting galaxies from Rupke et al. (2010b) was selected to have mass ratios close to unity (1:1 to 1:3) and have undergone only the first passage and not be in the later stages of merging. The radial Z_{gas} gradients found in Rupke et al. (2010b) interacting galaxies span a large range in radii from < 1.0 R25 to out to 2.0 R25. Rupke et al. (2010b) clips the gradients in their control sample to $\leqslant$ 1.5 R25, and all the gradients in our subsample of VENGA galaxies go out to a radius of $\lesssim$ 1.0 R25. Rupke et al. (2010b) finds that the gradients for their control sample of non-interacting spiral galaxies can be approximated with straight lines, so presumably comparisons of their control sample of non-interacting galaxies and the non-interacting galaxies in our VENGA subsample should not be significantly affected by how far the data probes out in radius. Again it is difficult to draw robust conclusions, given the difference in quality of the data and the large scatter. Rupke et al. (2010b) finds that on average, their sample of interacting galaxies have flatter Z_{gas} gradients than their control sample of isolated spiral galaxies. They cite that the median Z_{gas} gradient using the N2O2-KD02 diagnostic for the interacting galaxies is -0.23±0.03 dex (R/R25)$^{-1}$ while their control sample exhibits a median gradient of -0.57±0.05 dex (R/R25)$^{-1}$. Another study by Ellison et al. (2011) of eight interacting galaxies has a median gradient of -0.25±0.02 dex (R/R25)$^{-1}$, in agreement with the results from Rupke et al. (2010b). The gradients for our non-interacting VENGA galaxies appear to fall somewhere in between, with a median value of -0.27±0.02 for the N2O2-KD02 diagnostic. The gradient for our one interacting VENGA galaxy (NGC 5194) has the flattest gradient in our dataset ($-0.049 \pm 0.0.3$ dex (R/R25)$^{-1}$, see Table 6), although note that the gradients in our non-interacting VENGA galaxies are also quite flat so it is difficult to draw conclusions from our dataset. Future IFU observations of other interacting galaxies will help settle this matter. The gradient for our interacting galaxy NGC

5194 shows slight enhancement in Z_{gas} at a radius of $\sim$ 9 kpc or 0.7 R25, appearing to coincide with enhanced Z_{gas} in the spiral arms, possibly due to previous SF induced by the interaction with the companion galaxy, as seen in Hα derived SFR in Figure 9 and suggested by Mentuch Cooper et al. (2012). Although our sample only includes one interacting galaxy, It appears to be consistent with the idea that interactions are one mechanism that can drive strong radial gas flows and efficiently flatten Z_{gas} gradients. In § 5.5 we discuss the evolution of Z_{gas} gradients from high to low redshift where the gradients appear to be flattening over cosmic time. Multiple interactions, along with bars, and major and minor mergers throughout the history of a galaxy are all mechanisms that can lead to this observed flattening.

5.5 Comparison of Z_{gas} Gradient Between Low and High Redshift Galaxies

High redshift studies lack the spatial resolution to separate out different galactic components and excitation regions, but recent work using gravitational lensing (Yuan et al. 2011) and adaptive optics (Swinbank et al. 2012) has begun to study radial metallicity gradients at higher redshifts. These observations suggest that Z_{gas} gradients are flattening over cosmic time.

To study how Z_{gas} evolves with redshift, Figure 16 compares the Z_{gas} gradients of our subsample of z$\sim$ 0 VENGA spirals to that of a gravitationally lensed galaxy Sp1149 at $z \sim 1.5$ (Yuan et al. 2011), and another gravitationally lensed galaxy, the "clone arc", at $z \sim 2$ (Jones et al. 2010). We use the N2-PP04 Z_{gas} diagnostic as it is common to both low and high redshift systems. The radial extent of the galactic disk changes with redshift and among the different Hubble types, so we compare the Z_{gas} gradients using the R/R25 scale in the top panel. Since some systems do not have R25 reported, we also compared using radius in kpc in the bottom panel. Figure 16 clearly shows that the Z_{gas} gradients are markedly shallower for all our $z \sim 0$ galaxies than in the higher redshift galaxies, Sp1149 ($z \sim 1.5$) and the "clone arc" ($z \sim 2$). This is consistent with results reported by Yuan et al. (2011), who compares to slit based $z \sim 0$ spectroscopic data. We interpret these observations as evidence that Z_{gas} gradients are flattening over cosmic time.

There are two possible processes that can flatten Z_{gas} gradients. One is via radial gas mixing, as discussed in § 5.3 & § 5.4. The other way is by assembling disks "inside-out," as in the classic inside-out disk formation scenario, first assembling their halos around compact dense cores, followed by galaxy mergers or accretion of gas dominating the build-up of the outer regions over the past 10 billion years (Chiappini et al. 1997; Magrini et al. 2007; Weinzirl et al. 2011; van Dokkum et al. 2010). We look in more detail at simulations in § 5.6.

5.6 Comparison of Z_{gas} Gradient to Theoretical Models

To get a better understanding of the underlying physics causing the flattening of Z_{gas} gradients over cosmic time, we compare our shallow VENGA Z_{gas} gradients to several theoretical models. Current models of the chemical evolution of spiral galaxies are only in the early stages of beginning to constrain the detailed baryonic physics involved, and the constraints put into these current models are driven by observations of empirical Z_{gas} gradients at low and high redshifts, such as those for our VENGA subsample.

We start by comparing our Z_{gas} gradients to those derived by the updated Boissier model. The Boissier model was first employed by Boissier & Prantzos (1999) to simulate the chemical evolution of the Milky Way's disk, and was then generalized to other disks in Prantzos & Boissier (2000) by allowing the rotation curve and dimensionless spin parameter to scale. The scaling laws for the rotation curve and dimensionless spin parameter are deduced from ΛCDM simulations of disk formation by Mo et al. (1998). In the Boissier model, a single disk is modeled as a set of independent concentric rings with no radial inflows or outflows. The stellar distribution assumes a Kroupa IMF (Kroupa 2001). For the model we compare to, the SFR law has been updated to match the empirical SFR laws found in nearby spirals (Muñoz-Mateos et al. 2011). Primordial gas infall decreases exponentially with time, with larger gas infall timescales at greater radii. Gas accretes for a shorter amount of time in the center than at the edge of the disk. Since this model does not include radial mixing of gas through gas inflows and outflows, it should only be considered as a model of the "inside-out" disk formation scenario.

Figure 17 compares the Boissier model at different ages to the radial Z_{gas} profiles of our VENGA subsample of z $\sim$ 0 barred isolated spirals, the gravitationally lensed galaxy Sp1149 at z $\sim$ 1.5 (age $\sim$ 3 Gyr) (Yuan et al. 2011), and the "clone arc" at $z \sim 2$ (Jones et al. 2010). We use models with a circular velocity of 200 km s^{-1} and dimensionless spin parameters of 0.03, 0.05, & 0.07. *The Boissier models exhibit a somewhat shallower Z_{gas} gradient at $z \sim 1.5$ than Sp1149. They subsequently flatten with time from $z \sim 1.5$ to 0, but do not flatten enough to match the shallow Z_{gas} gradients at $z \sim 0$ of the spirals in our VENGA subsample.* This is perhaps not surprising since the Boissier models are missing important aspects of galaxy evolution and baryonic physics. They do not include the radial mixing of gas through gas inflows and outflows, driven by bars and mergers. Furthermore, since they are not cosmological hydrodynamic simulations, they do not include galaxy mergers, cold mode gas accretion, and feedback.

Next we look at more realistic simulations of the assembly and chemical evolution of galaxies, which are cosmologically-motivated, include more baryonic physics and allow for radial inflow/outflow of gas. We compare our VENGA subsample, Sp1149 at z $\sim$ 1.5 (Yuan et al. 2011), and the "clone arc" at $z \sim 2$ (Jones et al. 2010) to two simulated disk galaxies g1536 & g15784.

The first set of models from Pilkington et al. (2012), called MUGS, uses the gravitational N-body and SPH code Gasoline (Wadsley et al. 2004) to simulate 16 isolated disk galaxies that are randomly drawn from a 50 h^{-1} Mpc ΛCDM code with WMAP3 cosmology. Each galaxy is re-simulated at much higher resolution (Klypin et al. 2001). Pilkington et al. (2012) selects four galaxies with the most prominent disks, including g1536 and g15784. The MUGS model includes star formation and SNe feedback (Stinson et al. 2006), heating by a background UV field, cooling in gas derived using CLOUDY (Ferland et al. 1998), and gas enrichment via Type II & Ia SNe assuming a Kroupa IMF.

A similar Gasoline code called MaGICC (Brook et al. 2012), is used to also simulate g1536 and g15784 (Gibson et al. 2013) using "enhanced" feedback with double the energy of MUGS for SNe heating the ISM. MaGICC also includes radiative energy feedback from massive stars, and a Chabrier (2001) IMF.

Both simulated disk galaxies (g1536 & g15784) are selected to be isolated and have somewhat quiescent assembly histories (Gibson et al. 2013) which are identical in both MUGS and MaGICC. It is clear from Figure 18, that the primary difference in Z_{gas} gradients for these simulations depends on the type of feedback being used, and less on which specific disk galaxy (g1536 or g15784) is being simulated. MaGICC, with its "enhanced" feedback, drives stronger radial mixing and more numerous outflows, resulting in higher Z_{gas} than MUGS and flatter gradients at high redshift that steepen only slightly from redshift 1.5 $\rightarrow$ 0 (Gibson et al. 2013), showing little evolution in the gradients over cosmic time. The galaxies in the MUGS simulation have more "conventional" feedback and their Z_{gas} gradients start out strongly negative and flatten significantly between redshift 1.5 $\rightarrow$ 0 (Pilkington et al. 2012). The simulations MUGS and MaGICC imply that the strength of the feedback can significantly affect Z_{gas} gradients (Gibson et al. 2013). Figure 18 shows how the Z_{gas} gradients for g1536 & g15784 for both MUGS and MaGICC evolve from redshift 1.5 $\rightarrow$ 0 and compares them to the high redshift galaxies Sp1149 (Yuan et al. 2011) and the "clone arc" (Jones et al. 2010) and our low redshift VENGA subsample. The MUGS results are in much better agreement with the evolution from high to low redshift in both the absolute value and gradients of Z_{gas}, with what we see when comparing the flat gradients in our VENGA subsample to the strongly negative gradients seen at high redshift in Sp1149 ($z \sim 1.5$, Yuan et al. 2011) and the "clone arc" ($z \sim 2$, Jones et al. 2010), as shown in Figure 18 and discussed in § 5.5. Although these comparisons between simulations and data are very preliminary, "conventional" feedback appears to better match the physics driving the observed evolution of Z_{gas} gradients in spiral galaxies. Our VENGA subsample, along with future observations and modeling, will help constrain the physics behind Z_{gas} gradient evolution.

6 SUMMARY AND CONCLUSIONS

This study explores the gas-phase metallicity Z_{gas}, SFRs, and ionization parameter q in nine nearby (median distance =14.3 Mpc) spiral galaxies drawn from the VIRUS-P Exploration of Nearby Galaxies (VENGA) integral field unit (IFU) spectroscopic survey. Our IFU data has broad blue-to-red wavelength coverage (3600-6800 Å) and moderate spectral resolution ($\sim$ 5 Å FWHM at 5000 Å, corresponding to $\sim$ 120 km s^{-1}). Our sample galaxies were selected to have IFU data over a large fraction of the galaxy's disk (median $f_{R25} \sim 0.66$) while maintaining a high spatial sampling and resolution (median PSF$_{\mathrm{FWHM}}$ $\sim$ 298 pc and median ratio of (R_e-bulge/PSF$_{\mathrm{FWHM}}$)$\sim$ 3.63), so that we can resolve individual galactic components such as the bulge (classical or pseudo), bar, and outer disk, and thereby explore how Z_{gas} varies across these different components. The sample contains nine isolated galaxies, of which six are barred and three are unbarred, as well as one unbarred interacting galaxy. Most galaxies have good coverage with ancillary data including HST, Spitzer, GALEX, CO maps from BIMA SONG (Helfer et al. 2003) and the CARMA CO survey STING (Rahman et al. 2011), and archival HI 21 cm maps from THINGS (Walter et al. 2008) and ALFALFA (Giovanelli et al. 2005).

Our high spatial resolution and large λ coverage allow us to carefully tackle numerous issues that often plague Z_{gas} studies: (a) When calculating the ionization parameter q and Z_{gas}, we use BPT diagrams to exclude gas, which is predominantly excited by an AGN or shocks, rather than predominantly photoionized by photons from massive stars (§ 4.1). The inclusion of this gas can lead to erroneous Z_{gas} values. (b) We assess the impact of DIG and find that fibers dominated by the DIG lie in the outer regions of the disk of our galaxies away from the spiral arms and regions of SF. We find that the location of the DIG at least partially explains the LINER like line ratios on the BPT diagrams seen in the outer regions of the galaxies away from massive SF. We exclude DIG-dominated fibers from calculations of q and Z_{gas} (§ 4.2). (c) We break the degeneracies that exist between some indicators (e.g., R_{23}) and Z_{gas} by using four Z_{gas} indicators (R23, N2O2, O2N2, N2; Table 5). (d) We explicitly calculate Z_{gas} using seven commonly used Z_{gas} diagnostics (Table 5), and explore how the absolute values of Z_{gas} and the shape of the radial profile of Z_{gas} vary between these seven Z_{gas} diagnostics. We calculate q and explore its possible effect on Z_{gas} diagnostics. (e) When interpreting BPT, q, and Z_{gas} maps, our high spatial resolution allow us to explore connections with different galactic components (bulge, bar, spiral arms, outer disk), regions of different excitation (e.g, regions of different SFR density; outflows driven by starburst and AGN; shocks along the bar), and regions of different dynamics (e.g., the circumnuclear inner 1-2 kiloparsec region hosting the rising part of the rotation curve and inner Lindblad resonances of bars; the outer disk hosting the CR and OLR of bars, etc.).

We analyzed seven out of the nine galaxies in our subsample and calculate their Z_{gas} using seven commonly used Z_{gas} diagnostics: R_{23}-KK04, R_{23}-M91, R_{23}-Z94, N2O2-KD02, O3N2-PP04, N2-D02, and N2-PP04 (Table 5). Our results are:

(1) **Resolved Distribution of Z_{gas}, q, DIG, and SFR:** We present high-quality maps (Figure 8) of q, DIG, extinction-corrected Hα-based SFRs, and six different Z_{gas} diagnostics for four isolated barred sample galaxies (NGC 0337, 2903, 4254, & 5713), two isolated unbarred galaxies (NGC 0628 & 3938), and one unbarred isolated galaxy (NGC 5194). We exclude the unbarred galaxy NGC 2775 (as it shows very little ionized gas emission) and NGC 1068 (as the fibers covering this Seyfert galaxy are dominated by LINER and/or Seyfert emission). *The Z_{gas} maps are of higher quality in terms sampling frequency and spatial resolution compared to existing Z_{gas} maps of spiral galaxies in the literature.*

(2) **Comparison between the seven Z_{gas} diagnostics:** In terms of the *shape* of the radial profile of Z_{gas}, the eight Z_{gas} diagnostics show fairly good agreement beyond the inner 1-2 kpc, and yield flat to moderately negative gradients (Figure 10). In terms of the *absolute values* of Z_{gas}, there is fairly good agreement, within 0.1 to 0.2 dex, between R_{23}-KK04, R_{23}-M91, R_{23}-Z94, and N2O2-KD02 . Compare to the latter three diagnostics, O3N2-PP04, N2-PP04, and N2-D02 yield Z_{gas} that are systematically lower by 0.1 to 0.4 dex. The N2O2-KD02 & O3N2-PP04 diagnostics show the least amount of scatter out of all seven Z_{gas} diagnostics. We have explored if corrections based on q can resolve some of these differences but have found it does not have a significant effect.

(3) **Z_{gas} in barred galaxies:** Among our four barred galaxies, *the Z_{gas} gradient is flat or at most most moderately negative along the bar and in the outer disk beyond the bar end.* In the inner 1-2 kpc radius, the behavior differs across the four galaxies with Z_{gas} rising toward the center in NGC 2903 and 0337, but staying flat in NGC 4254 and NGC 5713. In units of dex kpc^{-1}, the shallow gradients range from (-0.008 to -0.026) in R_{23}-KK04, (-0.01 to -0.04) in N2O2-KD02 and (-0.04 to 0.004) in N2-PP04, while in units of dex (R/R25)$^{-1}$ they range from (-0.13 to -0.24) in R_{23}-KK04, (-0.17 to -0.23) in N202-KD02, and (-0.3 to 0.04) in N2-PP04 (Table 6). We explore how our findings of shallow Z_{gas} gradients may be tied to the gas flows expected in a barred potential. Gas outflow between the CR and OLR of the bar may in part explain the flat gradient in the outer disk beyond the bar end, while gas inflow between the CR and ILR of the bar may in part explain the flat gradient along the bar. We find that NGC 2903 shows evidence of an ILR, and NGC 0337 might be undergoing a minor merger. We find no evidence of IRLs in NGC 4254 & 5713, although the large distance of NGC 5713 makes it difficult to determine.

(4) **Comparison of Z_{gas} between isolated barred and unbarred galaxies:** We compare our Z_{gas} gradients between barred and unbarred galaxies in our own VENGA sample and to barred and unbarred spiral galaxies in the control sample from Rupke et al. (2010b). We find that the gradients for both barred and unbarred galaxies are flat to slightly negative. There is no noticeable difference between the gradients in units of dex kpc^{-1} between the barred and unbarred spirals. In units of dex (R/R25)$^{-1}$, our isolated unbarred galaxies show a possible slightly steeper gradient than our barred galaxies, but it is difficult to draw conclusions from such a small dataset. The flat gradients seen in our unbarred galaxies likely have had their gradients flattened by previously existing bars, interactions, and major and minor mergers. These results are in disagreement with previous studies which have claimed that unbarred galaxies show steeper gradients (ie. Martin & Roy 1994; Vila-Costas & Edmunds 1992). It is possible that the intrinsic large scatter in gradients and the lower quality data for multi-slit spectroscopy when compared to IFU data might explain this discrepancy.

(5) **Comparison of Z_{gas} between isolated and interacting spirals:** We compare our Z_{gas} gradients between non-interacting and interacting galaxies in our own VENGA sample and to non-interacting and interacting spiral galaxies from Rupke et al. (2010b). It is difficult to draw conclusions for our comparison to the Rupke et al. (2010b) sample, but the one interacting galaxy in our VENGA subsample (NGC 5194) shows the flattest gradient when compared to all the other non-interacting spirals, but it is not significantly flatter and the non-interacting spirals do have quite flat gradients. Future IFU observations will help constrain if there is a difference in the gradients between interacting and isolated spirals.

(6) **Comparison of Z_{gas} between high and low redshift galaxies:** The Z_{gas} gradients in our $z \sim 0$ galaxies are markedly shallower than in higher redshift galaxies, such as Sp1149 at $z \sim 1.5$ (Yuan et al. 2011), and the "clone arc" at $z \sim 2$ (Jones et al. 2010) (Figure 16). This is consistent with the idea that Z_{gas} gradients are flattening over cosmic time due to radial gas mixing induced by bars, interactions, and major and minor mergers.

(7) **Comparison of Z_{gas} radial gradients with theoretical models:** We compare our data and other empirical results on Z_{gas} to theoretical models. The updated Boissier models, as used in Muñoz-Mateos et al. (2011), exhibit a Z_{gas} gradient, which is shallower than observations at z $\sim$ 1.5, and steeper than our spirals at z$\sim$0. This may be due to the fact that these models do not include galaxy mergers, cold mode gas accretion, feedback, and radial mixing of gas through gas inflows and outflows. We also compared to new models by Gibson et al. (2013) and Pilkington et al. (2012). We find that the evolution of Z_{gas} gradients from a redshift of 1.5 $\rightarrow$ 0 are best fit by the models which do not have enhanced feedback from supernovae and gas recycling, and instead include more conventional feedback prescriptions.

(8) **Broader impact of Z_{gas} maps:** The high-quality metallicity maps we produce will be useful for a wide variety of scientific applications such as the [CII] studies by the KINGFISH team (A. Bolatto and D. Fisher, private communication; Kennicutt et al. 2011) and studies of the CO-to-H_2 conversion factor by Sandstrom et al. (2012).

REFERENCES

Adams J.J., Blanc G.A., Hill G.J., et al., Jan. 2011, ApJS, 192, 5

Allen M.G., Groves B.A., Dopita M.A., Sutherland R.S., Kewley L.J., Sep. 2008, ApJS, 178, 20

Alonso-Herrero A., Ryder S.D., Knapen J.H., Apr. 2001, MNRAS, 322, 757

Baldwin J.A., Phillips M.M., Terlevich R., Feb. 1981, PASP, 93, 5

Blanc G.A., Heiderman A., Gebhardt K., Evans N.J. II, Adams J., Oct. 2009, ApJ, 704, 842

Blanc G.A., Gebhardt K., Heiderman A., et al., Oct. 2010, In: L. M. Stanford, J. D. Green, L. Hao, & Y. Mao (ed.) New Horizons in Astronomy: Frank N. Bash Symposium 2009, vol. 432 of Astronomical Society of the Pacific Conference Series, 180

Blanc G.A., Weinzirl T., Song M., et al., May 2013, AJ, 145, 138

Boissier S., Prantzos N., Aug. 1999, MNRAS, 307, 857

Brook C.B., Stinson G., Gibson B.K., Wadsley J., Quinn T., Aug. 2012, MNRAS, 424, 1275

Buta R., Combes F., 1996, FCPH, 17, 95

Cameron E., Carollo C.M., Oesch P., et al., Nov. 2010, MNRAS, 409, 346

Cappellari M., Emsellem E., Feb. 2004, PASP, 116, 138

Chabrier G., Jun. 2001, ApJ, 554, 1274

Chiappini C., Matteucci F., Gratton R., Mar. 1997, ApJ, 477, 765

Cole S., Lacey C.G., Baugh C.M., Frenk C.S., Nov. 2000, MNRAS, 319, 168

Condon J.J., 1992, ARAA, 30, 575

Conselice C.J., Oct. 2009, MNRAS, 399, L16

Cortés J.R., Kenney J.D.P., Hardy E., Aug. 2008, ApJ, 683, 78

de Vaucouleurs G., de Vaucouleurs A., Corwin H.G., et al., Feb. 1995, VizieR Online Data Catalog, 7155, 0

Dekel A., Birnboim Y., May 2006, MNRAS, 368, 2

Dekel A., Birnboim Y., Engel G., et al., Jan. 2009a, Nature, 457, 451

Dekel A., Sari R., Ceverino D., Sep. 2009b, ApJ, 703, 785

Denicoló G., Terlevich R., Terlevich E., Feb. 2002, MNRAS, 330, 69

Devereux N.A., Young J.S., Feb. 1990, ApJL, 350, L25

Dolphin A.E., Kennicutt R.C. Jr., Jan. 2002, AJ, 123, 207

Dong X.Y., De Robertis M.M., Mar. 2006, AJ, 131, 1236

Dopita M.A., Evans I.N., Aug. 1986, ApJ, 307, 431

Dopita M.A., Kewley L.J., Heisler C.A., Sutherland R.S., Oct. 2000, ApJ, 542, 224

Drozdovsky I.O., Karachentsev I.D., Mar. 2000, A&A Suppl., 142, 425

Dutil Y., Roy J.R., May 1999, ApJ, 516, 62

Edmunds M.G., Pagel B.E.J., Dec. 1984, MNRAS, 211, 507

Ellison S.L., Nair P., Patton D.R., et al., Sep. 2011, MNRAS, 416, 2182

Farage C.L., McGregor P.J., Dopita M.A., Bicknell G.V., Nov. 2010, ApJ, 724, 267

Ferland G.J., Korista K.T., Verner D.A., et al., Jul. 1998, PASP, 110, 761

Fioc M., Rocca-Volmerange B., Oct. 1997, A&A, 326, 950

Fisher D.B., Drory N., Aug. 2008, AJ, 136, 773

Freedman W.L., Madore B.F., Gibson B.K., et al., May 2001, ApJ, 553, 47

Gibson B.K., Pilkington K., Brook C.B., Stinson G.S., Bailin J., Apr. 2013, ArXiv e-prints

Giovanelli R., Haynes M.P., Kent B.R., et al., Dec. 2005, AJ, 130, 2598

Greenawalt B., Walterbos R.A.M., Braun R., Jul. 1997, ApJ, 483, 666

Haffner L.M., Dettmar R.J., Beckman J.E., et al., Jul 2009, Rev. Mod. Phys., 81, 969, URL `http://link.aps.org/doi/10.1103/RevModPhys.81.969`

Handa T., Sofue Y., Nakai N., 1991, In: Combes F., Casoli F. (eds.) Dynamics of Galaxies and Their Molecular Cloud Distributions, vol. 146 of IAU Symposium, 156

Helfer T.T., Thornley M.D., Regan M.W., et al., Apr. 2003, ApJS, 145, 259

Heller C.H., Shlosman I., Athanassoula E., Dec. 2007, ApJ, 671, 226

Helou G., Khan I.R., Malek L., Boehmer L., Oct. 1988, ApJS, 68, 151

Hernquist L., Mihos J.C., Jul. 1995, ApJ, 448, 41

Hill G.J., MacQueen P.J., Smith M.P., et al., Aug. 2008, In: Society of Photo-Optical Instrumentation Engineers (SPIE) Conference Series, vol. 7014 of Society of Photo-Optical Instrumentation Engineers (SPIE) Conference Series

Hoopes C.G., Walterbos R.A.M., Apr. 2003, ApJ, 586, 902

Jacobs B.A., Rizzi L., Tully R.B., et al., Aug. 2009, AJ, 138, 332

Jogee S., 2006, In: Alloin D. (ed.) Physics of Active Galactic Nuclei at all Scales, vol. 693 of Lecture Notes in Physics, Berlin Springer Verlag, 143

Jogee S., Kenney J.D.P., Smith B.J., 1999, In: Barnes J.E., Sanders D.B. (eds.) Galaxy Interactions at Low and High Redshift, vol. 186 of IAU Symposium, 357

Jogee S., Barazza F.D., Rix H.W., et al., Nov. 2004, ApJL, 615, L105

Jogee S., Scoville N., Kenney J.D.P., Sep. 2005, ApJ, 630, 837

Jogee S., Miller S.H., Penner K., et al., Jun. 2009, ApJ, 697, 1971

Jones T., Ellis R., Jullo E., Richard J., Dec. 2010, ApJL, 725, L176
Karachentsev I.D., Makarov D.I., Sharina M.E., et al., Feb. 2003, A&A, 398, 479
Kauffmann G., Heckman T.M., Tremonti C., et al., Dec. 2003a, MNRAS, 346, 1055
Kauffmann G., Heckman T.M., White S.D.M., et al., May 2003b, MNRAS, 341, 33
Kennicutt R.C., Calzetti D., Aniano G., et al., Dec. 2011, PASP, 123, 1347
Kennicutt R.C. Jr., Sep. 1983, ApJ, 272, 54
Kennicutt R.C. Jr., 1998, ARAA, 36, 189
Kereš D., Katz N., Weinberg D.H., Davé R., Oct. 2005, MNRAS, 363, 2
Kereš D., Katz N., Fardal M., Davé R., Weinberg D.H., May 2009, MNRAS, 395, 160
Kewley L.J., Dopita M.A., Sep. 2002, ApJS, 142, 35
Kewley L.J., Ellison S.L., Jul. 2008, ApJ, 681, 1183
Kewley L.J., Dopita M.A., Sutherland R.S., Heisler C.A., Trevena J., Jul. 2001, ApJ, 556, 121
Kewley L.J., Geller M.J., Barton E.J., Apr. 2006a, AJ, 131, 2004
Kewley L.J., Groves B., Kauffmann G., Heckman T., Nov. 2006b, MNRAS, 372, 961
Klypin A., Kravtsov A.V., Bullock J.S., Primack J.R., Jun. 2001, ApJ, 554, 903
Kobulnicky H.A., Kewley L.J., Dec. 2004, ApJ, 617, 240
Kobulnicky H.A., Kennicutt R.C. Jr., Pizagno J.L., Apr. 1999, ApJ, 514, 544
Kormendy J., Kennicutt R.C. Jr., Sep. 2004, ARAA, 42, 603
Kowalski M., Rubin D., Aldering G., et al., Oct. 2008, ApJ, 686, 749
Kroupa P., Apr. 2001, MNRAS, 322, 231
Laine S., Kenney J.D.P., Yun M.S., Gottesman S.T., Feb. 1999, ApJ, 511, 709
Leitherer C., Schaerer D., Goldader J.D., et al., Jul. 1999, ApJS, 123, 3
Leroy A.K., Walter F., Bigiel F., et al., Jun. 2009, AJ, 137, 4670
Lotz J.M., Jonsson P., Cox T.J., et al., Dec. 2011, ApJ, 742, 103
Macri L.M., Stetson P.B., Bothun G.D., et al., Sep. 2001, ApJ, 559, 243
Madsen G.J., Reynolds R.J., Haffner L.M., Nov. 2006, ApJ, 652, 401
Magrini L., Corbelli E., Galli D., Aug. 2007, A&A, 470, 843
Marinova I., Jogee S., Apr. 2007, ApJ, 659, 1176
Martin C.L., May 2000, In: Arthur S.J., Brickhouse N.S., Franco J. (eds.) Revista Mexicana de Astronomia y Astrofisica Conference Series, vol. 9 of Revista Mexicana de Astronomia y Astrofisica, vol. 27, 270–272
Martin P., Roy J.R., Apr. 1994, ApJ, 424, 599
Mathis J.S., Nov. 2000, ApJ, 544, 347
McCall M.L., Rybski P.M., Shields G.A., Jan. 1985, ApJS, 57, 1
McGaugh S.S., Oct. 1991, ApJ, 380, 140
Mentuch Cooper E., Wilson C.D., Foyle K., et al., Aug. 2012, ApJ, 755, 165
Mihos J.C., Hernquist L., Jun. 1996, ApJ, 464, 641
Mo H.J., Mao S., White S.D.M., Apr. 1998, MNRAS, 295, 319
Moustakas J., Kennicutt R.C. Jr., Tremonti C.A., et al., Oct. 2010, ApJS, 190, 233
Muñoz-Mateos J.C., Boissier S., Gil de Paz A., et al., Apr. 2011, ApJ, 731, 10
Oh K., Sarzi M., Schawinski K., Yi S.K., Aug. 2011, ApJS, 195, 13
Olivares E. F., Hamuy M., Pignata G., et al., Jun. 2010, ApJ, 715, 833
Osterbrock D.E., Ferland G.J., 2006, Astrophysics of gaseous nebulae and active galactic nuclei
Pettini M., Pagel B.E.J., Mar. 2004, MNRAS, 348, L59
Pilkington K., Few C.G., Gibson B.K., et al., Apr. 2012, A&A, 540, A56
Poznanski D., Butler N., Filippenko A.V., et al., Apr. 2009, ApJ, 694, 1067
Prantzos N., Boissier S., Apr. 2000, MNRAS, 313, 338
Rahman N., Bolatto A.D., Wong T., et al., Apr. 2011, ApJ, 730, 72
Rich J.A., Dopita M.A., Kewley L.J., Rupke D.S.N., Sep. 2010, ApJ, 721, 505
Romano-Díaz E., Shlosman I., Heller C., Hoffman Y., Nov. 2008, ApJL, 687, L13
Rosales-Ortega F.F., Kennicutt R.C., Sanchez S.F., et al., 02 2010, URL `http://arxiv.org/abs/1002.1946v1`
Rupke D.S.N., Kewley L.J., Barnes J.E., Feb. 2010a, ApJL, 710, L156
Rupke D.S.N., Kewley L.J., Chien L.H., Nov. 2010b, ApJ, 723, 1255
Saha A., Thim F., Tammann G.A., Reindl B., Sandage A., Jul. 2006, ApJS, 165, 108
Sakai S., Ferrarese L., Kennicutt R.C. Jr., Saha A., Jun. 2004, ApJ, 608, 42
Sánchez S.F., Kennicutt R.C., Gil de Paz A., et al., Nov. 2011, In: Zapatero Osorio M.R., Gorgas J., Maíz Apellániz J., Pardo J.R., Gil de Paz A. (eds.) Highlights of Spanish Astrophysics VI, 339–344
Sánchez S.F., Rosales-Ortega F.F., Marino R.A., et al., Oct. 2012, A&A, 546, A2
Sánchez-Blázquez P., Peletier R.F., Jiménez-Vicente J., et al., Sep. 2006, MNRAS, 371, 703
Sandage A., Bedke J., 1994, The Carnegie Atlas of Galaxies. Volumes I, II.
Sandstrom K.M., Leroy A.K., Walter F., et al., Dec. 2012, ArXiv e-prints
Sarzi M., Falcón-Barroso J., Davies R.L., et al., Mar. 2006, MNRAS, 366, 1151
Schlegel D.J., Finkbeiner D.P., Davis M., Jun. 1998, ApJ, 500, 525
Shaver P.A., McGee R.X., Newton L.M., Danks A.C., Pottasch S.R., Jul. 1983, MNRAS, 204, 53
Sheth K., Elmegreen D.M., Elmegreen B.G., et al., Mar. 2008, ApJ, 675, 1141
Shields G.A., 1990, ARAA, 28, 525
Somerville R.S., Primack J.R., Dec. 1999, MNRAS, 310, 1087
Spitzer L., 1978, Physical processes in the interstellar medium
Springob C.M., Masters K.L., Haynes M.P., Giovanelli R., Marinoni C., Oct. 2007, ApJS, 172, 599

Stinson G., Seth A., Katz N., et al., Dec. 2006, MNRAS, 373, 1074
Sutherland R.S., Dopita M.A., Sep. 1993, ApJS, 88, 253
Swinbank A.M., Sobral D., Smail I., et al., Oct. 2012, MNRAS, 426, 935
Tubbs A.D., Apr. 1982, ApJ, 255, 458
Tully R.B., 1988, Nearby galaxies catalog
Tully R.B., Shaya E.J., Karachentsev I.D., et al., Mar. 2008, ApJ, 676, 184
Tully R.B., Rizzi L., Shaya E.J., et al., Aug. 2009, AJ, 138, 323
van Dokkum P.G., Whitaker K.E., Brammer G., et al., Feb. 2010, ApJ, 709, 1018
Vila-Costas M.B., Edmunds M.G., Nov. 1992, MNRAS, 259, 121
Wadsley J.W., Stadel J., Quinn T., Feb. 2004, NewA, 9, 137
Walsh W., Beck R., Thuma G., et al., Jun. 2002, A&A, 388, 7
Walter F., Brinks E., de Blok W.J.G., et al., Dec. 2008, AJ, 136, 2563
Walterbos R.A.M., Apr. 1998, PASA, 15, 99
Weinzirl T., Jogee S., Khochfar S., Burkert A., Kormendy J., May 2009, ApJ, 696, 411
Weinzirl T., Jogee S., Conselice C.J., et al., Dec. 2011, ApJ, 743, 87
Wood K., Hill A.S., Joung M.R., et al., Oct. 2010, ApJ, 721, 1397
Xu C., Dec. 1990, ApJL, 365, L47
Yuan T.T., Kewley L.J., Swinbank A.M., Richard J., Livermore R.C., May 2011, ApJL, 732, L14
Yuan T.T., Kewley L.J., Swinbank A.M., Richard J., Nov. 2012, ApJ, 759, 66
Zaritsky D., Kennicutt R.C. Jr., Huchra J.P., Jan. 1994, ApJ, 420, 87

Table 1. Comparison between different IFU surveys

IFU Survey	Spectral Range (Å)	Spectral (km s^{-1})	Spatial Res. Res.	FOV	# E/S0s mapped	# Spirals mapped	Redshift Range
VENGA	**3600-6800**	120	4.3" **(VENGA med.=298 pc)**[a] **(Subsample med.=298 pc)**[b]	**110" x 110'**	0	**30**	**z < 0.010** **(VENGA med. D=14.3 Mpc)**[a] **(Subsample med. D=14.3 Mpc)**[b]
PINGS	3700-7100	600	2.7"	$74'' \times 65''$	3	14	z < 0.005 (med. D=17.5 Mpc)
CALIFA	3745-700	350 (red), 180 (blue)	3.7" **(med.=1256 pc)**	$74'' \times 65''$	~ 200	~ 400	0.005 < z < 0.03 **(med. D $\approx$ 70 Mpc)** **(cutoff 45"<D25<80")**
SAURON (Low-res.) (Hi-res.)	4760-5400	105 90	0.94" 0.27'	$33'' \times 41''$ $9'' \times 11''$	48	24	z < 0.012
Atlas^{3D}	4760-5400	105	0.94"	$33'' \times 41''$	260	0	z < 0.010

[a] Median for full VENGA survey of 30 nearby spiral galaxies.
[b] Median for our subsample of nine nearby spiral galaxies.

Table 2: Our subsample of nine VENGA Galaxies.

NGC	Dist. (Mpc)	R25 (')	i (°)	Hubble Type	Bar?[a]	Interacting?	Bulge B/T	Bulge Re (Kpc)	Bulge n	Res. (pc)	Re/PSF	f_{R25}
0337[b]	19.3	1.44× 0.91	55	SB(s)d	y	n				402		0.72
0628	9.9	5.24× 4.78	27	SA(s)c	n	n	0.10	0.60	1.35	206	2.89	0.47
1068[b]	10.1	3.54× 3.01	35	SA(rs)b	y	n				210		0.72
2775	18.2	2.13× 1.66	43	SA(r)ab	n	n	0.61	4.18	4.85	379	11.01	1.18
2903	8.9	6.29× 3.01	66	SAB(rs)bc	y	n	0.09	0.36	0.42	185	1.93	0.38
3938	17.9	2.69× 2.45	27	SA(s)c	n	n	0.07	0.56	1.18	373	1.50	0.60
4254	14.3	2.69× 2.34	33	SA(s)c	y	n	0.39	2.11	2.68	298	7.08	0.81
5194[b]	8.4	5.61× 3.46	56	SA(s)bc	n	y				175		0.56
5713	32.6	1.38× 1.23	30	SAB(rs)bc	y	n	0.33	2.46	1.84	679	3.63	0.66

[a] Barredness determined from literature, including IR imaging, kinematics, and distribution of cold gas. We performed independant checks on bar properties by inspection of IR images, and using the works of Weinzirl et al. (2009) and Marinova & Jogee (2007).
[b] Galaxies with no bulge parameters have not undergone bulge-disk 2D image decomposition.

Table 3: Full VENGA Sample of 30 Nearby Spiral Galaxies

(1) NGC	(2) Hubble Type[a]	(3) B/T[b]	(4) Bulge n[b]	(5) R_e[b] (",Kpc)	(6) R_e/PSF[c]	(7) Dist.[d] (Mpc)	(8) Res. (pc)	(9) R25[a] (')	(10) R_{vp} (')	(11) f_{R25}	(12) i[e] (°)	(13) HI[f]	(14) CO[g]	(15) GA[h]	(16) Sp[h]	(17) 2M[h]	(18) VW[h]	(19) XCo[i]	(20) KF[j]
0337	**SB(s)d**			**,**		**19.3^{α}**	**402**	**1.44× 0.91**	**1.04**	**0.72**	**55**	**y$^{\alpha}$**	**y$^{\beta\gamma}$**	**y**	**y**	**y**	**n**	**1**	**y**
0628	**SA(s)c**	**0.10^{α}**	**1.35^{α}**	**12.43, 0.60^{α}**	**2.89**	**9.9^{β}**	**206**	**5.24× 4.78**	**2.46**	**0.47**	**27**	**y$^{\beta}$**	**y$^{\alpha\gamma}$**	**y**	**y**	**y**	**n**	**0**	**y**
1042	SAB(rs)cd	0.03^{β}	0.10^{β}	5.91, 0.12^{β}	1.37	4.2^{γ}	87	2.34× 1.82	1.54	0.66	43	y$^{\alpha}$	n	y	y	y	y	0	n
1068	**SA(rs)b**			**,**		**10.1^{γ}**	**210**	**3.54× 3.01**	**2.55**	**0.72**	**35**	**n**	**y$^{\alpha}$**	**y**	**y**	**y**	**n**	**0**	**n**
2775	**SA(r)ab**	**0.61^{β}**	**4.85^{β}**	**47.35, 4.18^{β}**	**11.01**	**18.2^{δ}**	**379**	**2.13× 1.66**	**2.52**	**1.18**	**43**	**n**	**n**	**y**	**y**	**y**	**y**	**0**	**n**
2841	SA(r)b	0.17^{γ}	2.97^{γ}	11.19, 0.76^{γ}	2.60	14.1^{ϵ}	293	4.06× 1.77	2.76	0.68	69	y$^{\alpha\beta}$	y$^{\alpha\gamma}$	y	y	y	y	2	y
2903	**SAB(rs)bc**	**0.09^{γ}**	**0.42^{γ}**	**8.29, 0.36^{γ}**	**1.93**	**8.9^{ζ}**	**185**	**6.29× 3.01**	**2.39**	**0.38**	**66**	**y$^{\alpha\beta}$**	**y$^{\alpha\gamma}$**	**y**	**y**	**y**	**y**	**0**	**n**
3147	SA(rs)bc	0.25^{α}	3.66^{α}	5.82, 1.15^{α}	1.35	40.9^{η}	852	1.95× 1.73	1.61	0.83	30	y$^{\alpha}$	y$^{\beta}$	y	y	y	n	0	n
3166	SAB(rs)0	0.25^{β}	0.56^{β}	3.25, 0.37^{β}	0.76	23.6^{δ}	491	2.39× 1.17	1.79	0.75	65	n	n	y	y	y	n	0	n
3198	SB(rs)c	0.11^{α}	5.12^{α}	14.17, 1.00^{α}	3.30	14.5^{θ}	302	4.26× 1.66	1.15	0.27	73	y$^{\alpha\beta}$	y$^{\beta\gamma}$	y	y	y	n	0	y
3227	SAB(s)pec	0.10^{β}	0.32^{β}	4.84, 0.52^{β}	1.13	22.1^{δ}	460	2.69× 1.82	1.69	0.63	51	n	n	n	y	y	y	0	n
3351	SB(r)b	0.17^{γ}	1.51^{γ}	11.00, 0.51^{γ}	2.56	9.6^{ι}	200	3.71× 2.51	1.70	0.46	51	y$^{\alpha\beta}$	y$^{\alpha\gamma}$	y	y	y	n	0	y
3521	SAB(rs)bc	0.10^{γ}	3.20^{γ}	3.83, 0.21^{γ}	0.89	11.2^{γ}	233	5.48× 2.56	2.69	0.49	67	y$^{\alpha\beta}$	y$^{\alpha\gamma}$	y	y	y	y	2	y
3627	SAB(s)b	0.08^{γ}	2.90^{γ}	21.57, 1.06^{γ}	5.02	10.1^{κ}	210	4.56× 2.08	2.69	0.59	68	y$^{\alpha\beta}$	y$^{\alpha}$	y	y	y	n	1	y
3938	**SA(s)c**	**0.07^{β}**	**1.18^{β}**	**6.43, 0.56^{β}**	**1.50**	**17.9^{λ}**	**373**	**2.69× 2.45**	**1.61**	**0.60**	**27**	**n**	**y$^{\alpha\gamma}$**	**y**	**y**	**y**	**n**	**1**	**y**
3949	SA(s)bc	0.08^{β}	0.64^{β}	4.67, 0.43^{β}	1.09	19.1^{γ}	398	1.44× 0.83	0.98	0.68	59	y$^{\alpha}$	y$^{\beta}$	y	y	y	y	0	n
4013	SAb			,		18.9^{γ}	394	2.62× 0.51	1.71	0.65	90	y$^{\alpha}$	n	y	n	y	n	0	n
4254	**SA(s)c**	**0.39^{β}**	**2.68^{β}**	**30.46, 2.11^{β}**	**7.08**	**14.3^{α}**	**298**	**2.69× 2.34**	**2.17**	**0.81**	**33**	**y$^{\alpha}$**	**y$^{\beta\gamma}$**	**y**	**y**	**y**	**n**	**0**	**y**
4314	SB(rs)a	0.26^{β}	2.05^{β}	11.22, 0.57^{β}	2.61	10.4^{δ}	216	2.08× 1.86	1.60	0.77	30	y$^{\alpha}$	n	y	y	y	y	0	n
4450	SA(s)ab	0.17^{β}	2.26^{β}	8.19, 0.61^{β}	1.90	15.3^{γ}	318	2.62× 1.95	1.68	0.64	46	n	y$^{\alpha}$	y	y	y	n	0	n
4569	SAB(rs)ab	0.06^{γ}	1.90^{γ}	1.64, 0.08^{γ}	0.38	9.9^{μ}	206	4.78× 2.18	0.96	0.20	68	n	y$^{\alpha\gamma}$	y	y	y	n	1	y
4826	SA(rs)ab	0.13^{γ}	3.94^{γ}	16.71, 0.38^{γ}	3.89	4.7^{ν}	97	5.00× 2.69	0.90	0.18	62	y$^{\alpha\beta}$	y$^{\alpha}$	y	y	y	n	0	y
5055	SA(rs)bc	0.26^{γ}	1.84^{γ}	46.91, 2.05^{γ}	10.91	9.0^{ξ}	187	6.29× 3.62	0.94	0.15	59	y$^{\alpha\beta}$	y$^{\alpha\gamma}$	y	y	y	n	2	y
5194	**SA(s)bc**			**,**		**8.4^{λ}**	**175**	**5.61× 3.46**	**3.14**	**0.56**	**56**	**y$^{\beta}$**	**y$^{\alpha\gamma}$**	**y**	**y**	**y**	**n**	**0**	**n**
5713	**SAB(rs)bc**	**0.33^{β}**	**1.84^{β}**	**15.59, 2.46^{β}**	**3.63**	**32.6^{δ}**	**679**	**1.38× 1.23**	**0.91**	**0.66**	**30**	**n**	**y$^{\beta\gamma}$**	**y**	**y**	**y**	**n**	**1**	**y**
5981	Sc			,		49.7^{γ}	1036	1.41× 0.23	1.30	0.92	90	y$^{\alpha}$	n	y	y	y	n	0	n
6503	SA(s)cd			,		5.3^{o}	110	3.54× 1.20	1.98	0.56	76	n	y$^{\beta}$	y	y	y	n	0	n
6946	SAB(rs)cd	0.01^{γ}	1.87^{γ}	4.41, 0.10^{γ}	1.03	4.7^{λ}	97	5.74× 4.89	1.78	0.31	35	y$^{\beta}$	y$^{\delta}$	y	n	y	n	2	y
7479	SB(s)c	0.09^{β}	1.09^{β}	6.00, 0.88^{β}	1.40	30.2^{γ}	629	2.04× 1.55	1.77	0.87	44	y$^{\alpha}$	y$^{\epsilon}$	y	y	y	n	0	n
7331	SA(s)b			,		14.5^{π}	302	5.24× 1.86	0.89	0.17	75	y$^{\alpha\beta}$	y$^{\gamma}$	y	y	y	n	2	y

Our subsample of nine VENGA galaxies in our study are in highlighted in boldface.

(a) Hubble Type visual classification and R25 from RC3 de Vaucouleurs et al. (1995)

(b) Bulge-to-total (B/T) mass ratio, bulge Sersic Index (Bulge n), and bulge scale radius (R_e) from decomposition in:
(α) K-band, Dong & De Robertis 2006 (β) H-band, Weinzirl et al. 2009 (γ) V-band, Fisher & Drory 2008

(c) Ratio of the bulge scale length R_e to the point spread function of VIRUS-P (R_e/4.3 arcsec.)

(d) Distance to galaxy in Mpc from (α) Springob et al. 2007 (β) Olivares E. et al. 2010 (γ) Tully et al. 2008 (δ) Tully 1988, corrected H_0 from 75 → 70 km/s/Mpc (ϵ) Macri et al. 2001
(ζ) Drozdovsky & Karachentsev 2000 (η) Kowalski et al. 2008 (θ) Saha et al. 2006 (ι) Sakai et al. 2004 (κ) Dolphin & Kennicutt 2002 (λ) Poznanski et al. 2009 (μ) Cortés et al. 2008
(ν) Jacobs et al. 2009 (ξ) Tully et al. 2009 (o) Karachentsev et al. 2003 (π) Freedman et al. 2001

(e) Inclination $= \cos^{-1}\left(\sqrt{\left[(\text{R25 major axis/R25 minor axis})^2 - 0.2^2\right] / \left[1 - 0.2^2\right]}\right) + 3^{\circ}$, from Tully (1988)

(f) HI 22 cm maps from (α) ALFALFA, Giovanelli et al. 2005 (β) THINGS, Walter et al. 2008

(g) CO maps from (α) BIMA-SONG, Helfer et al. 2003, (β) STINGS, Bolatto et al. 2011, in preparation (γ) HERACLES, Leroy et al. 2009 (δ) Walsh et al. 2002 (ϵ) Laine et al. 1999

(h) Coverage by GA=GALEX, Sp=Spitzer, 2M=2MASS, VW=VIRUS-W

(i) Status of galaxy in the XCo survey: (0) not in study (1) in study but no metallicity (2) in study but uncertain metallicity from Moustakas et al. 2010

(j) Galaxy coverage in KINGFISH survey (Kennicutt et al. 2011)

Table 4. Star Formation Rates

Galaxy	Global SFR[a]	VENGA Hα SFR[b]	VENGA Peak $\Sigma_{\mathbf{SFR}}$[c]	FIR Lum.[d]	FIR SFR[e]
NGC 0337	4.26	1.81	0.498	6.42E+09	2.50
NGC 0628	2.00	0.62	2.201	4.60E+09	1.79
NGC 2903	3.63	1.81	0.323	5.87E+09	2.29
NGC 3938	1.20	1.91	1.768	6.47E+09	2.53
NGC 4254	10.96	5.42	3.397	1.47E+10	5.72
NGC 5194	7.59	3.23	1.148	1.48E+10	5.79
NGC 5713	9.77	12.21	8.633	3.74E+10	14.60

[a] Global UV or Hα SFRs ($M_\odot$ yr^{-1}) from Blanc et al. (2013) and references therein.
[b] Hα based SFRs ($M_\odot$ yr^{-1}) measured from integrated Hα flux over the regions covered by our pointings of VIRUS-P (as seen in Figure 1). See § 4.3 for details.
[c] Largest SFR surface density Σ_{SFR} ($M_\odot$ yr^{-1} kpc^{-2}) seen in VENGA spatial coverage of galaxy. See also Figure 9 for Σ_{SFR} radial gradients.
[d] FIR luminosity, in units of solar luminosity, calculated from the IRAS 60 & 100 μm bands.
[e] FIR SFR ($M_\odot$ yr^{-1}) calculated from the FIR luminosity. See § 4.3 for details.

Table 5. Summary of the seven Z_{gas} diagnostics

Z_{gas} **Diagnostics**	**Line Ratio**[a]	**Reference**	**Type of Calibration**	q**-Corrected?**[a]
R_{23}-M91	([OII]+[OIII])/Hβ	McGaugh (1991)	Theoretical	y[b]
R_{23}-KK04	([OII]+[OIII])/Hβ	Kobulnicky & Kewley (2004)	Theoretical	y[c]
R_{23}-Z94	([OII]+[OIII])/Hβ	Zaritsky et al. (1994)	Theoretical	n
N2O2-KD02	[NII]/[OII]	Kewley & Dopita (2002)	Theoretical	Invariant[d]
O3N2-PP04	([OIII]/Hβ)/([NII]/Hα)	Pettini & Pagel (2004)	Empirical	n
N2-D02	[NII]/Hα	Denicoló et al. (2002)	Empirical	n
N2-PP04	[NII]/Hα	Pettini & Pagel (2004)	Empirical	n

[a] Details for each of the Z_{gas} diagnostics can be found in § 4.5, and in Kewley & Ellison (2008).
[b] q corrected for using the [OIII]/[OII] line ratio. See Appendix B.
[c] q and Z_{gas} solved for iteratively as seen in Appendix A.
[d] [NII]/[OII] invariant to the value of q as seen in Figure 7.

.

Table 6. Z_{gas} radial gradient results

Name	**Hubble Type**	Z_{gas} **gradients**[a] R_{23}**-KK04** [dex kpc^{-1}]	R_{23}**-KK04** [dex (R/R25)$^{-1}$]	**N2O2-KD02** [dex kpc^{-1}]	**N2O2-KD02** [dex (R/R25)$^{-1}$]	**N2-PP04** [dex kpc^{-1}]	**N2-PP04** [dex (R/R25)$^{-1}$]
NGC 0337	Sd	-0.023 ± 0.003	-0.19 ± 0.02	-0.034 ± 0.002	-0.27 ± 0.02	-0.034 ± 0.001	-0.27 ± 0.01
NGC 0628	Sc	-0.0201 ± 0.0007	-0.30 ± 0.01	-0.0268 ± 0.0004	-0.404 ± 0.006	-0.0093 ± 0.0007	-0.14 ± 0.01
NGC 2903	Sbc	-0.0103 ± 0.0009	-0.17 ± 0.01	-0.0200 ± 0.0004	-0.327 ± 0.007	0.0008 ± 0.0008	0.01± 0.01
NGC 3938	Sc	-0.0225 ± 0.0007	-0.32 ± 0.01	-0.0200 ± 0.0005	-0.280 ± 0.007	-0.0002 ± 0.0004	-0.003 ± 0.006
NGC 4254	Sc	-0.0275 ± 0.0005	-0.222 ± 0.004	-0.0224 ± 0.0003	-0.181± 0.002	0.0040 ± 0.0004	0.032 ±0 .003
NGC 5194	Sbc	-0.0005 ± 0.0004	-0.007 ± -0.005	-0.0036 ± 0.0002	-0.049 ± 0.003	0.0101 ± 0.0004	0.138 ± 0.005
NGC 5713	Sbc	-0.014 ± 0.004	-0.18 ± 0.05	-0.013 ± 0.002	-0.17 ± 0.03	-0.008 ± 0.002	-0.10 ± 0.03

[a] Error bars are 1σ errors on the slope computed from a linear least squares fit to the data.

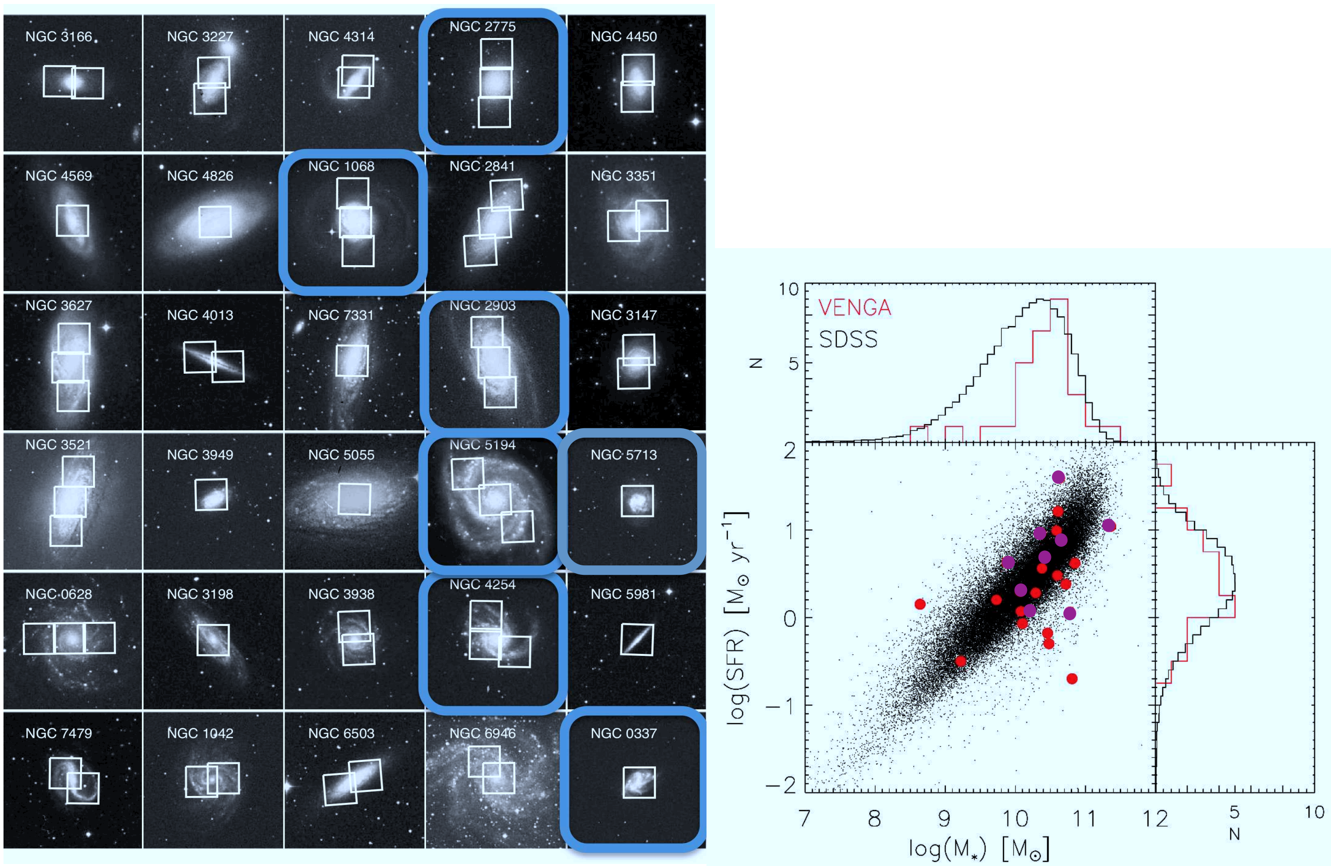

Figure 1. Left: DSS images of the VENGA sample of 30 nearby spiral galaxies are overlaid with squares, which indicate the pointings and coverage of the VIRUS-P IFU. Purple highlights our subsample of 9/30 spirals which are selected to maximize both our spatial resolution and spatial coverage of the disk for studying Z_{gas}. **Right:** Scatter plot and histograms adapted from Blanc et al. (2013) showing the stellar mass ($M_{\star}$) and SFR for the VENGA galaxies (red circles), compared to a sample of SDSS galaxies from the MPA/JHU catalog (black dots; Kauffmann et al. 2003b). For stellar mass above 10^{10} $M_{\odot}$, the VENGA spirals span a representative range of the stellar mass-SFR plane. Our subsample of nine spirals are highlighted in purple.

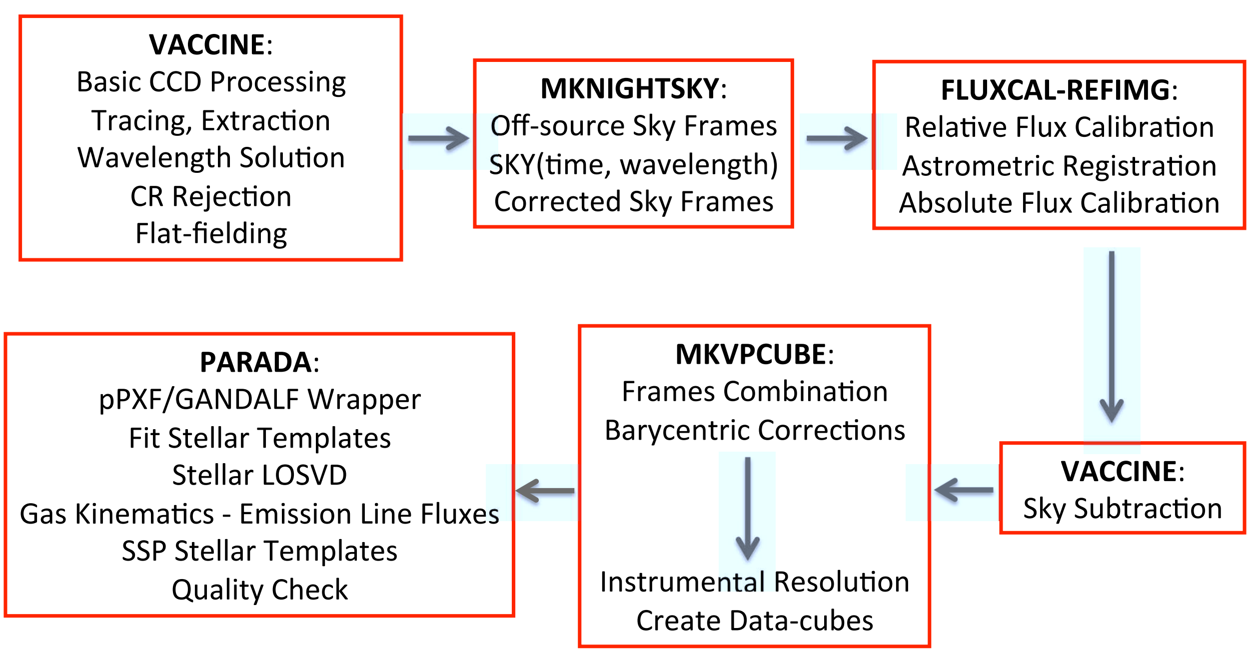

Figure 2. Flow chart of our data reduction and analysis pipeline, as outlined in § 3.

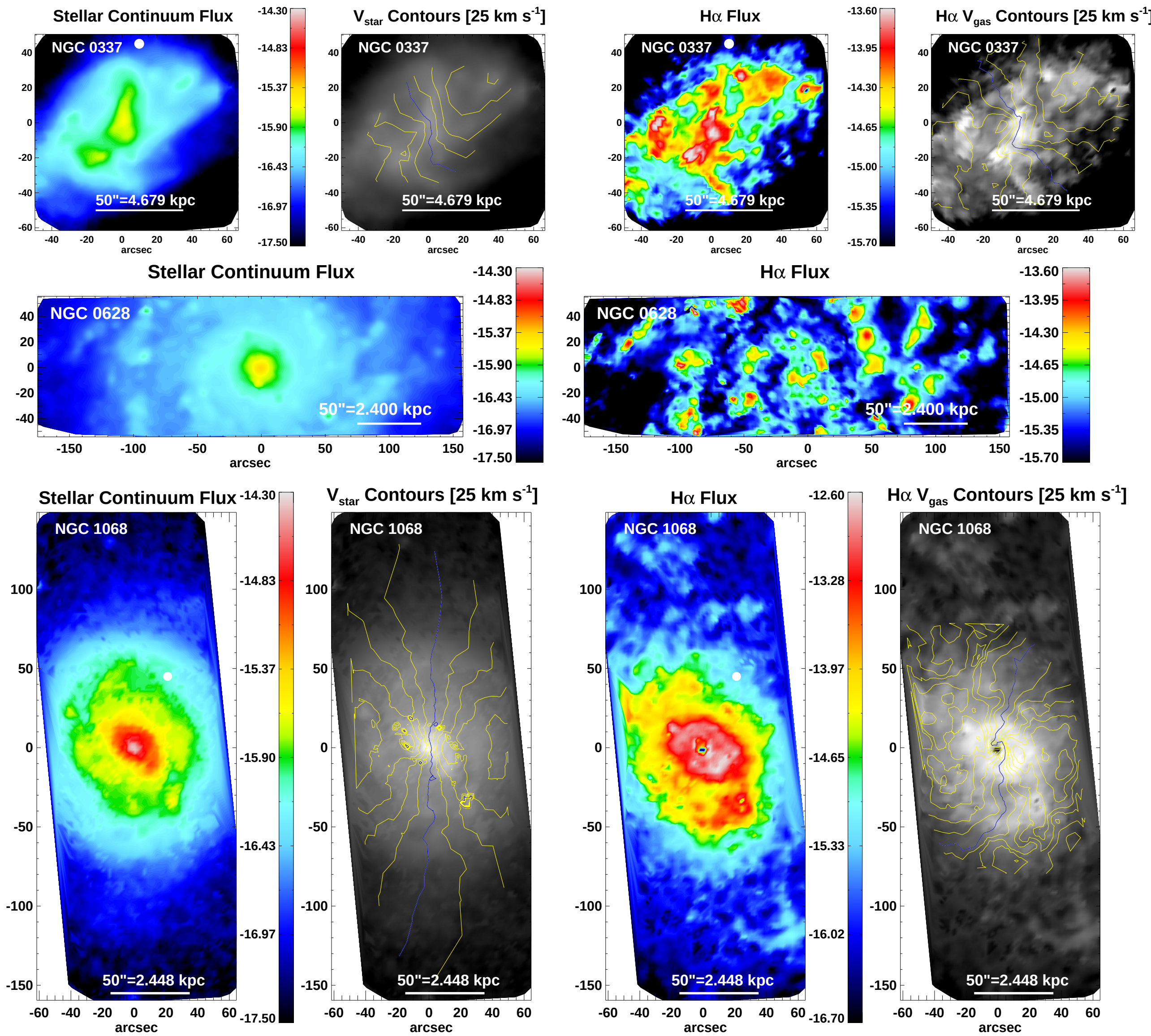

Figure 3. From top to bottom, each row shows VENGA IFU-based data products for the nine galaxies in our subsample: NGC 0337, 0628, 1068, 2775, 2903, 3938, 4354, 5194, & 5713. From left to right, each row shows the optical stellar continuum, stellar velocity field, extinction corrected Hα map, and Hα velocity field. The yellow isovelocity contours are in increments of 25 km s^{-1}, with the blue contour showing the systemic velocity where $v_{sys} = 0$ km s^{-1}. For the isolvelocity contours, we use Voronoi binning for regions with low S/N, with a minimum of S/N $\geqslant 3$ for Hα and a minimum S/N $\geqslant 50$ for the stellar continuum.

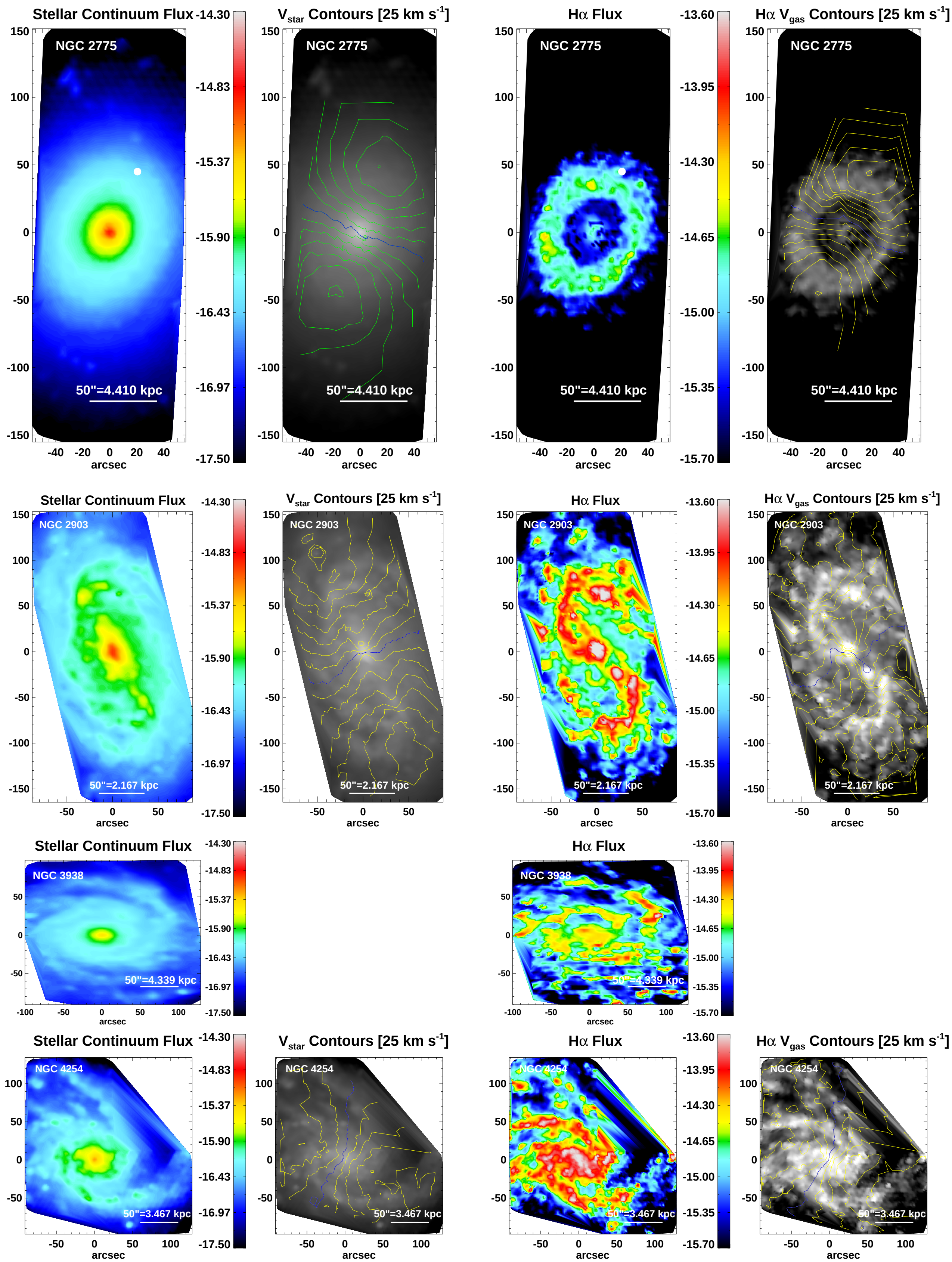

Figure 3. Continued for... NGC 2775, 2903, 3938, & 4254.

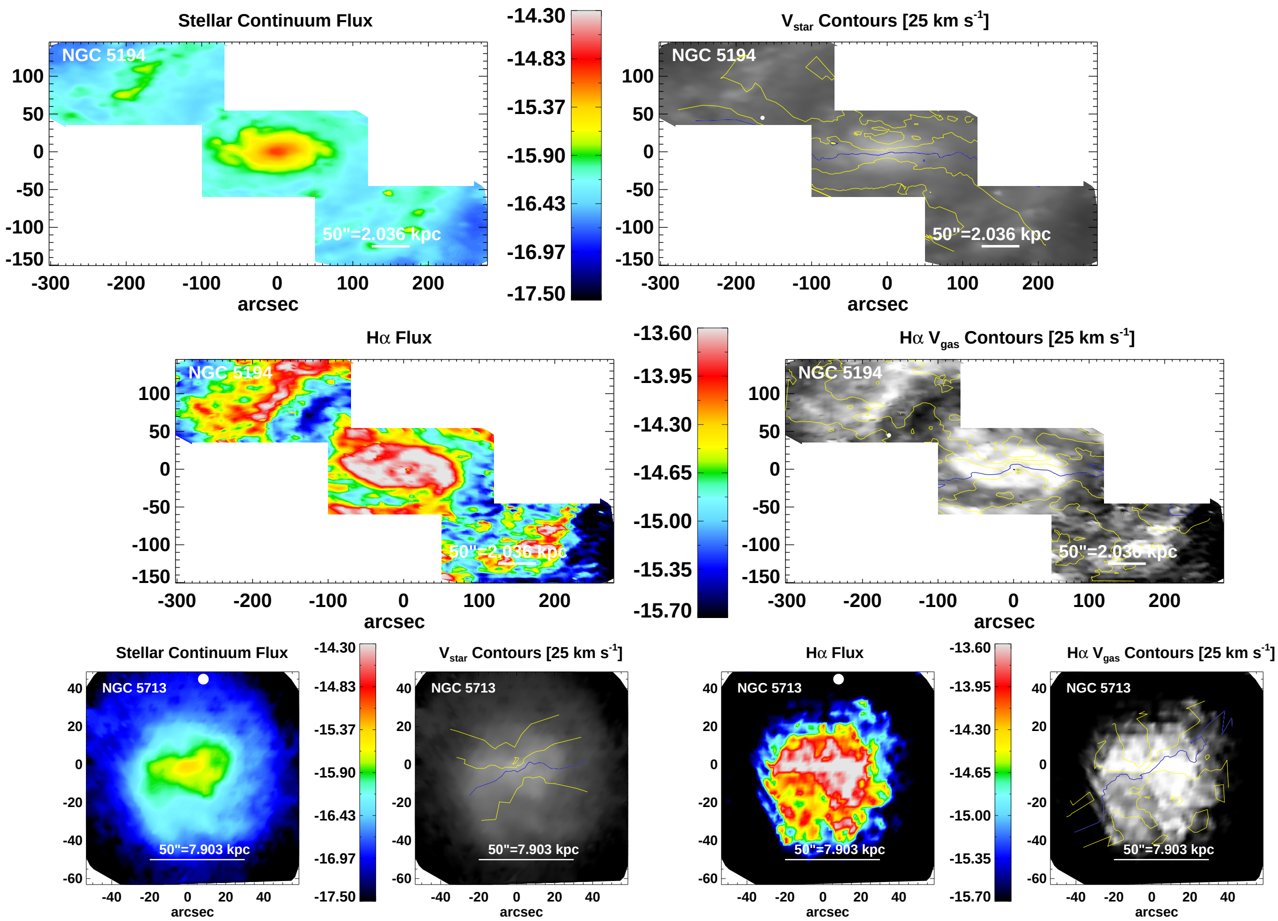

Figure 3. Continued for... 5194 & 5713.

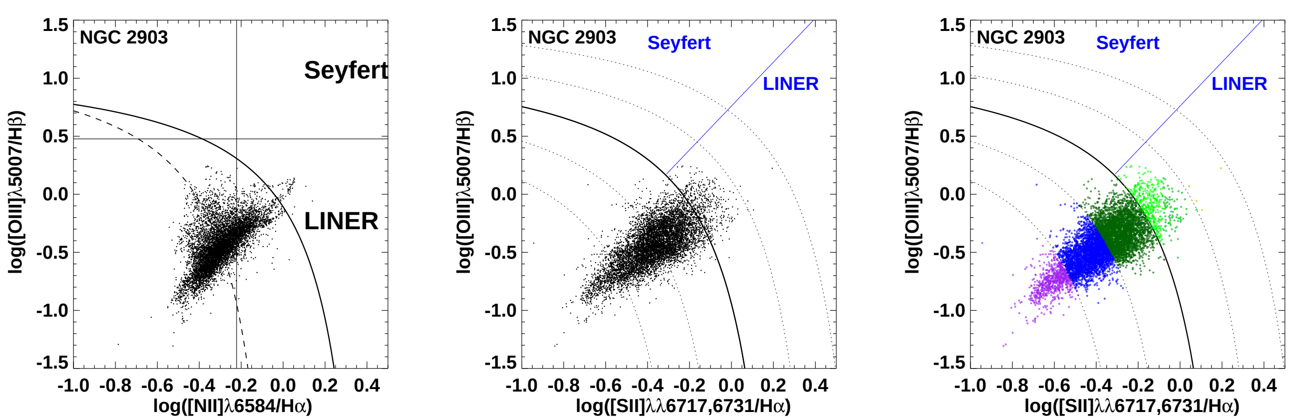

Figure 4. Example BPT diagrams for NGC 2903. Fibers covering regions dominated by recent massive SF are separated from those covering shocked or AGN excited gas by the threshold given in Kewley et al. (2001), shown as the solid black curve. **Left:** The [NII]/Hα BPT diagram is shown and the Seyfert & LINER regions are separated by the straight black lines shown in Kauffmann et al. (2003a) where . The dashed black curve is an additional threshold given in Kauffmann et al. (2003a) for separating regions dominated by recent massive SF from those covering shocked or AGN excited gas. **Center:** The [SII]/Hα BPT diagram is shown and the Seyfert & LINER regions are separated using the prescription given by Kewley et al. (2006b) shown in blue. **Right:** We show a *sliced* [SII]/Hα BPT diagram where we color code fibers based on where they fall in their *excitation sequence* of excitation by scaling the SF vs. excited threshold as seen as the dotted curves. The *excitation sequence* quantifies the distance a fiber is from the SF threshold defined by Kewley et al. (2001).

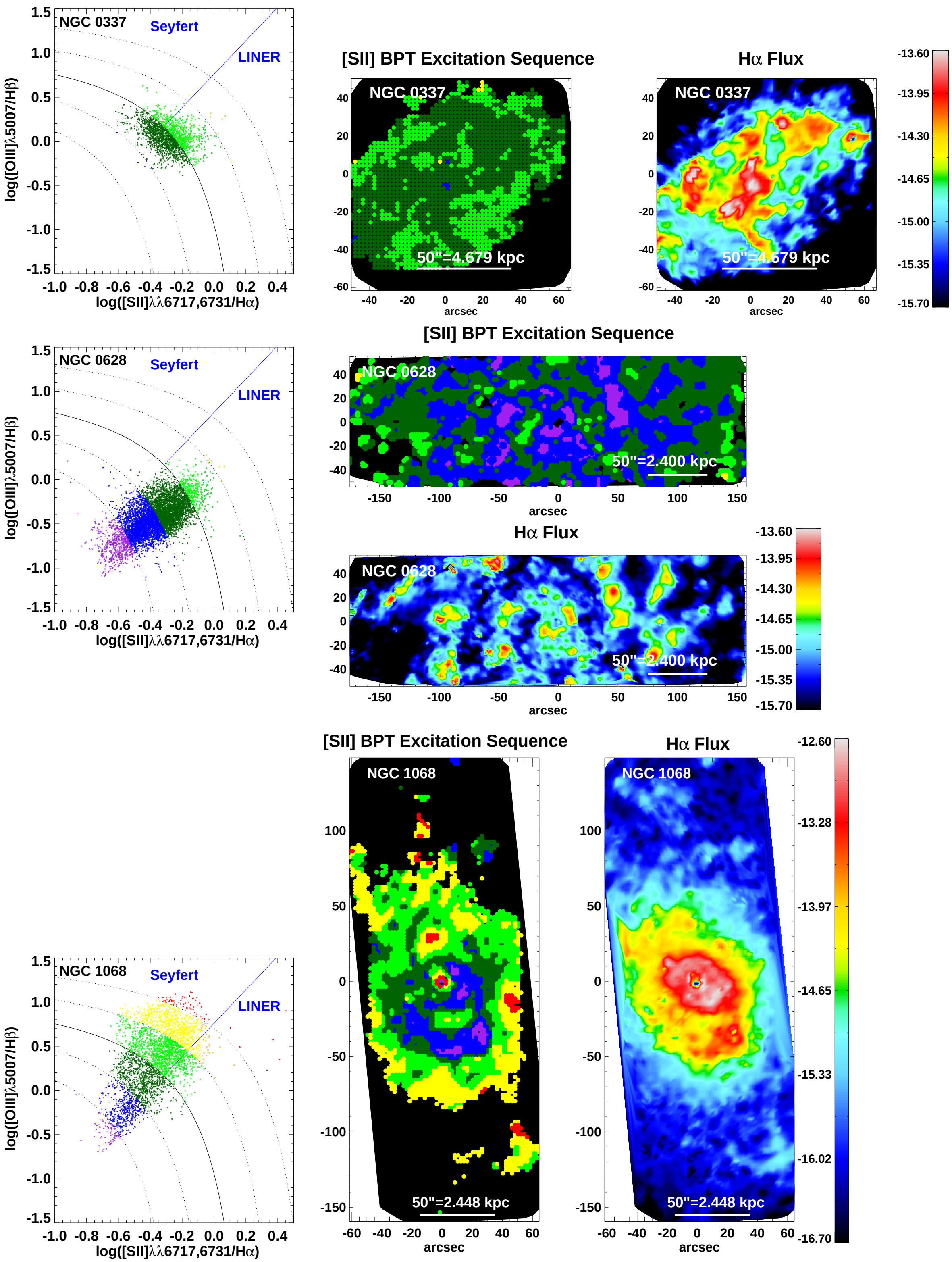

Figure 5. BPT diagrams and mapping of excited regions for NGC 0337, 0628, & 1068 from top-to-bottom. **Left:** *Sliced* [SII] BPT diagram color coded by *excitation sequence*. **Center:** Color coded BPT excitation sequence mapped back onto the galaxy. **Right:** Hα flux.

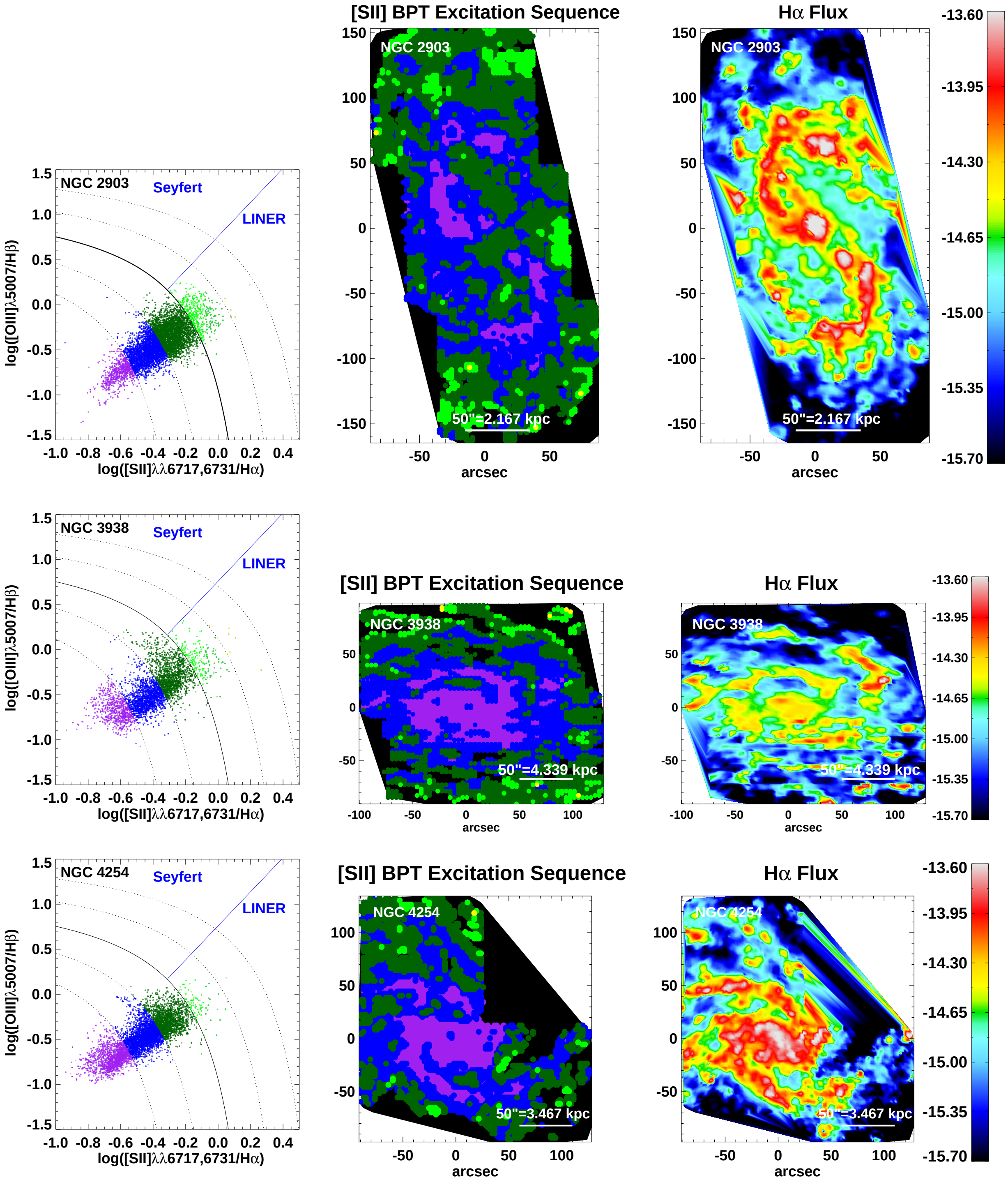

Figure 5. Continued... for NGC 2903, 3938, & 4254

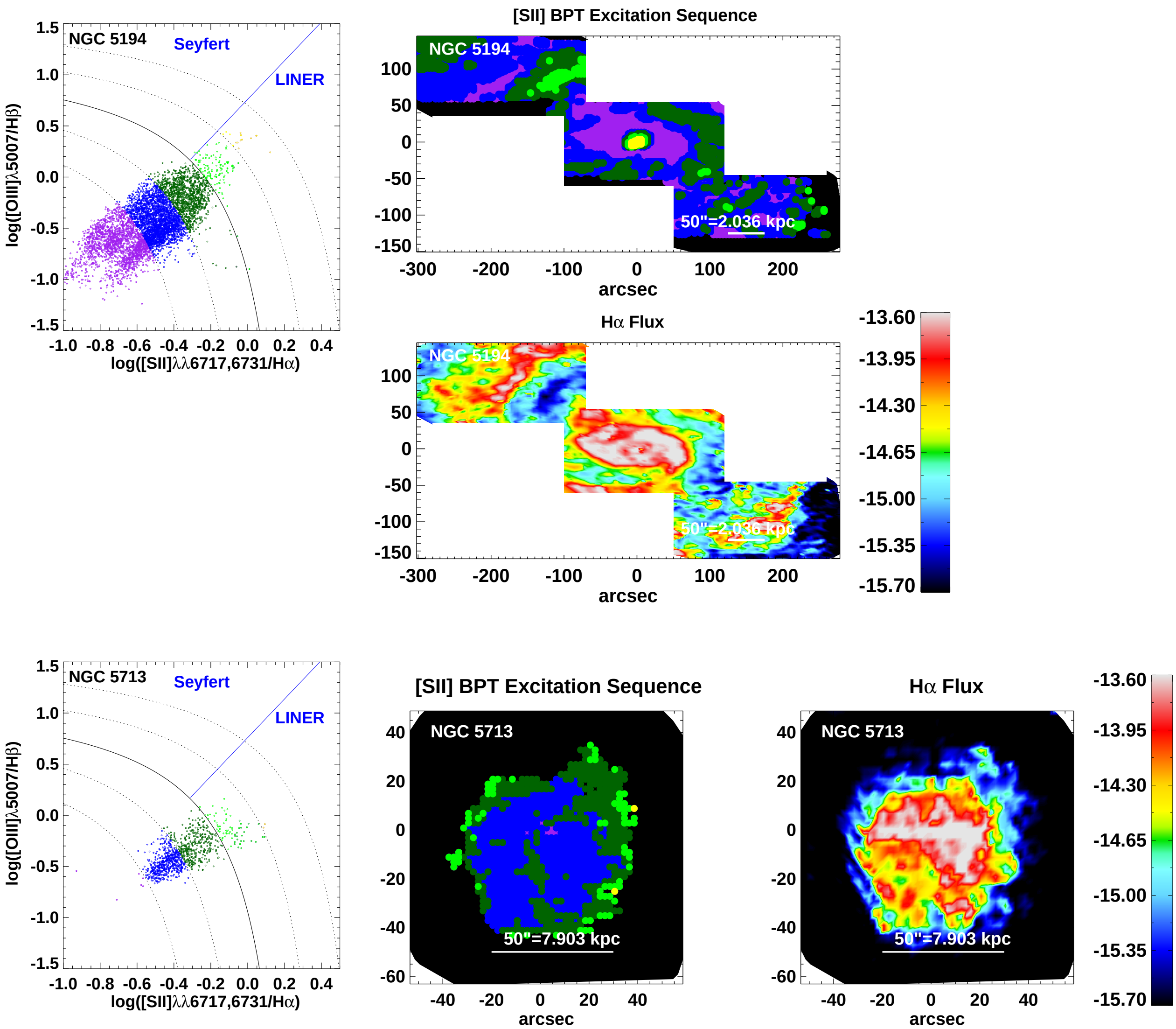

Figure 5. Continued... for NGC 5194 & 5713.

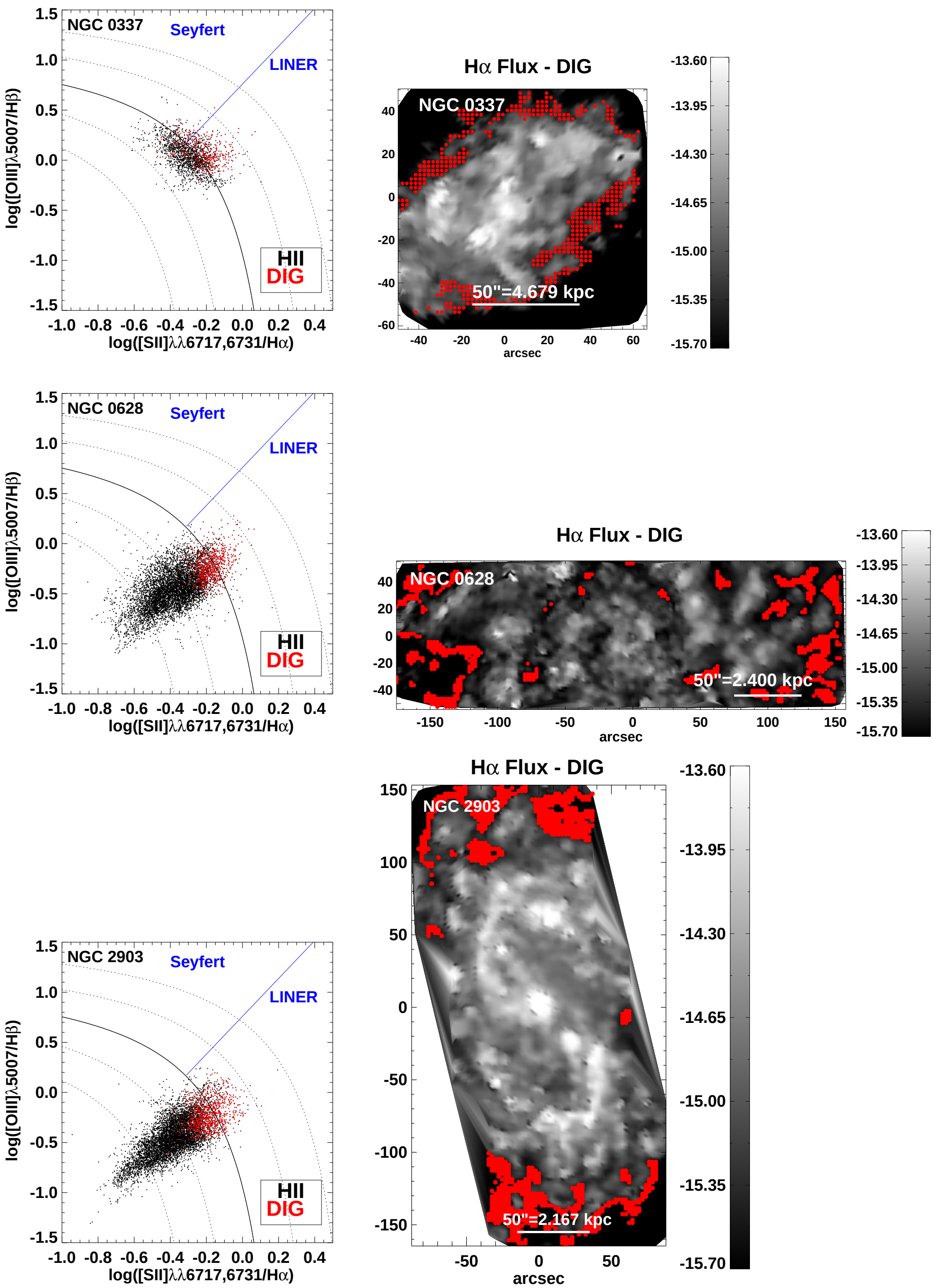

Figure 6. Left: [SII] BPT diagrams where fibers dominated by 100% DIG are shown in red. **Right:** Hα flux map showing the location of the DIG-dominated fibers. DIG-dominated fibers tend to fall on the upper right portion of the [SII] BPT diagram due to the high [SII]/Hα ratio found in DIG dominated emission, and they mostly are found on the edges outer disk of the galaxies, away from the spiral arms and regions of high SFR. Galaxies from top to bottom: NGC 0337, 0628, & 2903.

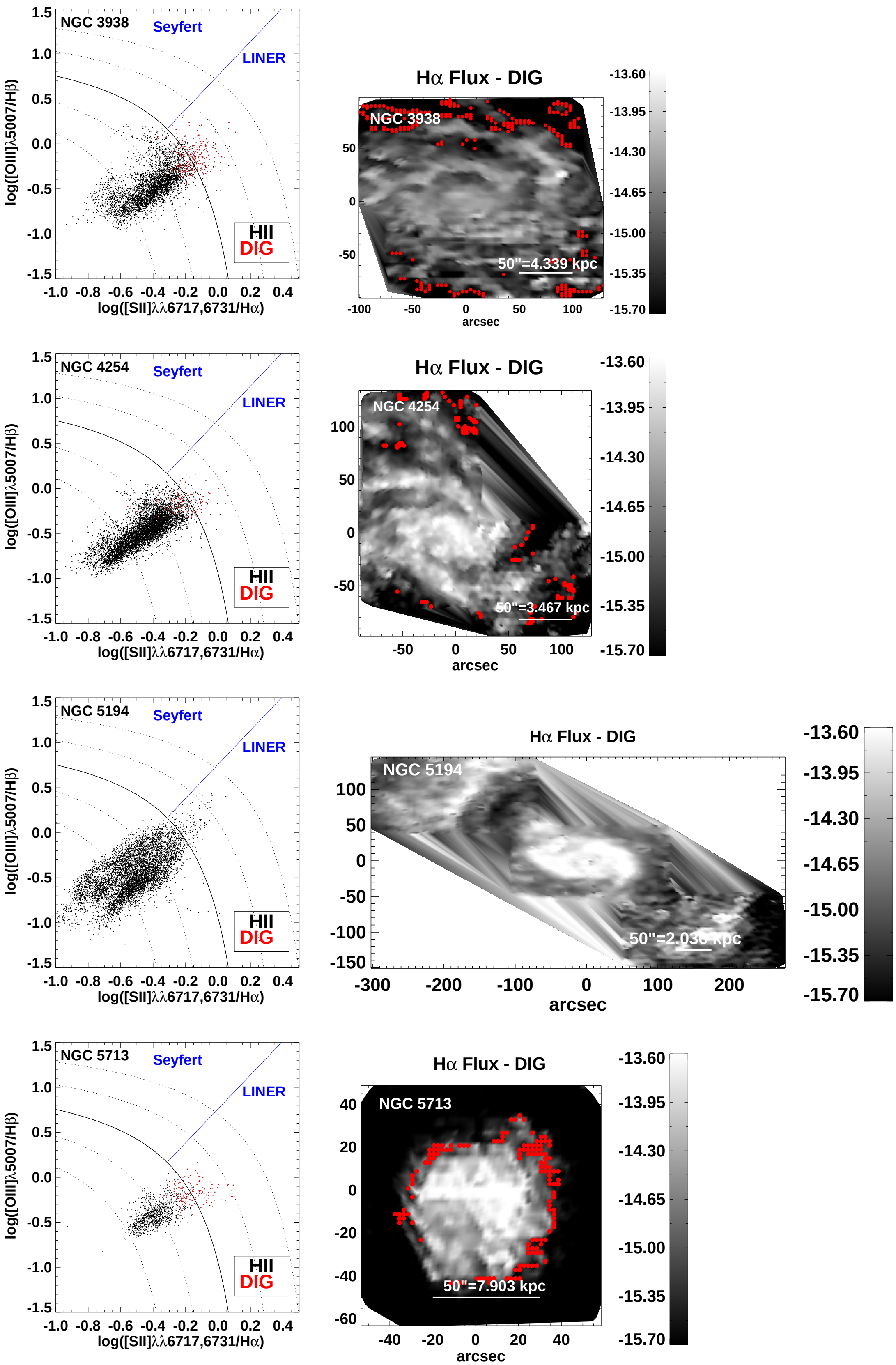

Figure 6. Continued for... NGC 3938, 4254, 5194, & 5713.

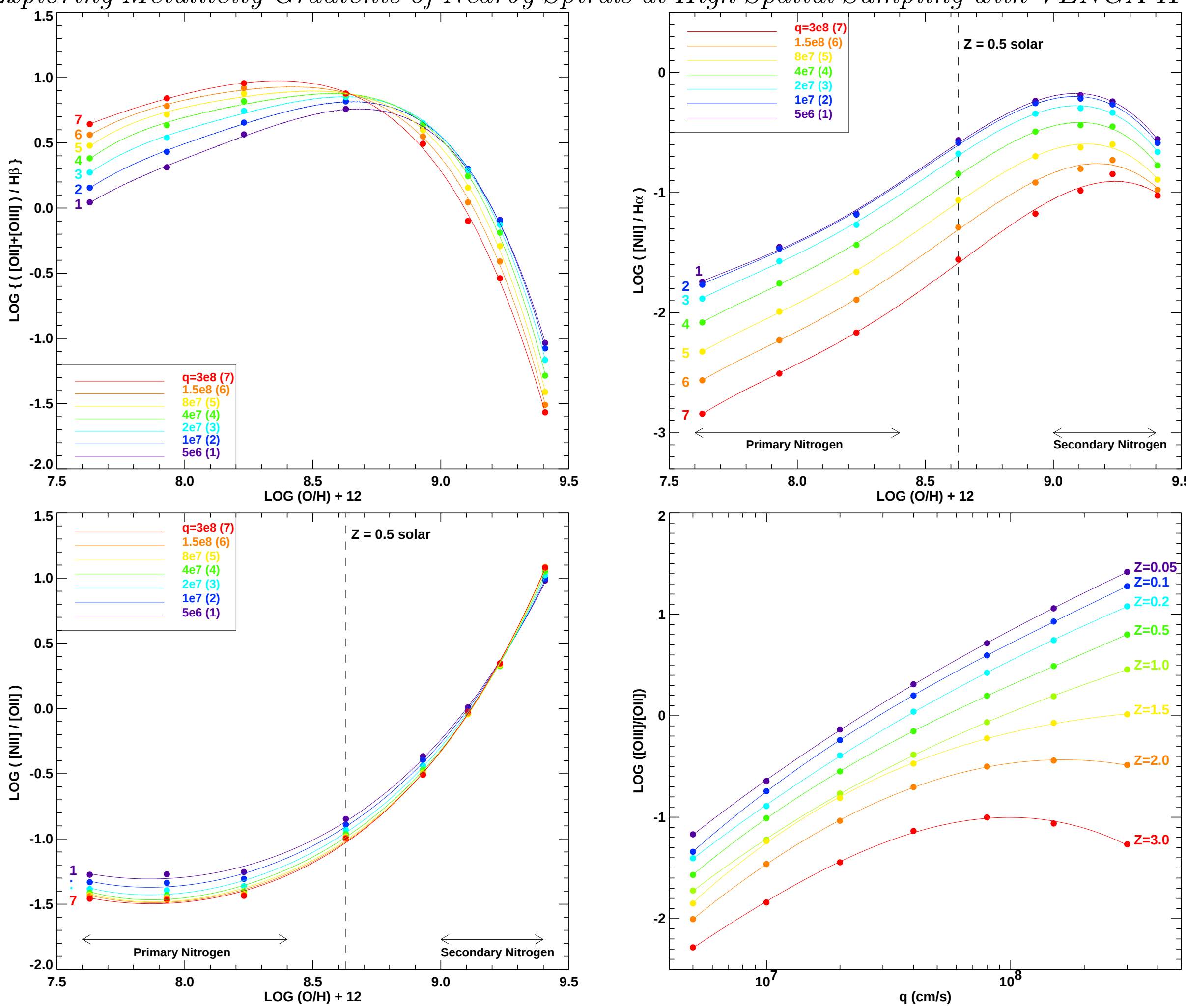

Figure 7. Plots from Kewley & Dopita (2002) showing the theoretical dependence of the emission line ratios. **Top Left:** R_{23} = ([OII]+[OIII])/Hβ, **Top Right:** [NII]/Hα, **Bottom Left:** [NII]/[OII], and **Bottom Right:** [OIII]/[OII] on Z_{gas} and ionization parameter q for gas in regions primarily photoionized by photons from massive stars.

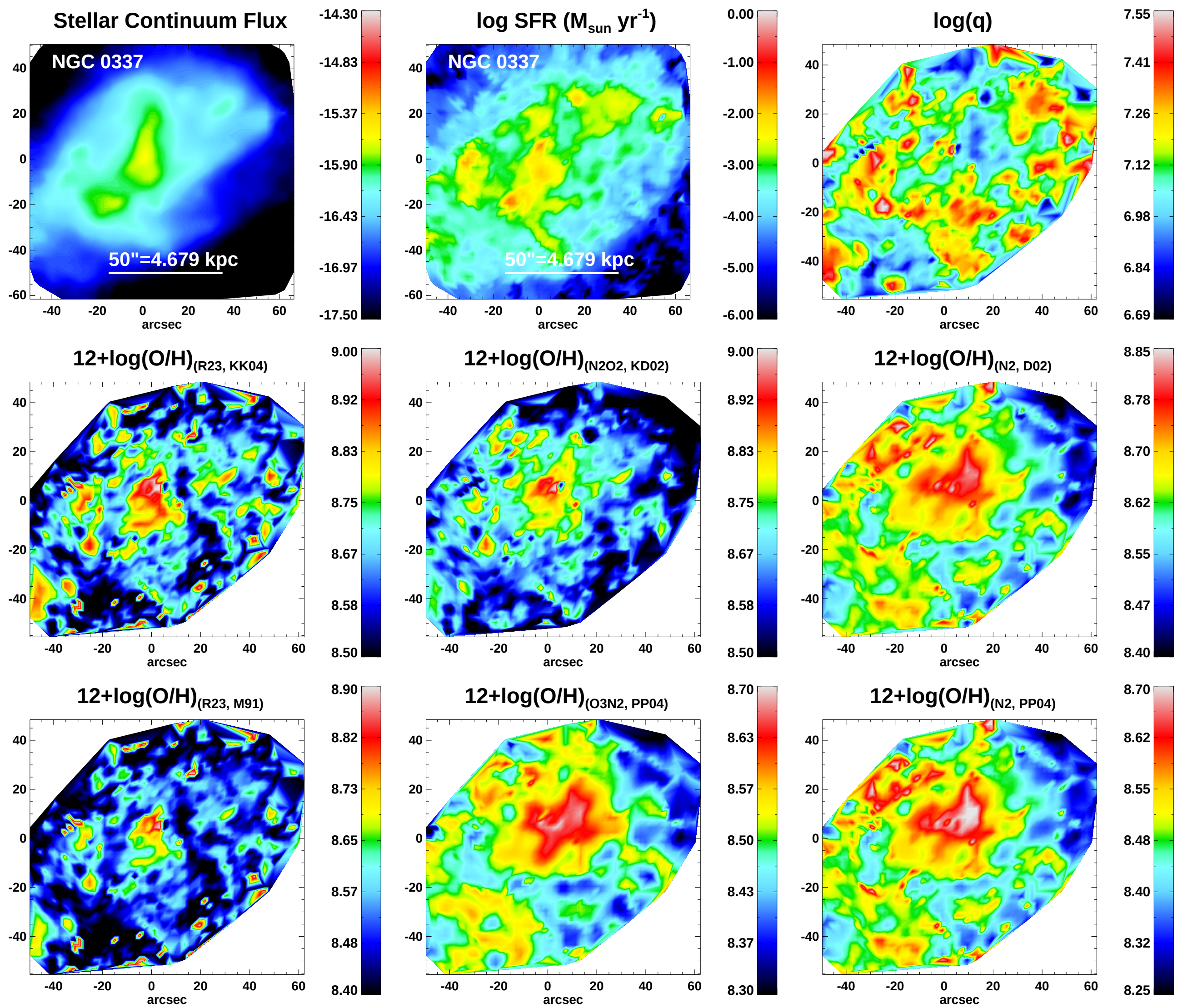

Figure 8. From left to right, top to bottom we show our 2D maps of the: **Top Left:** Bolometric stellar flux, **Top Center:** SFR derived from extinction corrected Hα flux using the calibration from Kennicutt (1998), **Top Right:** Ionization parameter q calculated as described in § 4.4, **Center Left:** Z_{gas} diagnostic $R_{23} - KK04$, **Center Center:** N2O2-KD02, **Center Right:** N2-DO2, **Bottom Left:** R_{23}-M91, **Bottom Center:** O3N2-PP04, and **Bottom Right:** N2-PP04 for NGC 0337

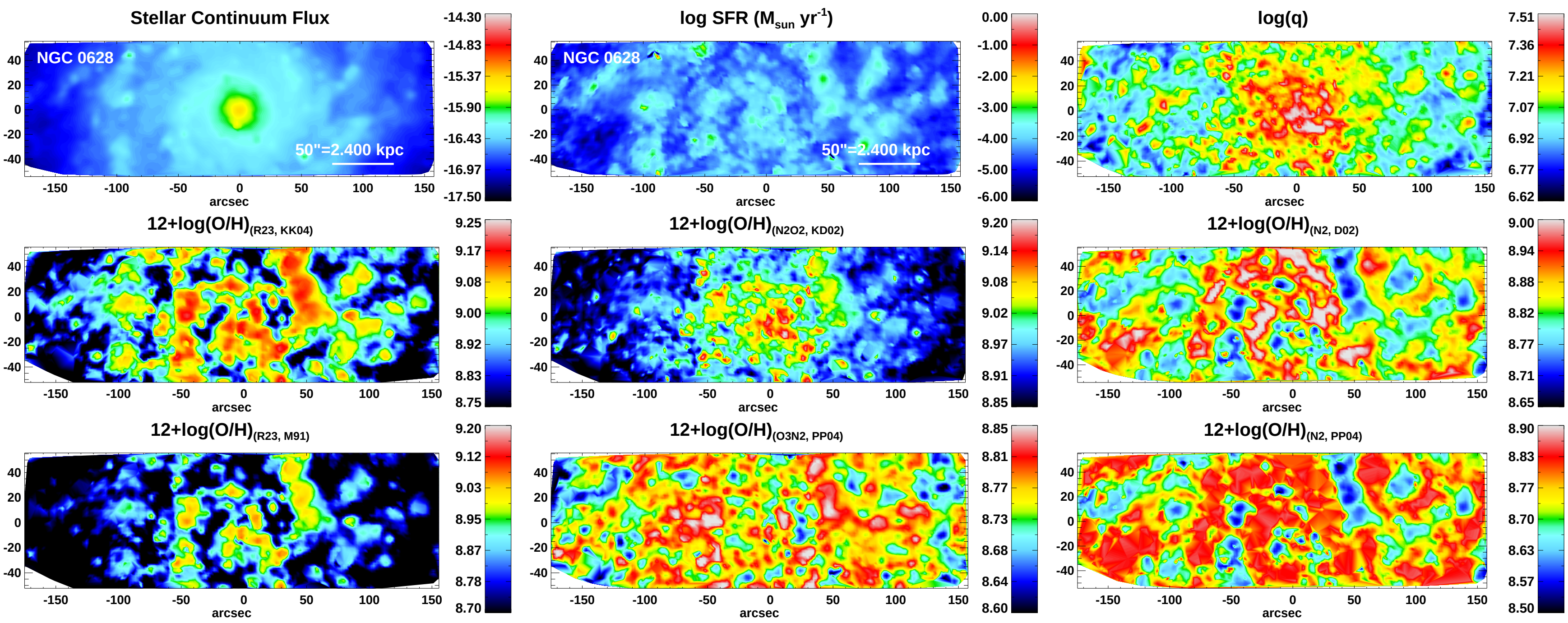

Figure 8. continued... NGC 0628

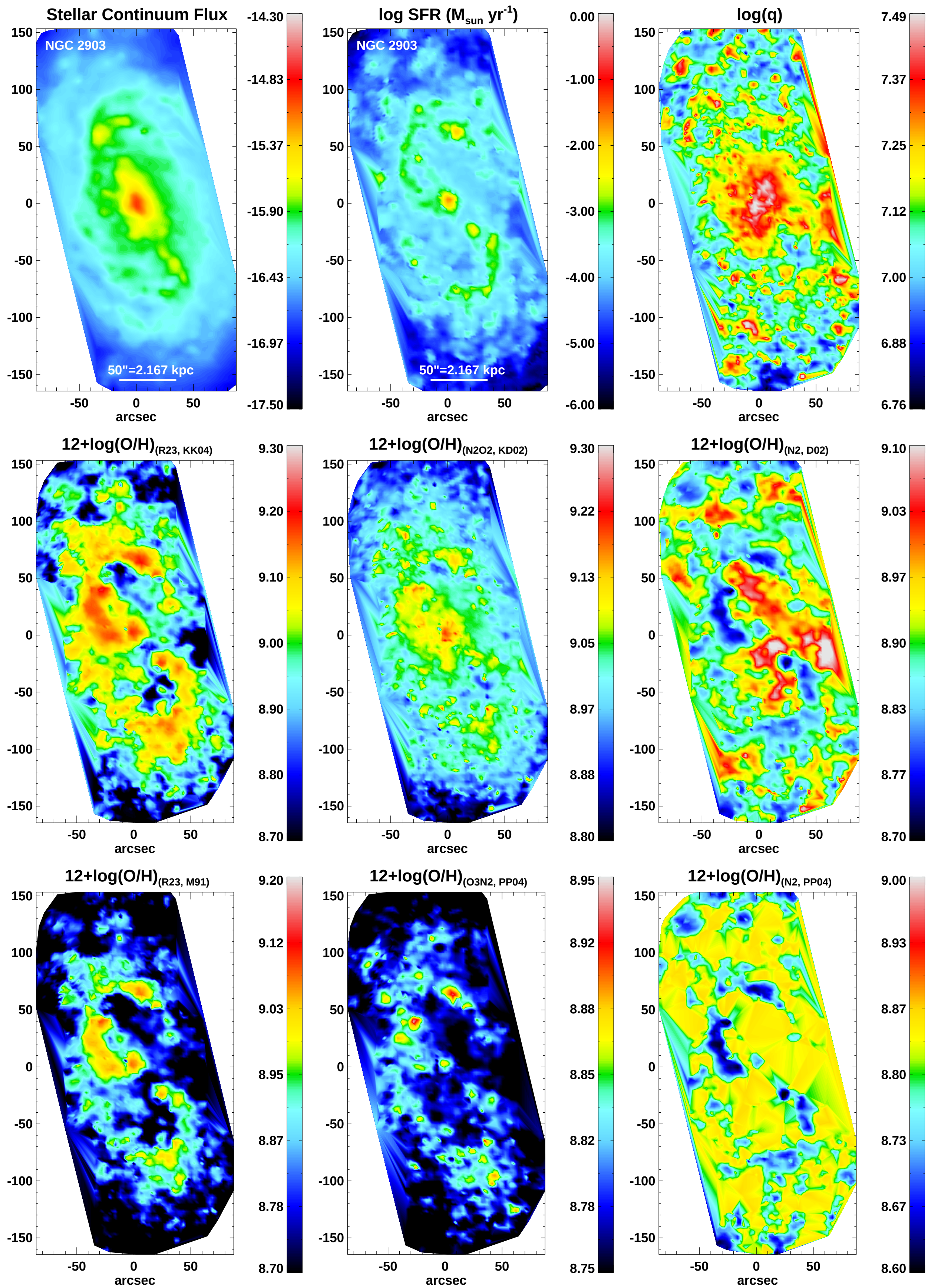

Figure 8. continued... for NGC 2903.

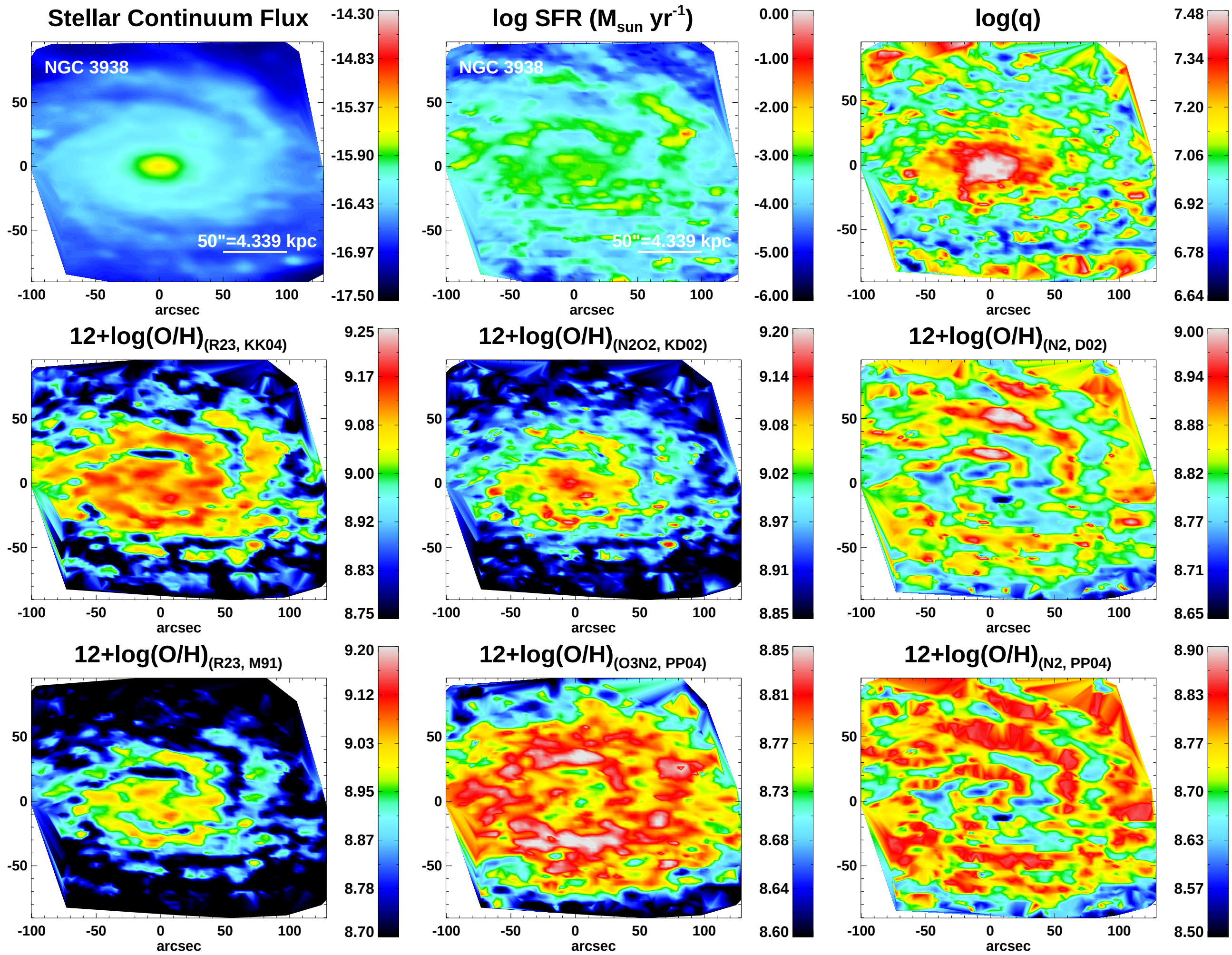

Figure 8. continued... NGC 3938.

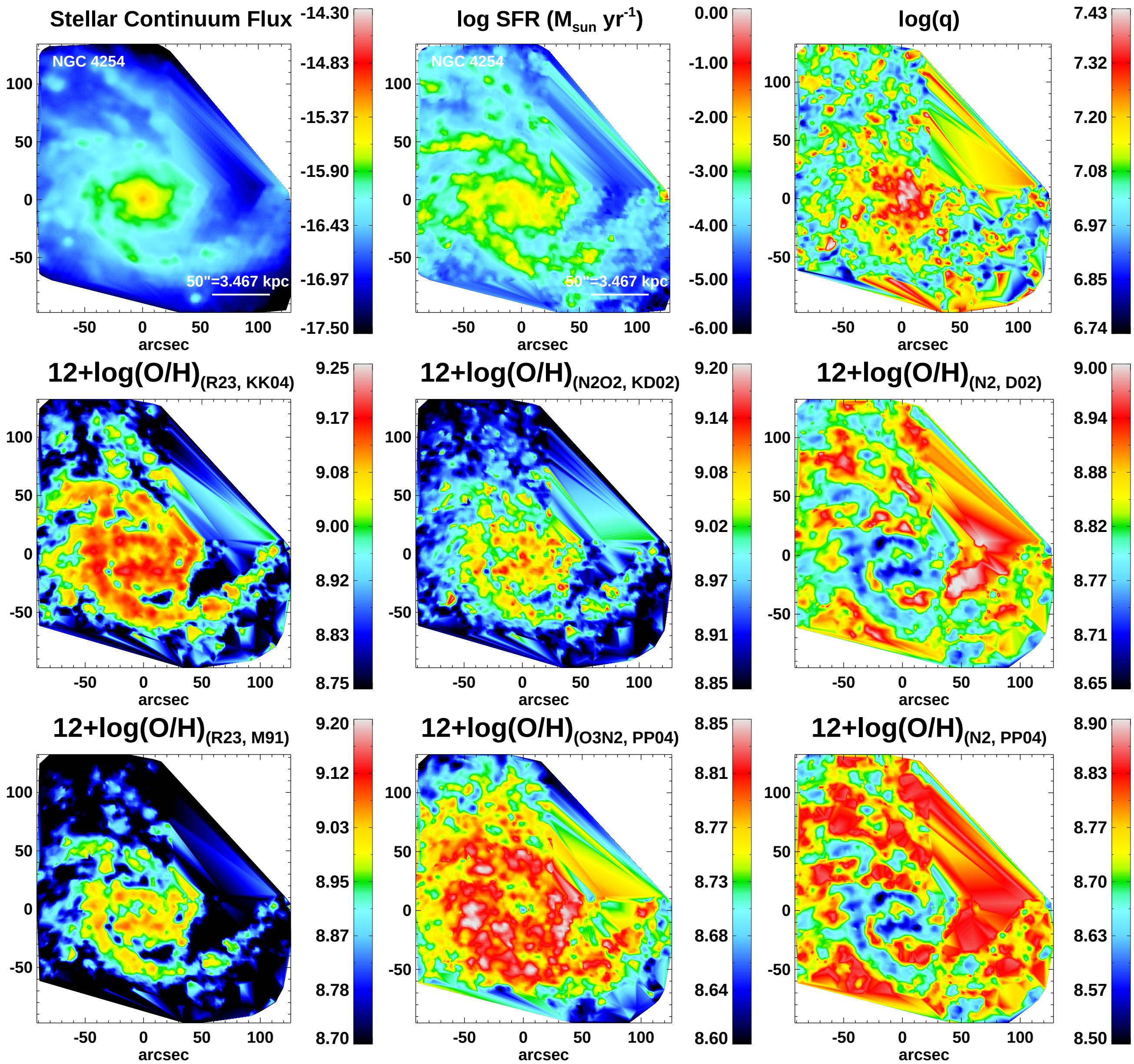

Figure 8. continued... NGC 4254.

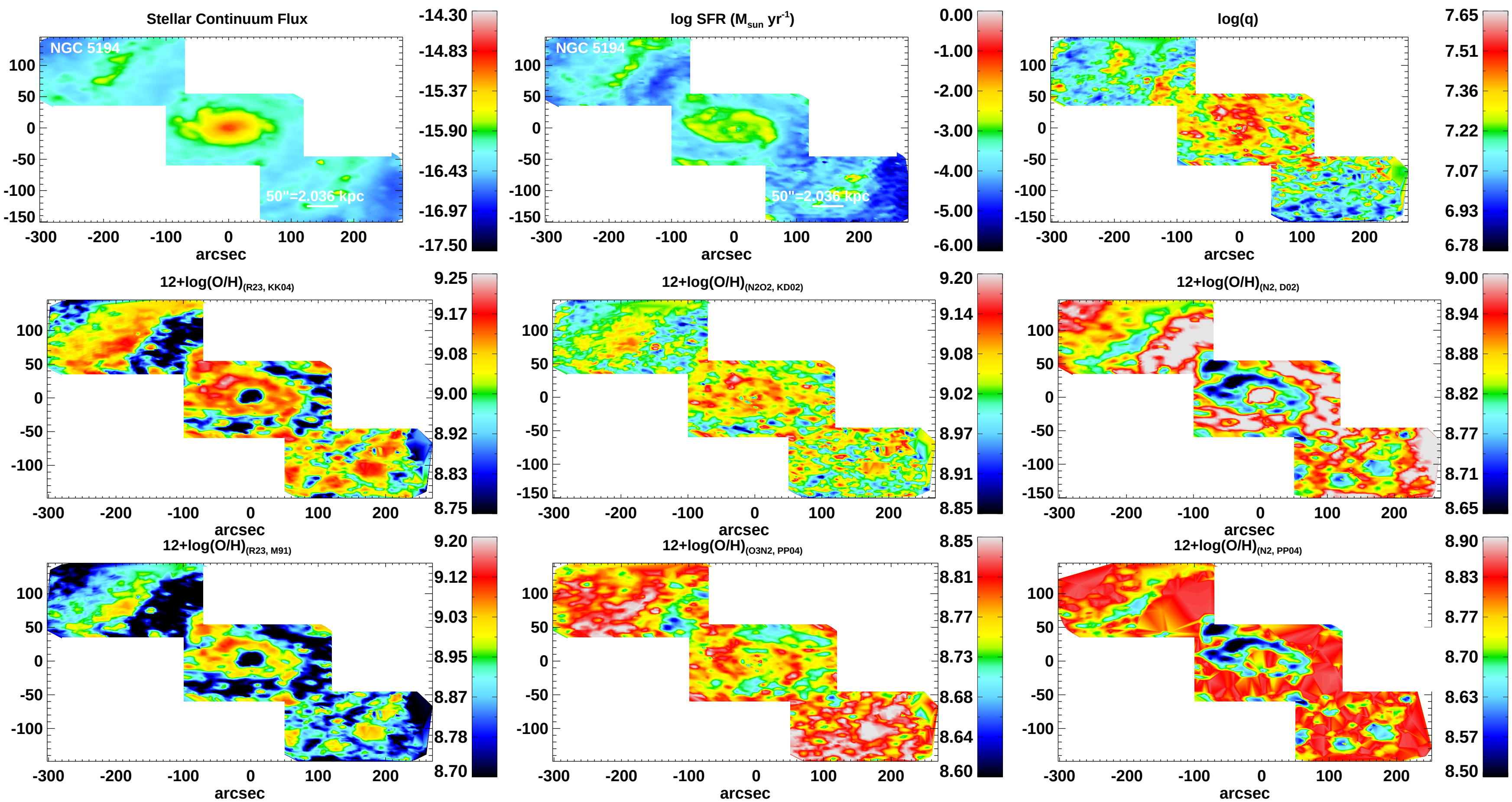

Figure 8. continued... NGC 5194

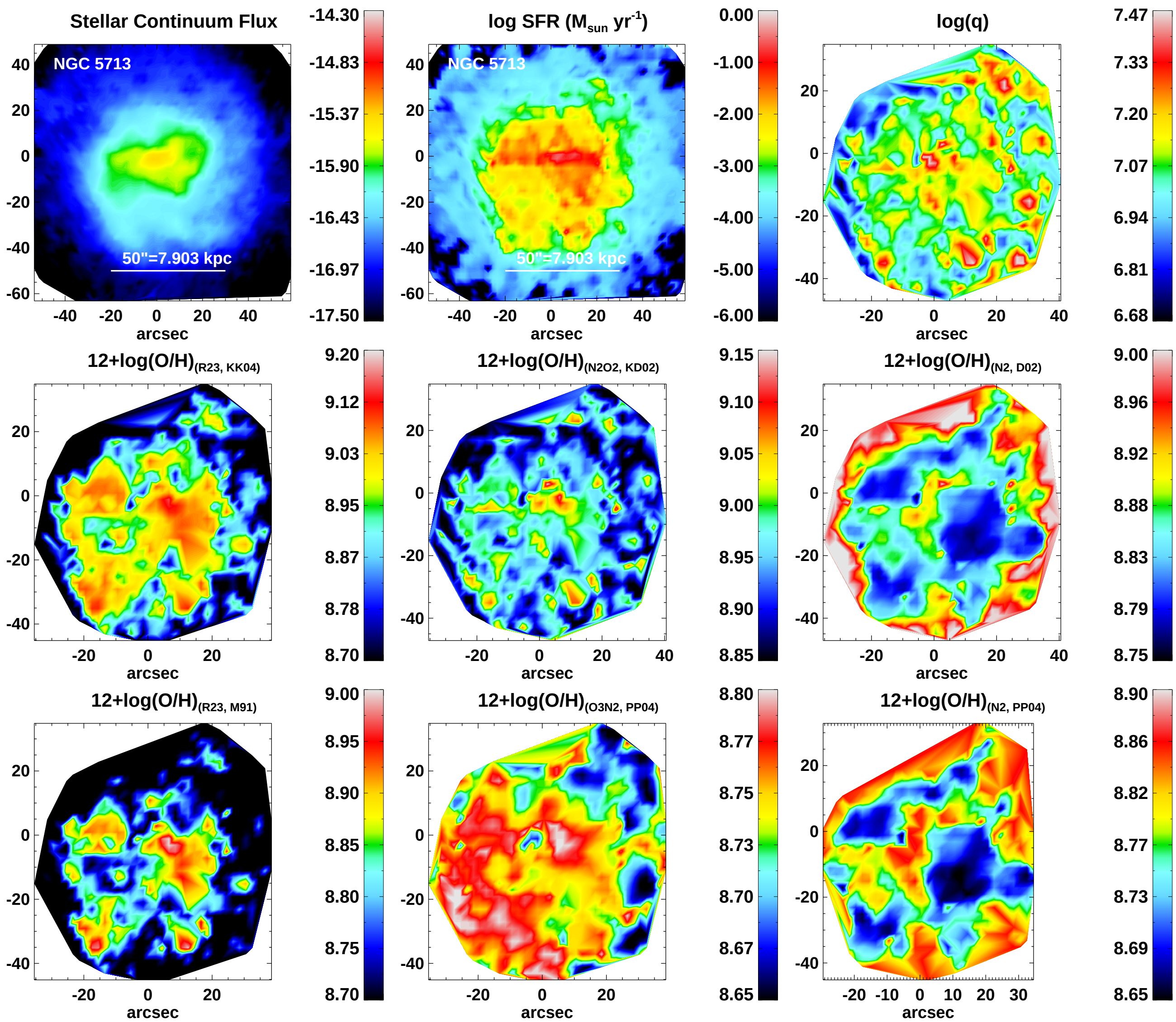

Figure 8. continued... for NGC 5713.

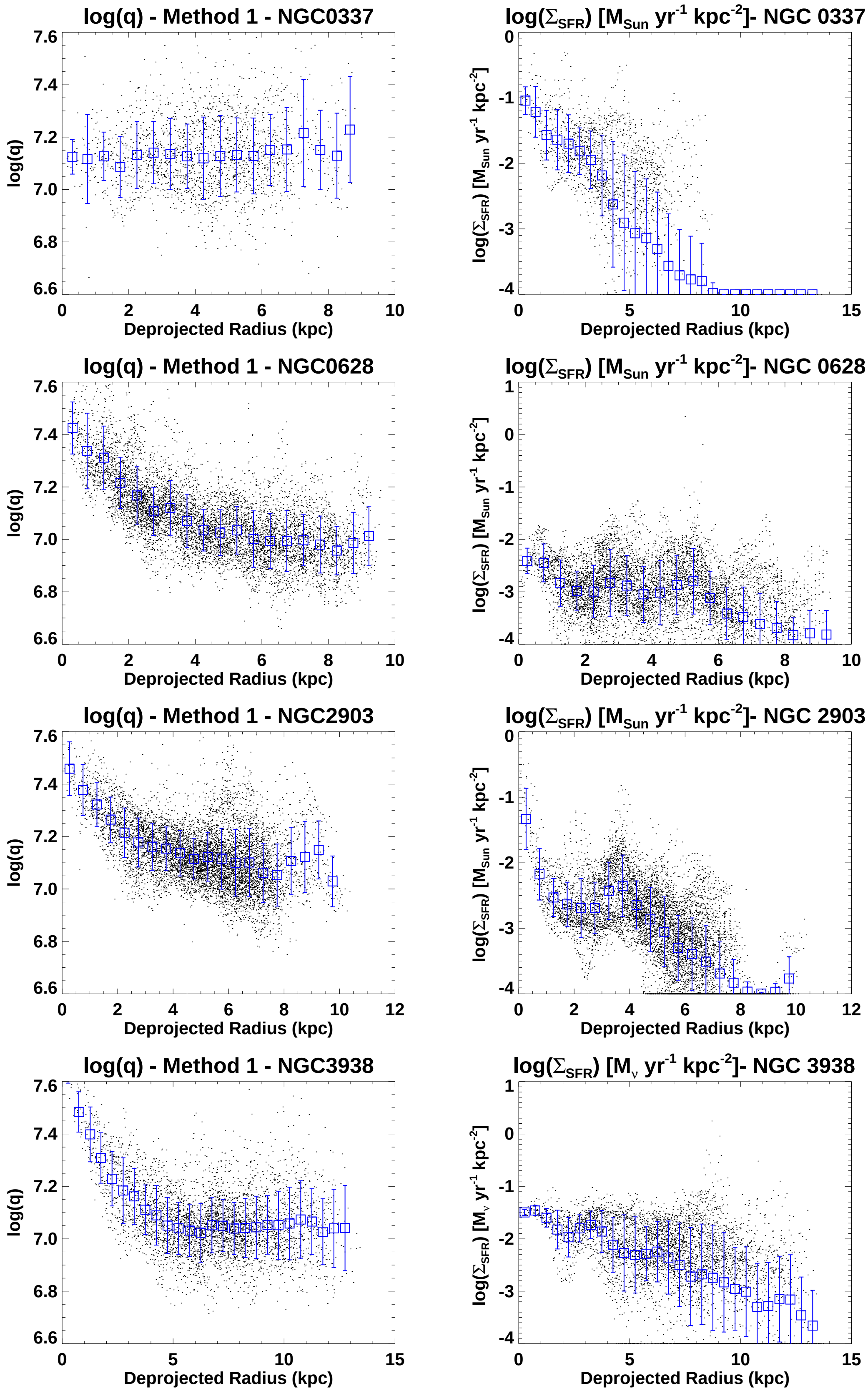

Figure 9. Azimuthally deprojected radial gradients for **Left:** the ionization parameter q (§4.4) and **Right:** the SFR surface density Σ_{SFR} ($M_{\odot}$ yr^{-1} kpc^{-2}) for the galaxies NGC 0337, 0628, 2903, & 3938 from top-to-bottom. The blue squares and error bars are the mean and 1σ dispersion of 0.5 kpc bins.

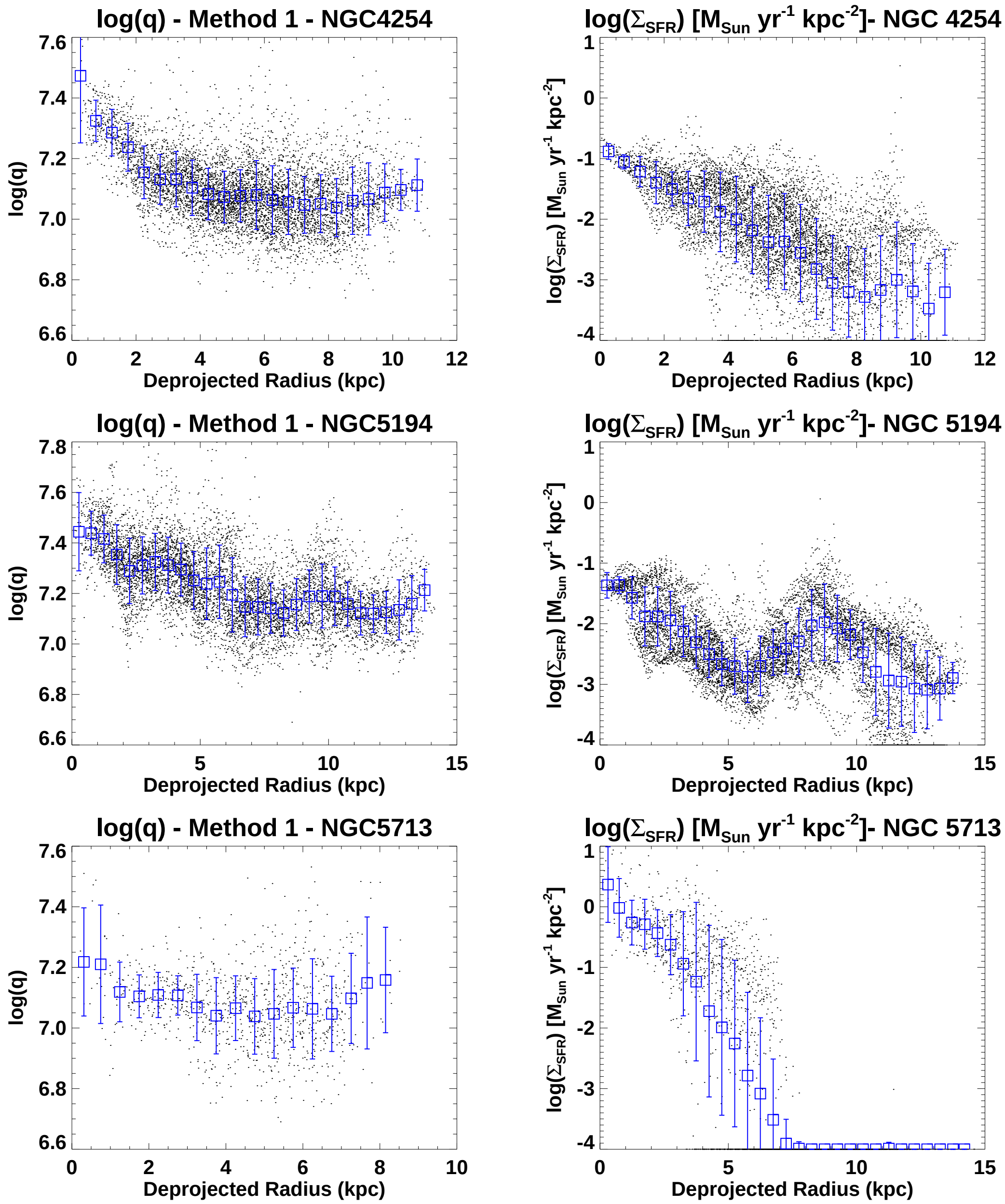

Figure 9. Continted for... NGC 4254, 5194, & 5713.

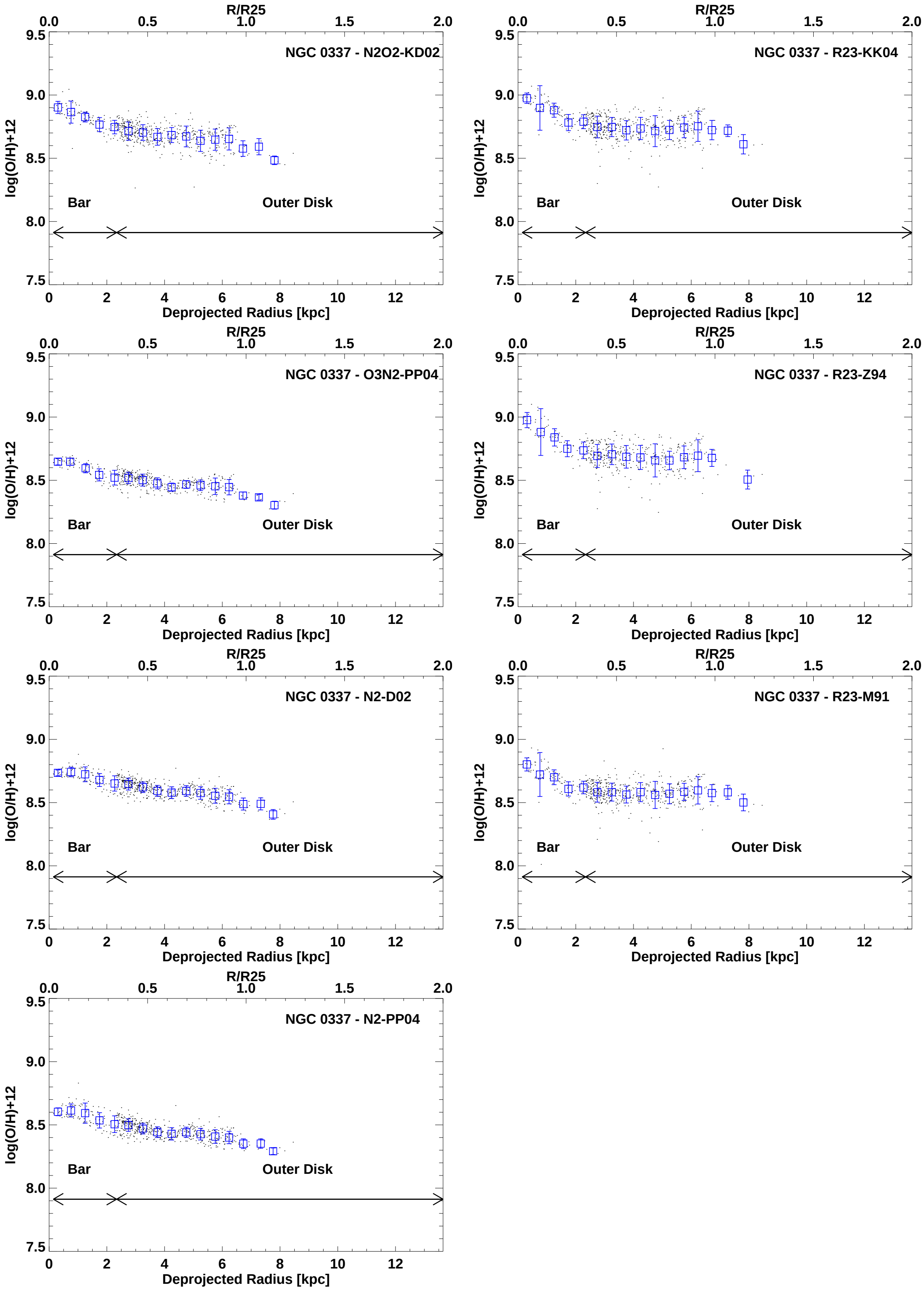

Figure 10. Azimuthally deprojected radial Z_{gas} gradients for NGC 0337 for the seven different Z_{gas} diagnostics we use. The arrows on the bottom show our decomposition of each galaxy into non-classical (NC, ie. disky or pseudo) bulge, bar, and outer disk. In the barred region we separate fibers in the bar as the black points and fibers not in the bar as the red points. The blue squares and error bars show the average and 1σ dispersion for 0.5 kpc bins for our data. For binning at radii labeled bar, we use only fibers within the bar. The Z_{gas} diagnostics, as shown in the order of left-to-right and top-to-bottom, are: N202-KD02, R_{23}-KK04, O3N2-PP04 R_{23}-Z94, N2-D02, R_{23}-M91, & N2-PP04. Note that for the N2-PP04 diagnostic, we only consider fibers with $-2.5 < \log([\mathrm{NII}]/H\alpha) < -0.3$, hence the cutoff at high log(O/H)+12 when compared to the N2-D02 diagnostic.

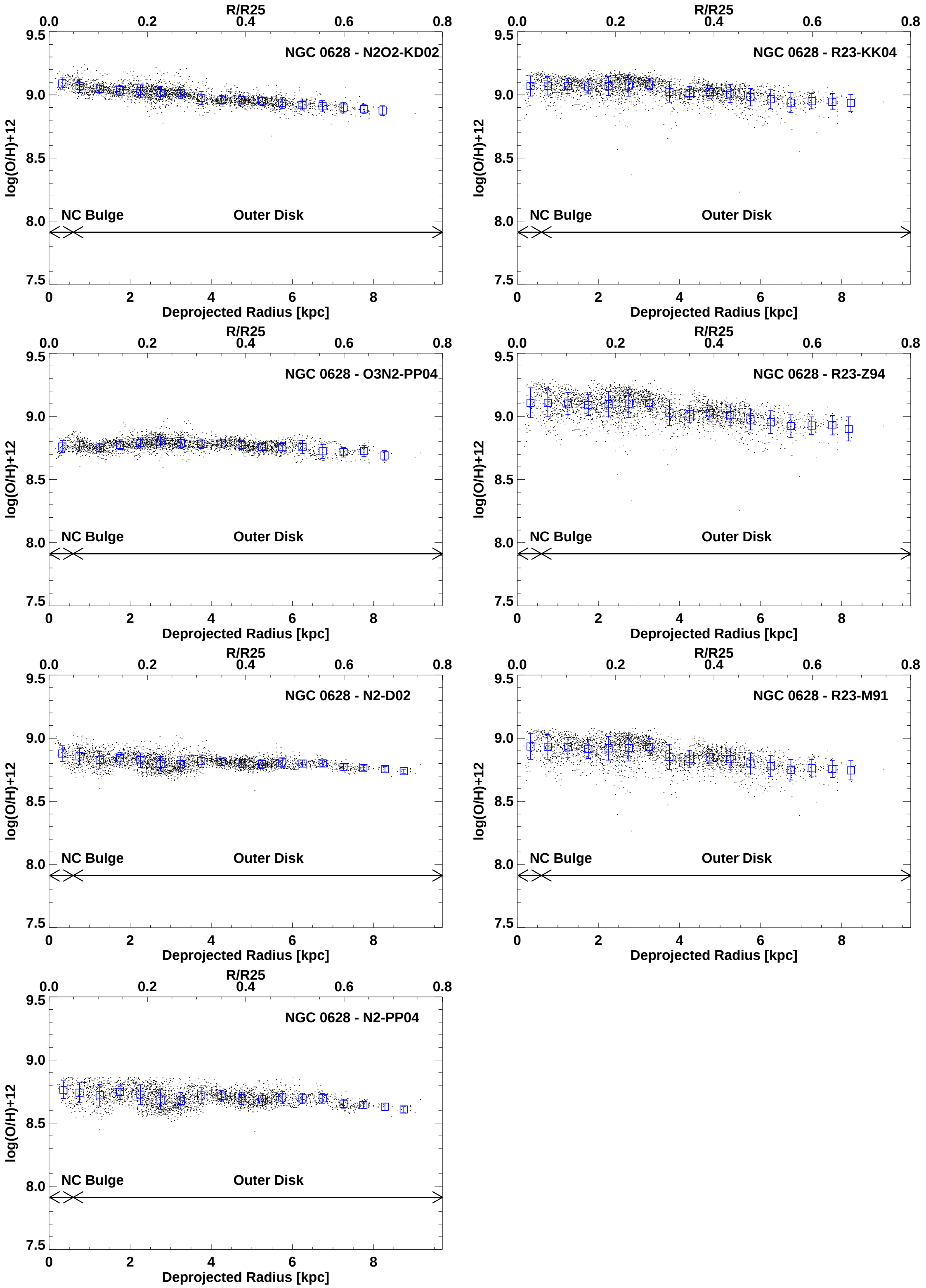

Figure 10. continued... for NGC 0628.

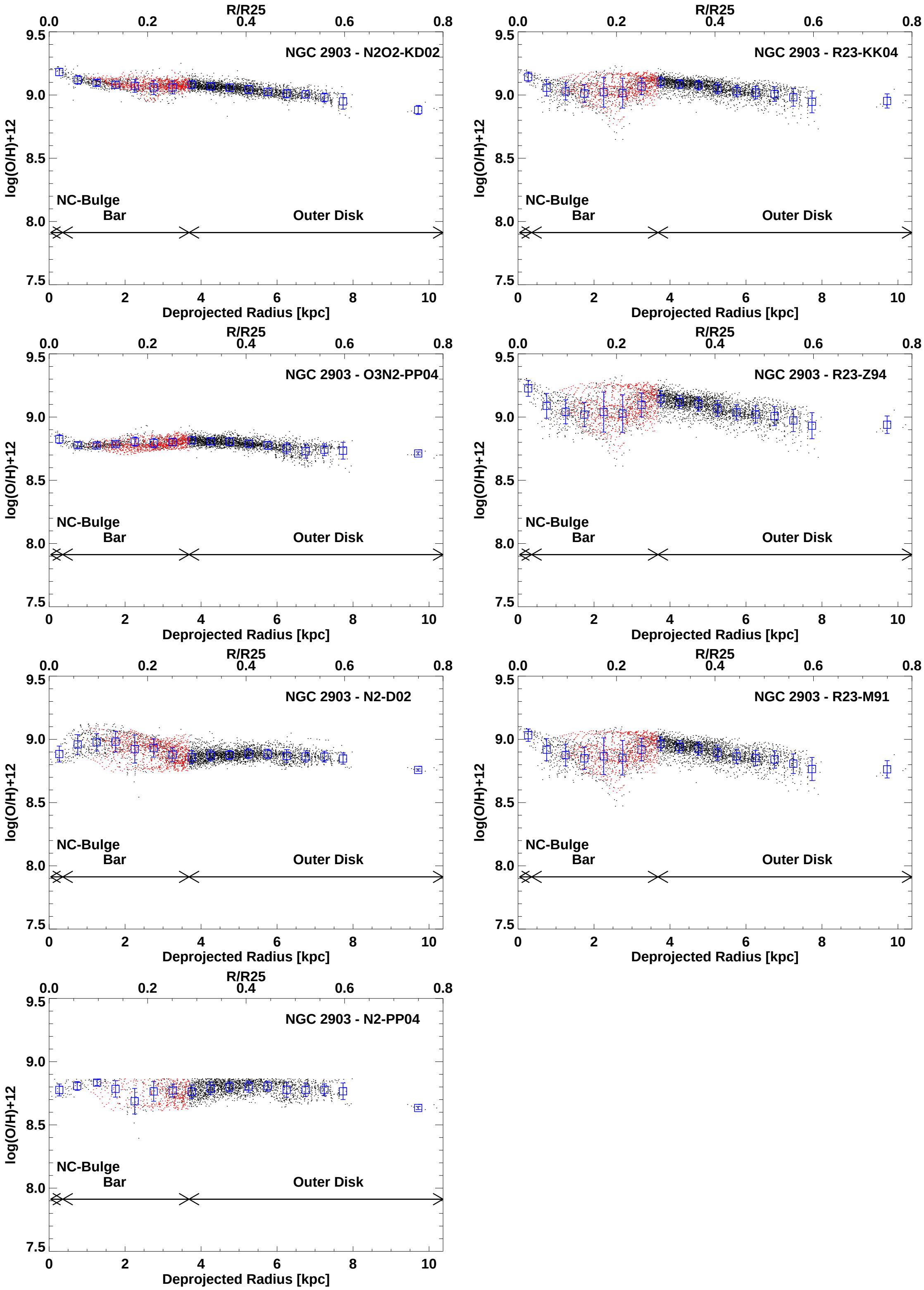

Figure 10. continued... for NGC 2903.

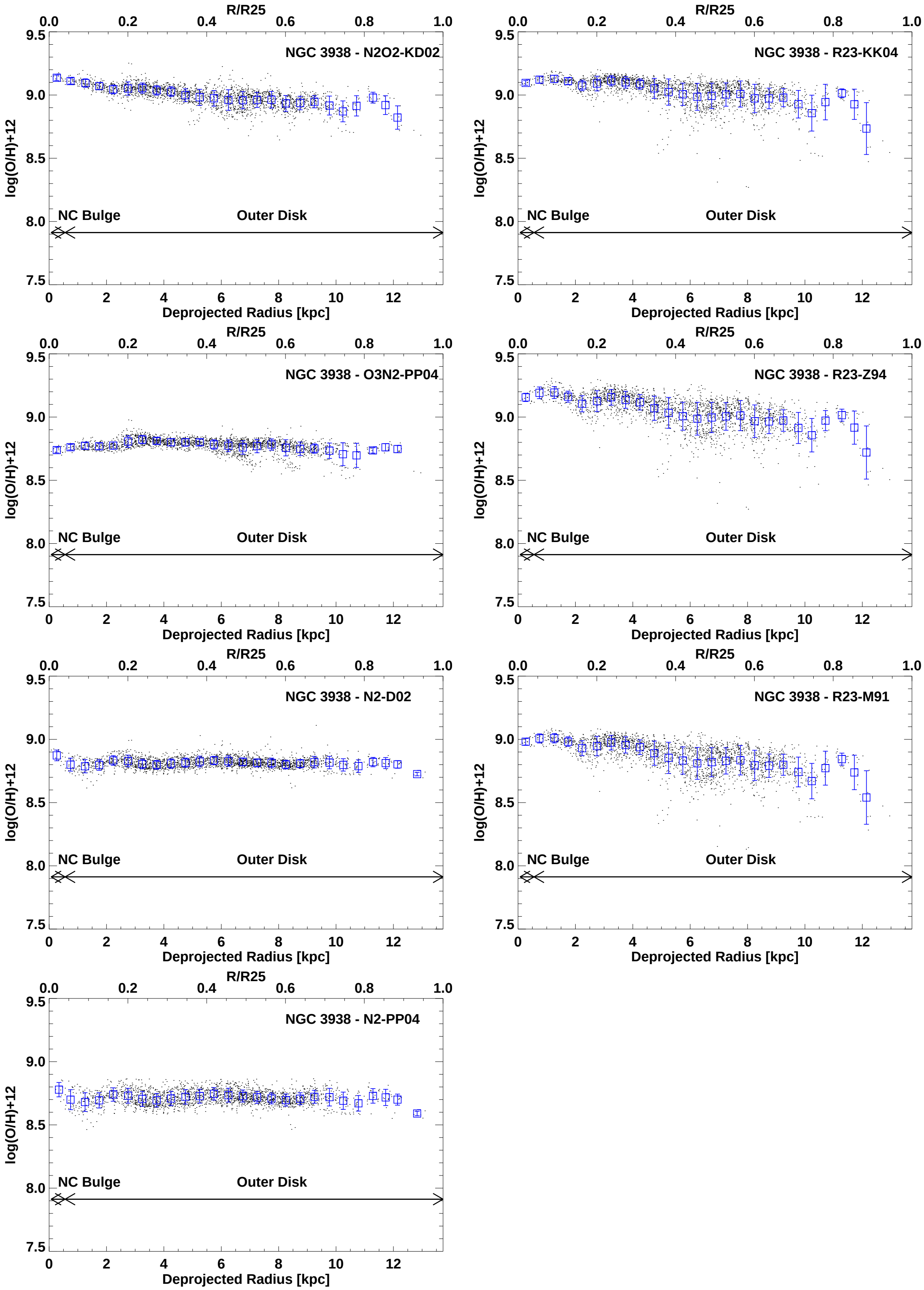

Figure 10. Continued... for NGC 3938.

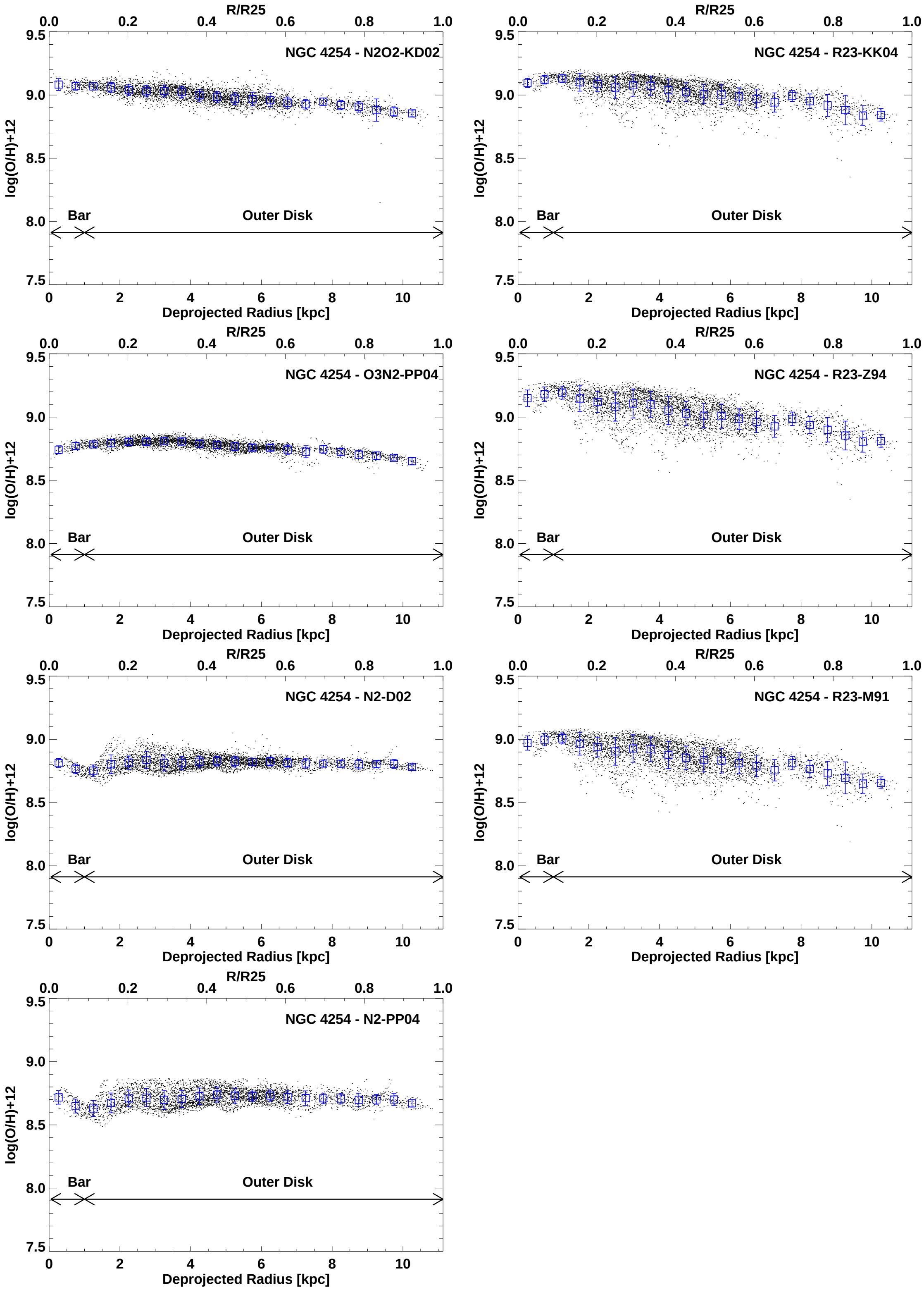

Figure 10. Continued... for NGC 4254.

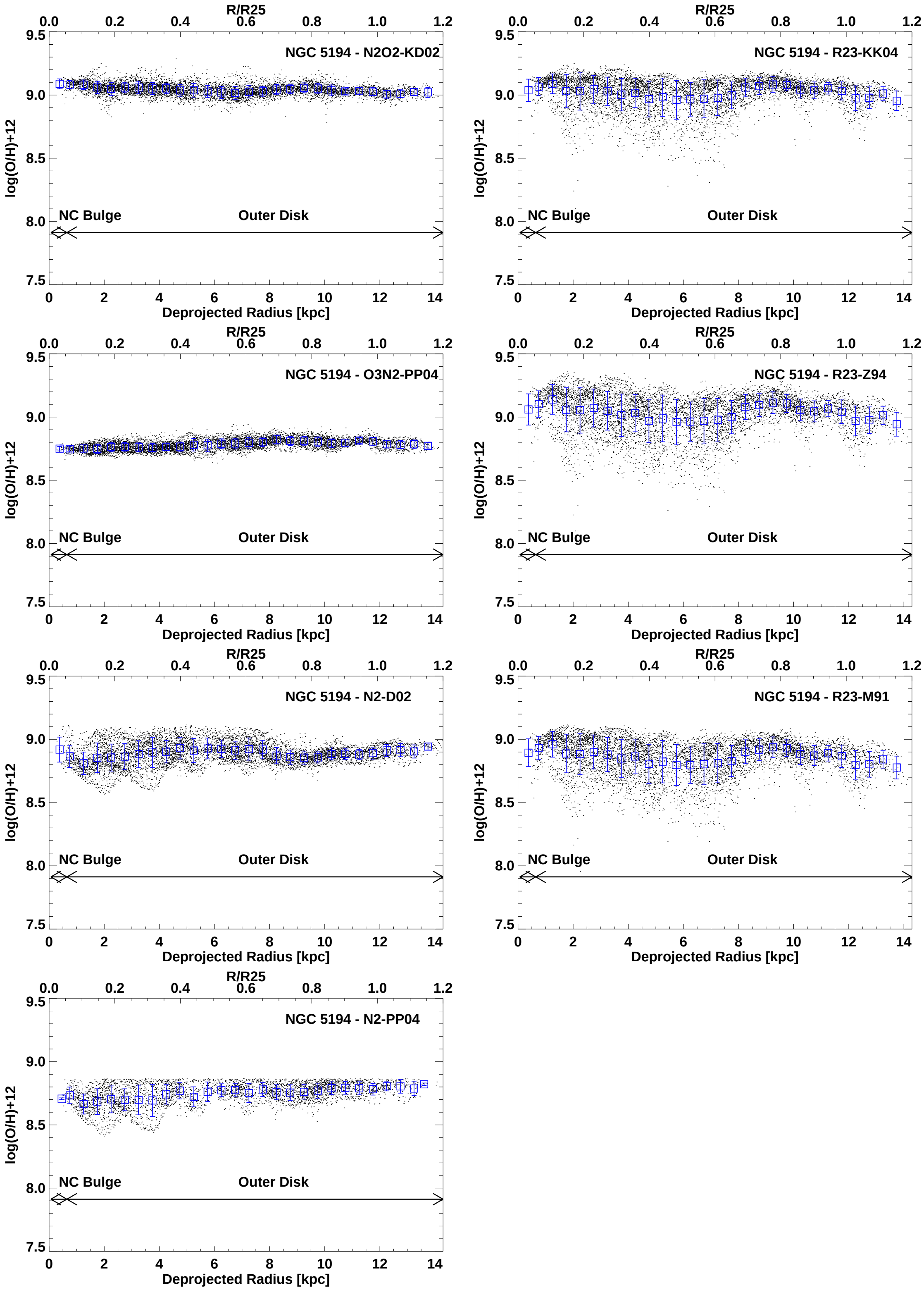

Figure 10. Continued... for NGC 5194.

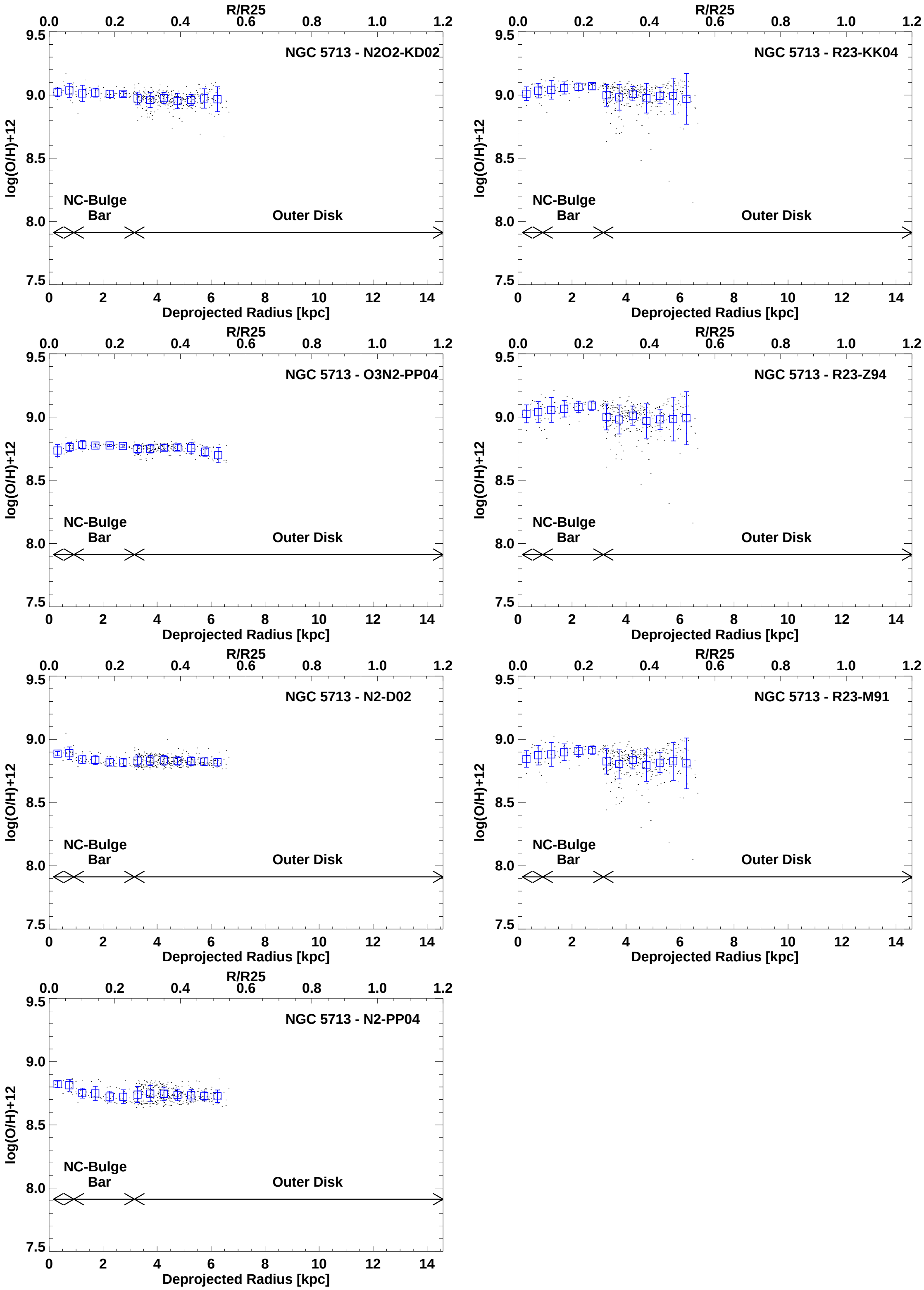

Figure 10. continued... for NGC 5713.

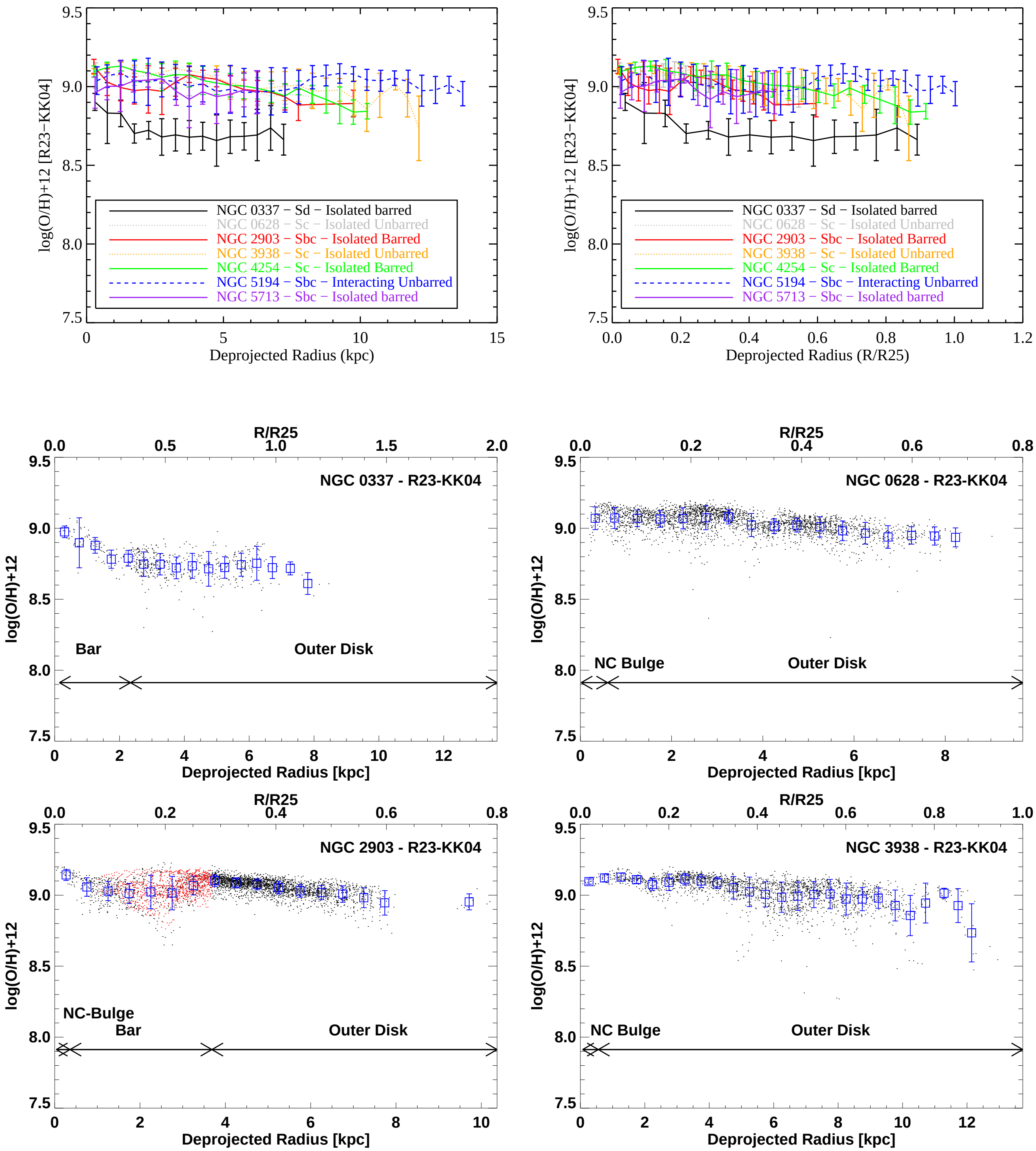

Figure 11. Comparison of azimuthally deprojected Z_{gas} gradients using the R_{23}-KK04 Z_{gas} diagnostic for NGC 0337 **(Center Left)**, NGC 0628 **(Center Right)**, NGC 2903 **(Bottom Left)**, NGC 3938 **(Bottom Right)**. The arrows on the bottom show our decomposition of each galaxy into non-classical (NC, ie. disky or pseudo) bulge, bar, and outer disk. In the barred region we separate fibers in the bar as the black points and fibers not in the bar as the red points. The blue squares and error bars show the average and 1σ dispersion for 0.5 kpc bins for our data. For binning at radii labeled bar, we use only fibers within the bar. We also overplot the Z_{gas} gradients for all our galaxies against the deprojected radius in **(Top Left)** kpc and in **(Top Right)** R/R25. The solid lines are for isolated barred galaxies, the dotted lines for isolated unbarred galaxies, and the dashed line for our interacting unbarred galaxy NGC 5194.

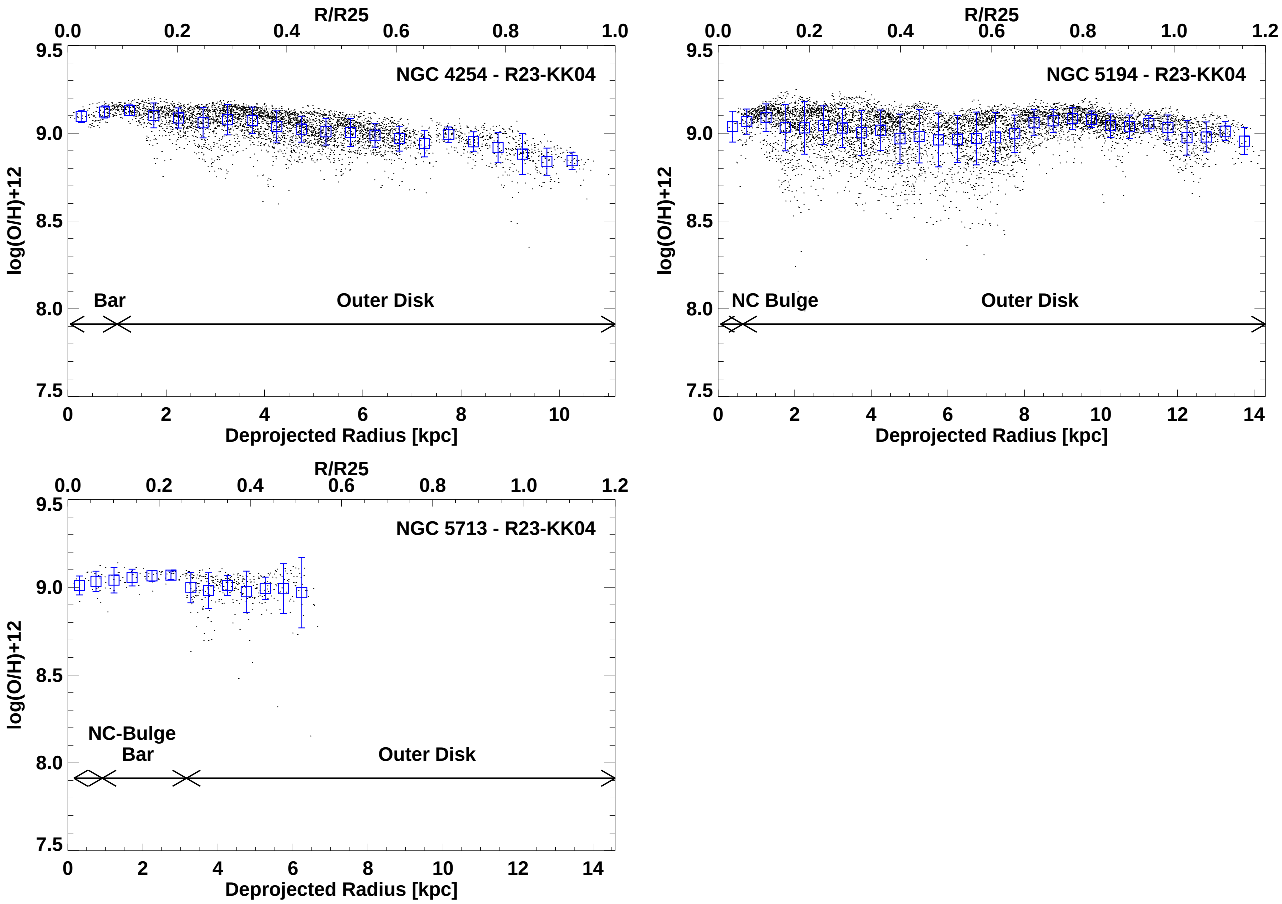

Figure 11. Continued for NGC 4254 **(Top Left)**, NGC 5194 **(Top Right)**, & NGC 5713 **(Bottom Left)**.

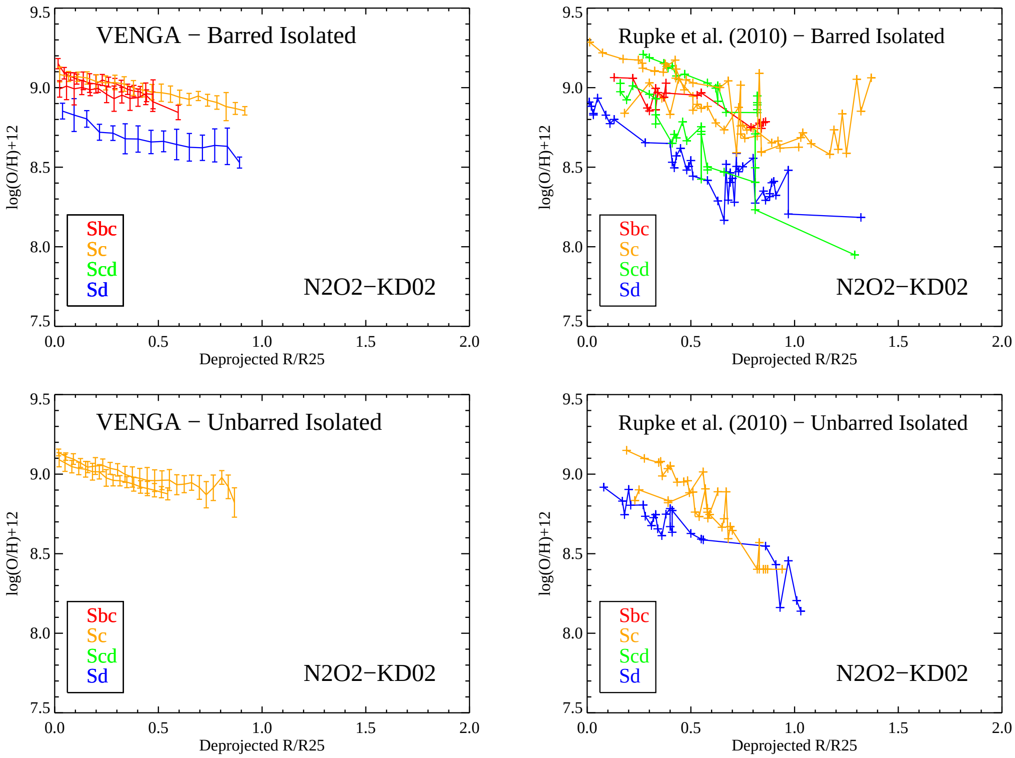

Figure 12. Comparison of R/R25 Z_{gas} gradients for isolated barred VENGA galaxies **(Top Left)** and isolated unbarred VENGA galaxies **(Bottom Left)** to control sample of isolated barred **(Top Right)** and isolated unbarred **(Bottom Right)** galaxies from the Rupke et al. (2010b) control sample for the N2O2-KD02 Z_{gas} diagnostic.

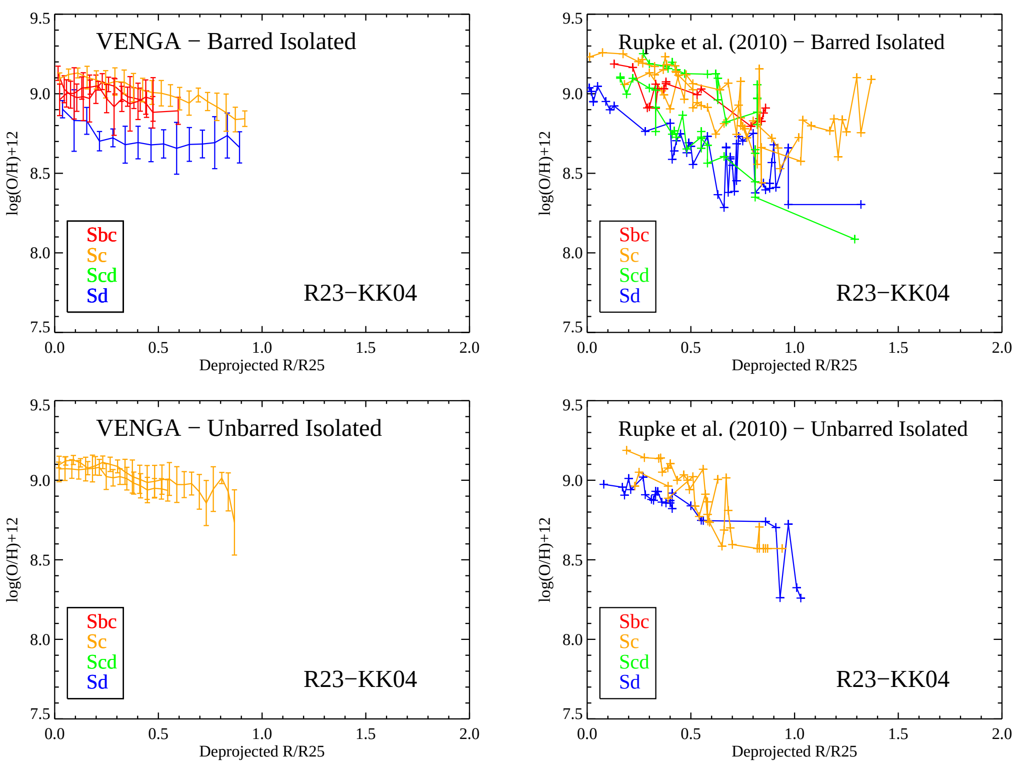

Figure 13. Same as for Figure 12 but for the R23-KK04 Z_{gas} diagnostic.

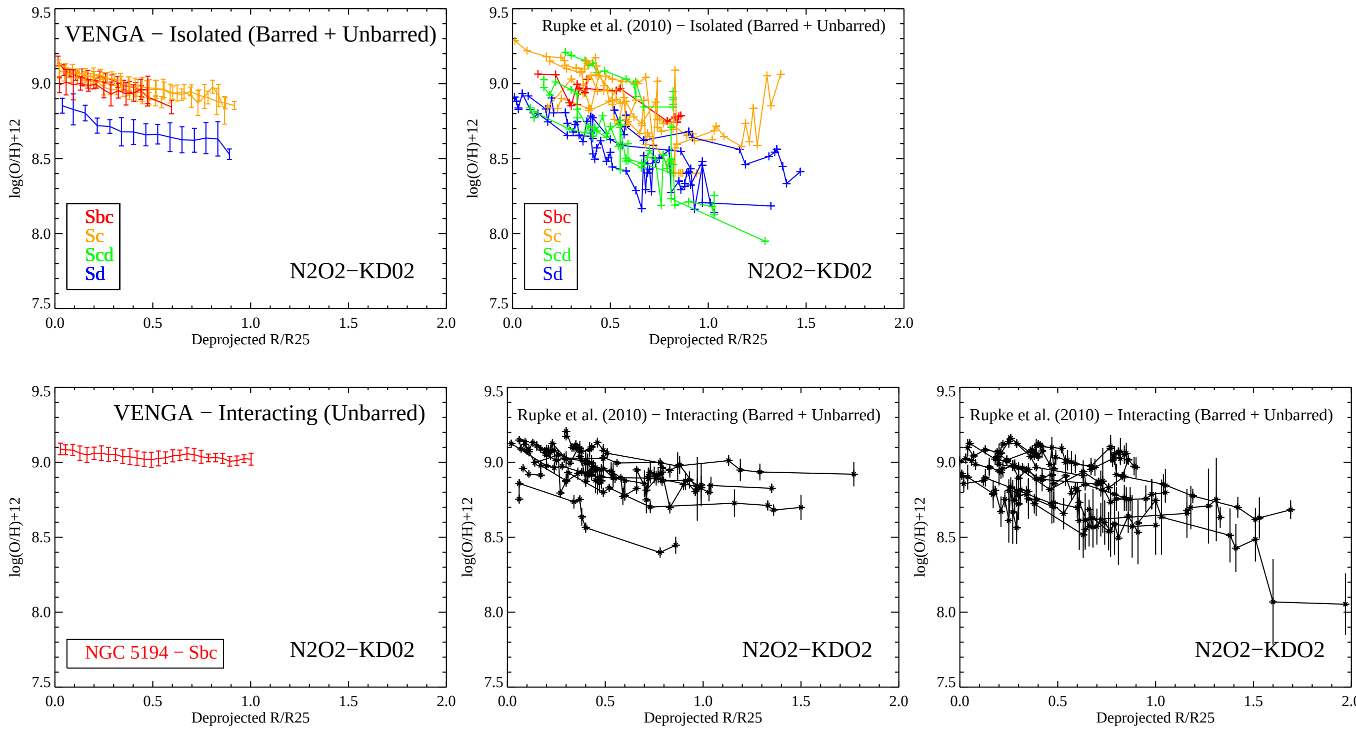

Figure 14. Comparison of R/R25 Z_{gas} gradients for isolated VENGA galaxies **(Top Left)** galaxies and the one interacting VENGA galaxy **(Bottom Left)** to isolated galaxies **(Top Center)** interacting galaxies **(Bottom Center & Right)** from Rupke et al. (2010b) with the N2O2-KD02 Z_{gas} diagnostic. The bottom center & right plots are both from the same sample of interacting galaxies and have been split into two plots for clarity.

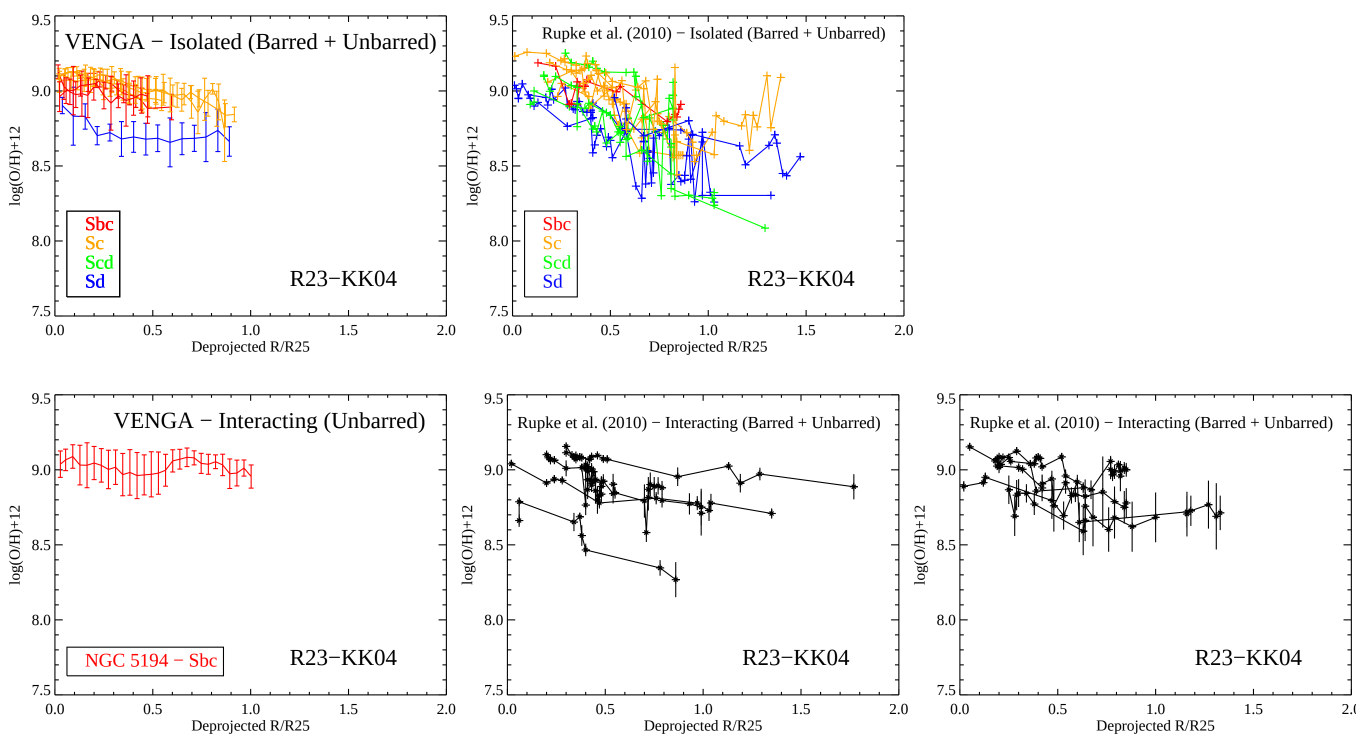

Figure 15. Same as for Figure 14 but for the R23-KK04 Z_{gas} diagnostic.

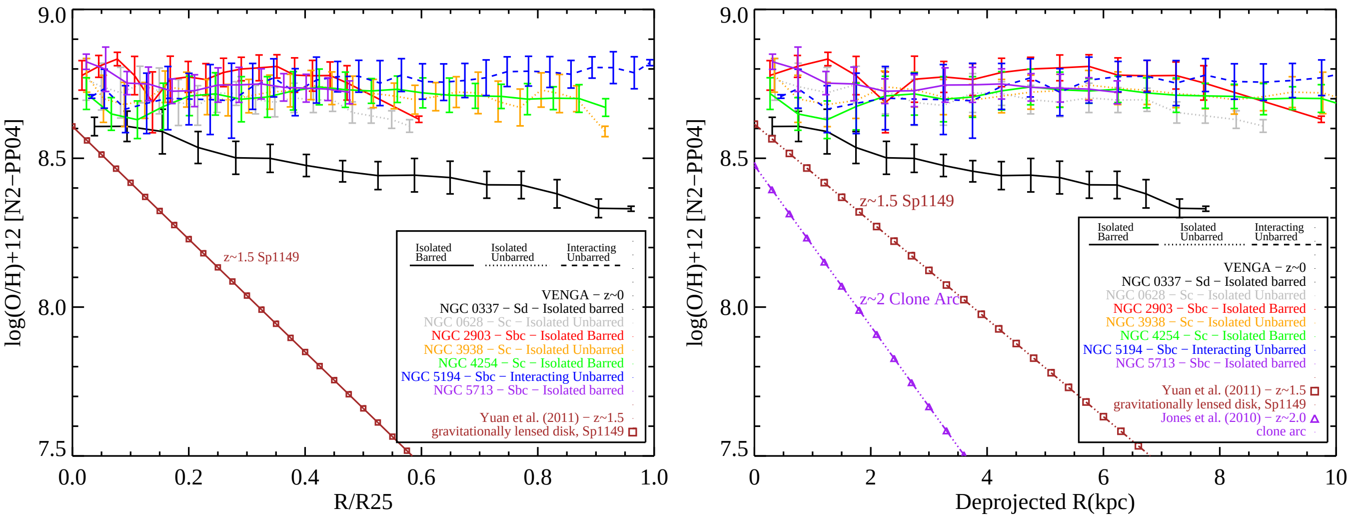

Figure 16. Left: Comparison of Z_{gas} gradients in R/R25 of our local ($z \sim 0$) VENGA subsample to the higher redshift ($z \sim 1.5$) gravitationally lensed disk galaxy Sp1149 (Yuan et al. 2011). **Right:** Comparison of Z_{gas} gradients in R(kpc) of our local ($z \sim 0$) VENGA subsample to Sp1149 ($z \sim 1.5$), and also the z∼2 "clone arc" from Jones et al. (2010). Sp1149 and the "clone arc" shows a significantly steeper gradient than our $z \sim 0$ VENGA subsample. We interpret these observations as the evolution in Z_{gas} gradients over cosmic time, where the gradients appear to become flatter with age.

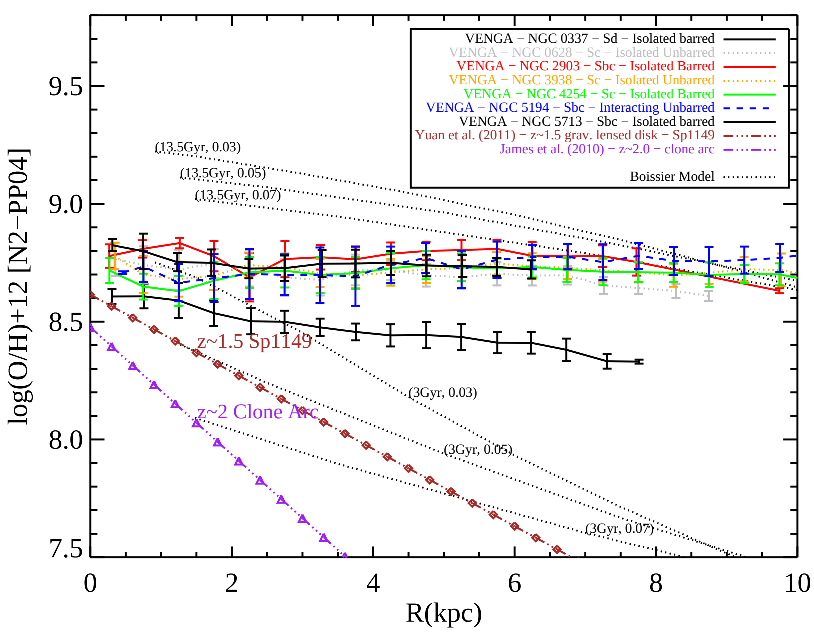

Figure 17. Comparison of Z_{gas} gradients in R(kpc) of our local ($z \sim 0$) VENGA subsample to the higher redshift ($z \sim 1.5$) gravitationally lensed disk galaxy Sp1149 (Yuan et al. 2011), the ($z \sim 2$) clone arc (Jones et al. 2010), and the model by Boissier (Muñoz-Mateos et al. 2011; Boissier & Prantzos 1999) at z∼1.5 (age∼3 Gyr) and z∼0 (age∼13.5 Gyr) assuming parameters to match Sp1149 of a circular velocity of 200 km s^{-1} and dimensionless spin parameters of 0.03, 0.05, & 0.07. The age and dimensionless spin parameters are labeled in parenthesis on the plot.

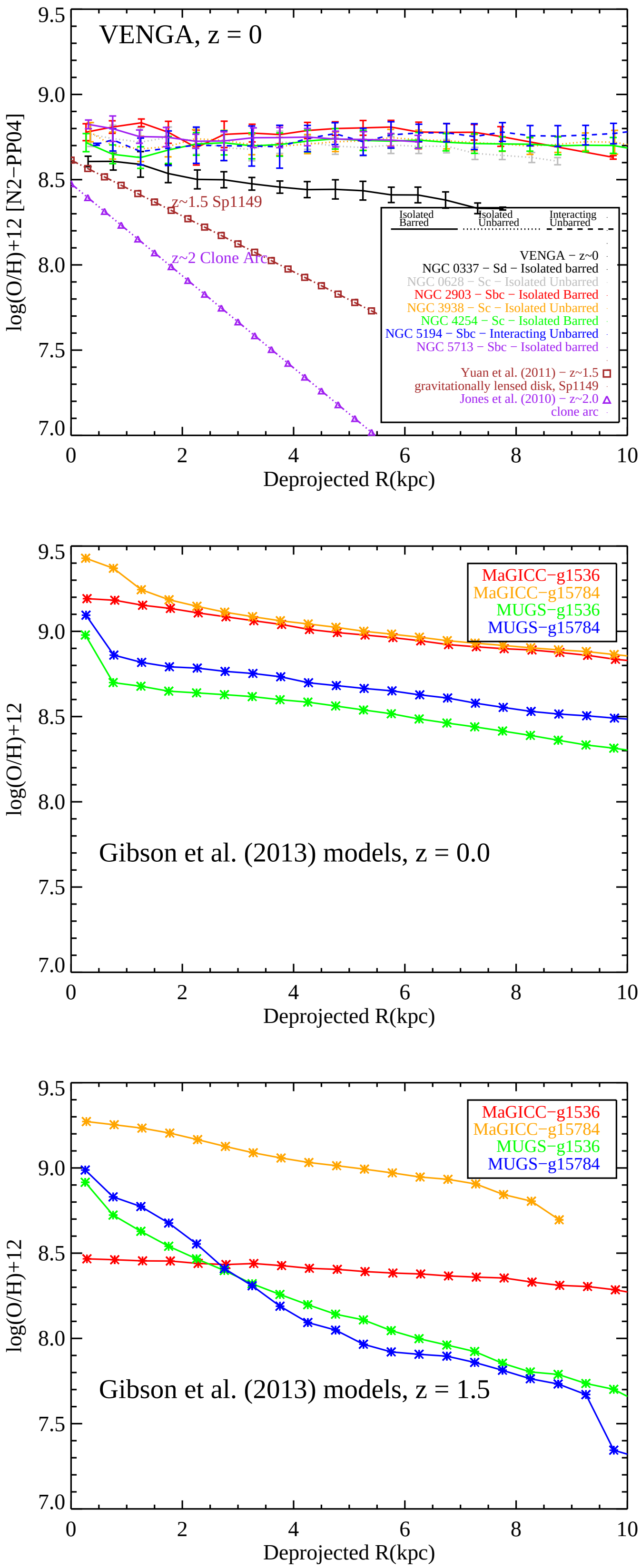

Figure 18. Comparison of of Z_{gas} gradients in R(kpc) of **Top:** our local ($z \sim 0$) VENGA subsample, the higher redshift ($z \sim 1.5$) gravitationally lensed disk galaxy Sp1149 (Yuan et al. 2011), and the ($z \sim 2$) clone arc (Jones et al. 2010) to the **Center:** z=0 and **Bottom:** z=1.5 MaGICC and MUGS models for the simulated disk galaxies g1536 & g15784 (Gibson et al. 2013; Pilkington et al. 2012).

APPENDIX A: HOW IONIZATION PARAMETER Q IS DETERMINED ITERATIVELY FOR THE R_{23}-KK04 DIAGNOSTIC - METHOD 2

The iterative determination of q is based off of the R_{23} Z_{gas} diagnostic in Kobulnicky & Kewley (2004), and this procedure is detailed in Appendix A2.1 of Kewley & Ellison (2008). R_{23} is dependent on q (see Figure 7 on the top right) so we iterate to converge on a Z_{gas} and q for this Z_{gas} indicator. First, an initial Z_{gas} is assumed by breaking the double valued degeneracy of R_{23} using [NII]/[OII]. Breaking the double valued degeneracy is described in detail in Appendix A1 of Kewley & Ellison (2008), in summary:

$$\text{upper branch}: \quad \log([\text{NII}]/[\text{OII}]) \geqslant -1.2 \qquad \text{lower branch}: \quad \log([\text{NII}]/[\text{OII}]) < -1.2 \tag{A1}$$

For each branch, the code assumes an initial Z_{gas} of:

$$\text{upper branch}: \quad \text{initial } \log(\text{O/H}) + 12 = 8.7 \qquad \text{lower branch}: \quad \text{initial } \log(\text{O/H}) + 12 = 8.2 \tag{A2}$$

This first initial guess for Z_{gas} and [OIII]/[OII] is used to make an initial guess at q using the following (See Eq. 13 in Kobulnicky & Kewley 2004):

$$y = \log([\text{OIII}]/[\text{OII}]) \qquad Z = \text{initial } \log(\text{O/H}) + 12 \tag{A3}$$

$$\log q = \frac{32.81 - 1.153y^2 + Z(-3.396 - 0.025y + 0.1444y^2)}{4.603 - 0.3119y - 0.163y^2 + Z(-0.48 + 0.0271y + 0.02037y^2)} \tag{A4}$$

With the initial guess for Z_{gas} and q for each fiber, the we iterate up to 10 times to try to constrain Z_{gas} and q. First Z_{gas} is calculated from R_{23} and the initial guess for q, then we recalculates q using the Z_{gas} we just calculated and [OIII]/[OII]. For the next iteration, the calculated q is then used to recalculate Z_{gas}. If the Z_{gas} difference between two iterations is $\Delta Z_{gas} < 0.01$ then the iterations stop and Z_{gas} and q are set for that fiber. If, after 10 iterations, there is no convergence, that fiber is flagged as a bad fit. This iteration makes use of R_{23}:

$$R_{23} = ([\text{OII}] + [\text{OIII}])/H\beta \tag{A5}$$

For each iteration, Z_{gas} is calculated for the upper and lower branches as:

$$\log(\text{O/H})_{upper} + 12 = 9.72 - 0.777R_{23} - 0.951R_{23}^2 - 0.072R_{23}^3 - 0.811R_{23}^4 \tag{A6}$$

$$- \log(q)(0.0737 - 0.0713R_{23}) - 0.141R_{23}^2 + 0.0373R_{23}^3 - 0.058R_{23}^4) \tag{A7}$$

$$\log(\text{O/H})_{lower} + 12 = 9.40 + 4.65R_{23} - 3.17R_{23}^2 - \log(q)(0.272 + 0.547R_{23} - 0.513R_{23}^2) \tag{A8}$$

The ionization parameter q is then calculated from Z_{gas} using Equation A4, which is then used to recalculate Z_{gas} for the next iteration. This continues until convergence ($\Delta Z_{gas} < 0.01$), or up to 10 iterations, after which the fiber is flagged as a bad fit.

APPENDIX B: HOW Z_{gas} IS DETERMINED FOR OUR 8 DIFFERENT INDICATORS

Note: These techniques are nearly identical to those described in Appendix A2 of Kewley & Ellison (2008).

(i) R_{23} **- McGaugh (1991)**

Assumed q**:** Not fixed, models attempt to correct for variation in q using the [OIII]/[OII] line ratio defined in y below.
Method: This method is doubly degenerate so which branch we are in is determined using [NII]/[OII] as described in Equation A1. McGaugh and Koblunicky performed detailed simulations of HII regions and have come up with the following analytical fits to the results from their models. These fits for the upper and lower branches are given in Kobulnicky et al. (1999):

$$x = \log(R_{23}) = \log(([\text{OII}] + [\text{OIII}])/H\beta) \qquad y = \log\left(\frac{[\text{OIII}]}{[\text{OII}]}\right) \tag{B1}$$

$$Z_{upper} = 12 - 2.939 - 0.2x - 0.237x^2 - 0.305x^3 - 0.0283x^4 \tag{B2}$$

$$- y(0.0047 - 0.0221x - 0.102x^2 - 0.0817x^3 - 0.00717x^4) \tag{B3}$$

$$Z_{lower} = 12 - 4.994 + 0.767x + 0.602x^2 - y(0.29 + 0.332x - 0.331x^2) \tag{B4}$$

(ii) R_{23} **- Kobulnicky & Kewley (2004)**

Assumed q**:** Iterated upon.
Method: First the Z_{gas} and q are guessed at depending on if you are in the upper or lower R_{23} branch, then the code iterates to converge on a Z_{gas} and q. The equations behind this method are described in detail above in Appendix A.

(iii) R_{23} **- Zaritsky et al. (1994)**

Assumed q**:** No solution included.
Method: This method is derived by averaging the three previous calibrations for R_{23} done by Edmunds & Pagel (1984); Dopita & Evans (1986); McCall et al. (1985). This method only works for the upper branch of the R_{23} double degeneracy. Which branch we are in is determined using [NII]/[OII] as described in Equation A1. If we are in the lower branch, the fiber is disregarded. If we are in the upper branch we use the following equations to calculate Z_{gas}:

$$x = \log(R_{23}) = \log(([\text{OII}] + [\text{OIII}])/H\beta) \tag{B5}$$

$$Z_{upper} = 9.265 - 0.33x - 0.202x^2 - 0.207x^3 - 0.333x^4 \tag{B6}$$

(iv) **[NII]/[OII] - Kewley & Dopita (2002)**
Assumed q: 2×10^7, although q is nearly invariant for this Z_{gas} indicator.
Method: For the above assumed q, we set the line ratio equal to the following fourth degree polynomial for Z_{gas} (see Table 3 from Kewley & Dopita 2002):

$$\log\left([\mathrm{NII}]/[\mathrm{OII}]\right) = 1106.87 - 532.154Z + 96.3733Z^2 - 7.81061Z^3 + 0.239282Z^4 \tag{B7}$$

The IDL function *fz_roots.pro* then solves for the roots of this polynomial to find Z_{gas}.

(v) **([OIII]/Hβ)/([NII]/Hα) - Pettini & Pagel (2004)**
Assumed q: None, fit is empirical
Method: Empirical fit of line ratios to 137 HII regions, 131 have metallicities measured used the direct T_e method, while 6 are derived using strong line methods.

$$x = \log\left(\frac{[\mathrm{OIII}]/H\beta}{[\mathrm{NII}]/H\alpha}\right) \tag{B8}$$

$$Z = 8.73 - 0.32x \tag{B9}$$

(vi) **[NII]/Hα - Denicoló et al. (2002)**
Assumed q: None, fit is empirical.
Method: Empirical fit to 236 galaxies. Approximately half are metal poor and half are metal rich to cover a wide range in Z_{gas}. A linear least squares fit to the data gives:

$$x = \log\left([\mathrm{NII}]/H\alpha\right) \tag{B10}$$

$$Z = 9.12 + 0.73x \tag{B11}$$

(vii) **[NII]/Hα - Pettini & Pagel (2004)**
Assumed q: None, fit is empirical
Method: Empirical fit of line ratios to 137 HII regions, 131 have metallicities measured used the direct T_e method, while 6 are derived using strong line methods. Note that we only consider fibers with $-2.5 < \log([\mathrm{NII}]/H\alpha) < -0.3$.

$$x = \log\left([\mathrm{NII}]/H\alpha\right) \tag{B12}$$

$$Z = 9.32 + 2.03x + 1.26x^2 + 0.32x^3 \tag{B13}$$